KfK 2890
November 1981

The WECHSL Code: A Computer Program for the Interaction of a Core Melt with Concrete

Model Description and User's Manual

M. Reimann, W. B. Murfin
Institut für Reaktorbauelemente
Projekt Nukleare Sicherheit

Kernforschungszentrum Karlsruhe

KERNFORSCHUNGSZENTRUM KARLSRUHE

Institut für Reaktorbauelemente
Projekt Nukleare Sicherheit

KfK 2890

The WECHSL Code:
A Computer Program for the Interaction of a Core Melt with Concrete

Model Description and User's Manual

M. Reimann, W.B. Murfin*

* Sandia Laboratories, Albuquerque, N.M.
Formerly USNRC delegate to Projekt Nukleare Sicherheit at Kernforschungszentrum Karlsruhe

Kernforschungszentrum Karlsruhe GmbH, Karlsruhe

Kernforschungszentrum Karlsruhe GmbH
ISSN 0303-4003

Abstract

The WECHSL Code is a mechanistic computer code developed for the analysis of the interaction of molten LWR reactor materials with concrete. The code in its present state performs calculations from the time of the initial contact of a hot molten pool slumping into a concrete cavity to the time of freezing of an entire layer of the pool. The modelling of the freezing phase, however, needs some further elaboration along with experimental confirmation. The code is capable to treat both the limited type of simulation experiments with melt masses between 100 and 600 kg as well as hypothetical core melt down accidents with actual, full scale reactor dimensions.

The submodels used in the code and their physical background are described in detail. Furthermore, the results of a test sample along with instructions for the use of the code are given.

Der WECHSL-Code: Ein Rechenprogramm für die Wechselwirkung einer Kernschmelze mit Beton

Modellbeschreibung und Benutzeranleitung

Zusammenfassung

Der WECHSL-Code, ein mechanistisches Rechenprogramm, wurde für die quantitative Beschreibung der Wechselwirkung von geschmolzenen LWR-Materialien mit Beton entwickelt. In der derzeitigen Ausbaustufe können Berechnungen vom ersten Kontakt einer heißen Schmelze, die sich in eine Betonkaverne ergießt, bis zum vollständigen Erstarren einer gesamten Schicht der Schmelze durchgeführt werden, wobei die Modellierung der Erstarrungsphase noch weiterer Entwicklungsarbeit und experimenteller Bestätigung bedarf. Der Code gestattet die Behandlung sowohl von Simulationsexperimenten mit Schmelzbadmassen zwischen 100 und 600 kg als auch von hypothetischen Kernschmelzenunfällen in Reaktordimensionen.

Die im Code benützten verschiedenen Modelle mit ihren physikalischen Grundlagen werden detailliert beschrieben. Weiter werden nach Anweisungen für die Handhabung des Rechencodes die Ergebnisse eines Testbeispiels wiedergegeben.

Table of Contents

Nomenclature

a	Laplace constant
A	aerea
Ar	Archimedes number
c	specific heat
c_o	Stefan-Boltzmann-constant
C	constant
D	coefficient
$Eö$	Eötvös number
F	force
f_{TP}	friction factor
g	acceleration of gravity
Gr	Grashof number
h	heat transfer coefficient
h	specific enthalpy
h_d	latent heat of melting or decomposing
H	enthalpy
k	thermal conductivity
K	equilibrium constant
L	characteristic length
$\dot{m}$	mass flux
$\dot{m}/A$	mass flux density
n	exponent
n	coordinate perpendicular to the wall
Nu	Nusselt number
p	pressure
Pr	Prandtl number
Q	heat flux, volume flux
Q/A	heat flux density
r	radius, radial coordinate
r_{eq}	equivalent bubble radius
R	ideal gas constant
Re	Reynolds number
s	coordinate in direction of the wall
Ste	Stefan (phase change) number
T	temperature

u_b	bubble rise velocity
v	wall shear velocity
v_g	artificial gas velocity
V_M	partial molar volume
w	flow velocity
We	Weber number
y^+	dimensionless distance
α	angle of inclination
β	coefficient of volumetric expansion
γ	heat transfer enhancement factor
δ	layer thickness (boundary layer, gas film, crust)
$\tilde{\delta}$	dimensionless layer thickness
δ^*	flow cell height
$\delta\tau$	time step
ΔH_c	specific decomposition enthalpy
ΔH_{LS}	molar latent heat of freezing
$\Delta\rho$	density difference
ε	void fraction
ε	emissivity
ζ	friction coefficient
$\dot{\zeta}$	melt front velocity
λ	Taylor wave length
μ	dynamic viscosity
ν	kinematic viscosity
ξ	dimensionsless coordinate
π	3.14159
ρ	density
σ	surface tension
τ	time
τ_w	wall shear stress
ϕ	boundary condition parameter
ϕ_g	porosity
χ	molar fraction
ψ	weight fraction

Subscripts

ax	axial
b	bubble
bs	bubble swarm
c	concrete
c	turbulent core
cond	conductive
conv	convective
d	decomposition
dO	melting surface
eff	effective
eq	equivalent
g	gaseous
h	hydrodynamical
i	species i, mesh i
i	interphase
ℓ	liquid
L	liquidus
LS	between liquidus and solidus
m	mean
m	melting
m	metal
o	oxide
rad	radiative
s	solid
sur	surface
S	solidus
t	thermal
tot	total
w	wall

1. Introduction

Light water reactors are designed and constructed with great attention to safety considerations. As a result of these efforts, it is extremely improbable that an accident leading to melt down of the nuclear core would occur. However, in the highly unlikely event of the simultaneous failure of a number of safety systems, it is possible that all cooling of the core could be lost. If this occured, decay heat would melt the reactor core. In the course of such a hypothetical core melt down accident, the combination of molten fuel, cladding, and structural material would collect in the lower plenum of the reactor pressure vessel. This molten material would melt through the pressure vessel within 20 - 160 min. after initiation of the accident, depending on the type and the course of the accident. Following reactor pressure vessel melt through, the molten core would drop onto the concrete base structure of the reactor building. The interaction of the core melt with concrete would continue for a long period of time.

During this interaction, a number of phenomena have an important bearing on the subsequent course of the accident /40/. These include:

- concrete decomposition
- release of steam and gases from the decomposing concrete,
- chemical reactions of these gases with metallic constituents of the melt and within the containment atmosphere,
- dilution of the molten fuel materials by molten concrete constituents and alteration of the freezing behavior of the molten pool.

These phenomena have a decisive influence on the basic safety questions:

Can the containment fail by overpressurization ?

Can the concrete base melt through ?

Even though a core melt accident is very unlikely, the possibility of health consequences to the public makes it necessary to give best-estimate answers to these questions. In the existing

risk studies /1,2/, conservative assumptions lead to pessimistic results. Better understanding of the physical background of the molten core/concrete interaction would provide a more realistic basis for an advanced risk study. Furthermore, good understanding of this part of the accident sequence could lead to design measures which will help in reducing the risk of a core melt down accident.

It is impossible to simulate the interaction completely in experiments, because of the materials, masses, and dimensions involved. Recourse must be made to mathematical models or computer codes to extrapolate the limited tests which can be performed to the expected materials, masses, and dimensions involved in a hypothetical melt down accident.

The WECHSL code is a mechanistic code based on the current understanding of the phenomena occuring during the interaction of a molten pool with concrete. As far as possible, the code is capable to treat both the limited type of simulation experiments with non-radioactive materials and melt masses between 100 and 600 kg as well as hypothetical core melt down accidents with actual, full scale reactor dimensions. The code was originally based on the INTER code /3/ developed in 1977. However, in the meantime so many improvements and changes have been made that the WECHSL code now bears little resemblance to the INTER code.

Like the INTER code, WECHSL considers the separation of the molten pool into metal and oxide layers. Numerous experiments with simulant materials have shown that the metal and oxide layers will rapidly segregate /4,5/. Further observations in these tests showed that vast amounts of combustible gases were produced that stirred the layers of the molten pool vigorously. These phenomena suggest a conceptual model as shown schematically in Figure 1.

Energy can be internally produced by decay heat or by exothermic reactions. Energy is lost to the concrete and to the overlying environment by a variety of mechanisms. Moreover, energy can be exchanged between the molten layers.

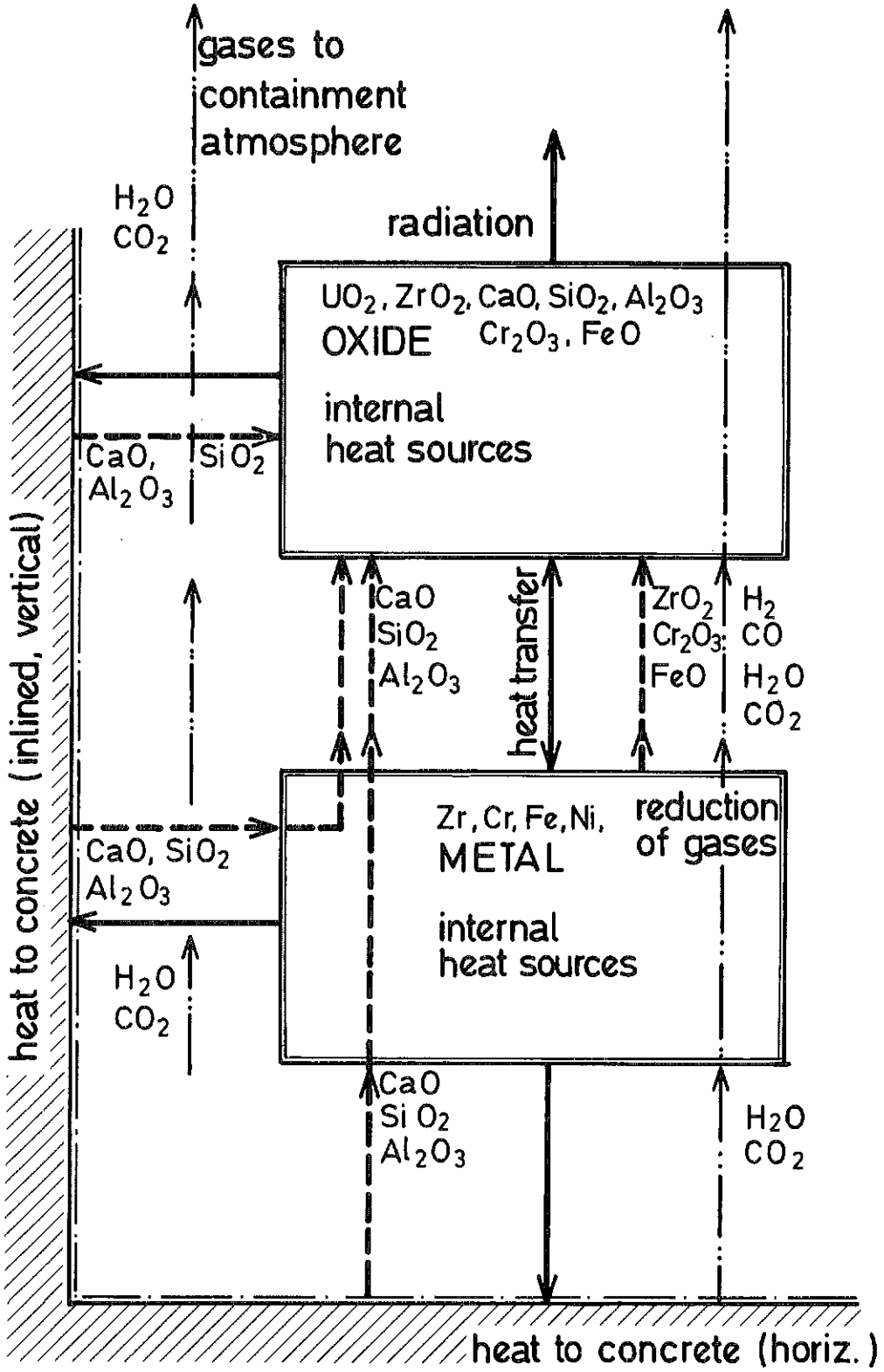

Figure 1: Flows of energy and material in WECHSL

The thermal attack on concrete gives rise to a vigorous evolution of gases. Much of these gases pass through the melt. During their passage, the melt is thoroughly stirred, so that each layer is nearly isothermal. Water vapor and carbon dioxide will be reduced as they pass through the metallic layer. Liquid concrete decomposition products dilute the oxide layer. The composition and, consequently, the material properties of the layers are thus continuously changing.

Because of the assumptions of gas stirring and prompt transfer of molten concrete to the oxide layer, the model is inapplicable to the period after freezing of either the metallic or the oxidic phase. It has been both theoretically and experimentally demonstrated that the propagation of the melt front into the concrete structure slows down after freezing. However, the solidified melt layer could be in contact with the concrete for long periods of time. Thus this phase is also important and a relevant modeling should be provided. The code in its present form is limited to the phase of the core/concrete interaction where both layers are liquid.

2. Present Constitution of the WECHSL-Code

2.1 General Remarks

Each of the phenomena modelled in the code has been included in such a way as to permit experimental or theoretical verification. Some of the models have already been confirmed experimentally. For those for which complete experimental verification is not yet available, the models have been constructed in such a way that empirical constants can be easily changed to match with the experimental data. The values of these constants in the present version have been chosen to give physically realistic results pending further confirmation.

Each of the important models contained in the code is described in detail in the following sections. The sources from which the submodels have been built are also given.

2.2 Melt/Concrete Interphase

2.2.1 Concrete Decomposition

The decomposition of concrete is an exceedingly complex process. Differential thermal analyses of concrete with different aggregates /6/ reveal the consecutive steps of dehydration, $CaCO_3$ decomposition and the range of melting with increasing temperature. Each of these decomposition steps takes place in a certain temperature range. Furthermore, as indicated by Powers /7/, chemical kinetics can alter each effective decomposition temperature range. The released gases flow through the residual porous concrete matrix and transport energy. Moreover, energy is transfered in this matrix of changing porosity by transient heat conduction.

In the WECHSL code a strongly simplified model is applied. It is assumed that under the impact of a high heat flux, the decomposition process of concrete can be treated as one-dimensional heat conduction in a semi-infinite body. At the melting surface, the molten material is continuously being removed. The gas release and other chemical reactions are assumed to occur at definite temperatures during the heat-up process of the concrete. The higher heat flux density is, the smaller is the zone in the concrete where the temperature drops from the melting point of the silicates to the ambient temperature. This means, that a quasi-stationary temperature profile will be established in the concrete a short time after the surface is exposed to high temperature melt.

The model for the decomposition process is formulated for n different layers /8/. In the layer i , the porosity of the concrete is ϕ_{gi}, and the weight percentage of the released gases escaping through this layer is ψ_{gi}. By assuming perfect temperature exchange between the solid and the gases, the coupling of the two relevant energy equations by source and sink terms results in a quasi stationary energy equation for the whole system. Between the layers of

the concrete, heat is absorbed by chemical or physical reactions. One set of boundary conditions is given by the melting temperature at the surface and the decomposition temperatures between the layers. Another set of boundary conditions can be established by energy balances at the boundaries between the layers.

The quasi stationary energy equation can be described by an exponential type temperature distribution. By applying the boundary conditions to this solution, the decomposition velocity, $\dot{\zeta}$, can be obtained according to /9/ as

$$\dot{\zeta} = \frac{(Q/A)}{\rho_c \, \Delta H_c} \, . \qquad (2.2.1 - 1)$$

This equation indicates that the quasi-stationary decomposition rate depends only on the imposed heat flux. The concrete decomposition enthalpy

$$\Delta H_c = (1-\psi_{g0}) \, h_{d0} + \left\{(\rho c)_{eff\,0} / \rho_c\right\} \, (T_{d0}-T_{00}) \qquad (2.2.1 - 2)$$

is a material property. The effective volumetric heat capacity, ρc, and the effective thermal conductivity, k, are given by

$$(\rho c)_{eff\,i} = \rho_{gi} \, c_{p\,gi} \, \phi_{gi} \left(1+\frac{\psi_{gi} \, \rho_c}{\phi_{gi} \, \rho_{gi}}\right) + (1-\phi_{gi}) \, \rho_{si} \, c_{si} \, , \qquad (2.2.1 - 3)$$

and

$$k_{eff\,i} = \phi_{gi} \, k_{gi} + (1-\phi_{gi}) \, k_{si} \, . \qquad (2.2.1 - 4)$$

Equations (2.2.1 - 3 and 4) can be evaluated by applying averaged solid (subscript s) and gaseous (subscript g) properties of the relevant concrete components. The unknown temperature difference $(T_{d0}-T_{00})$ in Eq. (2.2.1 - 2) is determined by regression from

$$T_{d\,i-1} - T_{d0\,i-1} = T_{d\,i-1} - T_{d\,i} + \frac{\psi_i \, \rho_c \, h_{d\,i} + (T_{d\,i}-T_{0\,i}) \, (\rho c)_{eff\,i}}{(\rho c)_{eff\,i-1}} \, . \qquad (2.2.1 - 5)$$

The decomposition reactions as considered in the model are given in Table 1. The exothermal formation of wollastonite ($CaSiO_3$) can be optionally included. A comparison between calculated and measured values for the decomposition enthalpies of different types of concrete is given in /6/.

Decomposition Temperature (K)	Decomposition Reaction	Heat of Decomposition (kJ/mole)
1573	$SiO_{2s} \rightarrow SiO_{2l}$	-8.53
	$CaO + SiO_2 \rightarrow CaSiO_3$	+88.5
	$CaSiO_{3s} \rightarrow CaSiO_{3l}$	-46.5
1167	$CaCO_3 \rightarrow CaO + CO_{2g}$	-165.5
796	$Ca(OH)_2 \rightarrow CaO + H_2O_g$	-99.5
400	$H_2O_l \rightarrow H_2O_g$	-39.4

Table 1: Characteristics for the decomposition of concrete

By applying this model in the WECHSL-code, the decomposition process is characterized by a surface temperature T_{dO} and by a unique concrete property, the volumetric decomposition enthalpy $\rho_c \Delta H_c$.

The assumption of a quasi-stationary decomposition velocity as given in Eq. (2.2.1-1) introduces two principal errors; the first because the heat flux imposed on the surface is actually time dependent and, consequently, the heat conduction process is transsient, and the second because of chemical kinetics. Although these two components are actually coupled, an idea of their magnitude can be obtained by considering them separately.

The transient problem of heat conduction with simultaneous melting in a homogeneous solid has been solved by Landau /9/. Although concrete is certainly far from homogeneous, it is instructive to

apply the method of Landau to get a feeling for the magnitude of the error involved.

At time $\tau = 0$, the semi-infinite homogeneous concrete body is at ambient temperature T_∞ and a constant heat flux density Q/A is imposed at the surface. The transient temperature distribution can be found analytically. From the time dependent temperature profile, the time at which the surface reaches melting temperature is evaluated to be

$$\tau_m = \frac{\pi\,(T_m - T_\infty)^2}{4\,(Q/A)^2}\,k\,\rho\,c \qquad (2.2.1 - 6)$$

or, after introducing the parameter

$$\theta = \frac{\pi^{1/2}}{2}\,\frac{c\,(T_m - T_\infty)}{h_{dO}}\,; \qquad (2.2.1 - 7)$$

$$\tau_m = \left(\rho\,\frac{h_{dO}}{(Q/A)}\,\frac{k}{\rho\,c}\,\theta\right)^2. \qquad (2.2.1 - 8)$$

After the surface has reached melting temperature, the melt front starts to move. The subsequent heat up process with simultaneous melting was treated numerically in /9/. In Figure 2, the ratio of the actual melt front velocity to the quasi-stationary melt front velocity resulting from Eq. (2.2.1-1) is plotted over the dimensionless time τ/τ_m with the material property θ as parameter. For a typical silicaceous concrete, this property yields $\theta = 16.9$. By integration of the relevant curve in Figure 2, it follows that for this type of concrete the acceleration phase of the melt front can be substituted by a displacement of the time ordinate as

$$\tau_{q.st} = 1.26\,\tau_m\,. \qquad (2.2.1 - 9)$$

By evaluating Equs. (2.2.1-8,9) the results given in Table 2 are obtained:

$\tau_{q.st.}$ s	Q/A 10^4 W/m^2
1	377.2
10	119.3
100	37.7

Table 2: Time ordinate displacement substituting the initial heat-up process

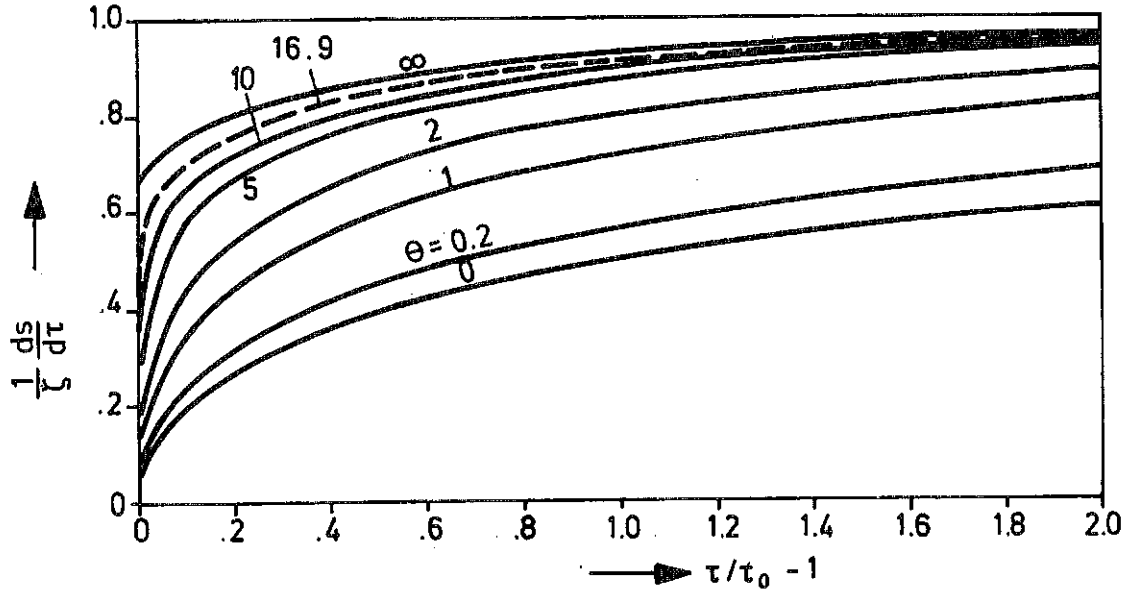

Figure 2: Melt front acceleration phase

The error due to chemical reactions is not as easily assessed. An approximate magnitude of the error can be obtained by assuming that the concrete is heated at a constant temperature rate from room temperature to the decomposition temperature for each decomposition step in the time $\tau_{q.st.}$. When the resulting temperature rate is substituted into the kinetic decomposition model of Powers /7/, it is found that the time required to decompose 90 % of the concrete constituents is of the order of the required displacement of the time axis, but generally smaller.

The transient effects could be important, if the melt temperature and therefore the transferred heat flux is low, or, if the heat flux is strongly time dependent. In the hypothetical core meltdown accident the initial temperature of the melt will be approximately 2500°C, and the duration of the interaction will be hours or days with a slowly decreasing pool temperature. This means that the assumption of a quasi-stationary temperature profile might be justified as long as considerable concrete errosion appears. However, in the low temperature range and after solidification of the melt, the transferred heat fluxes are low and the transient effects of the concrete decomposition will be more important.

In simulation tests, the lowest initial temperatures have been on the order of 1700°C. Without additional heating, the cooling rate of the melt is higher, the smaller the melt mass is. This means that the assumption of quasi-stationarity might not be justified in such tests where the duration of the experiment - i.e. the time to solidify the melt - is less than several minutes.

2.2.2 Gas Film Model

Due to the heat flux density (Q/A), the concrete is decomposed with a weight fraction ψ_g into gaseous and with $(1 - \psi_g)$ into liquid decomposition products. From the quasi-stationary heat transport model as discussed above, the mass flux density of the released gases is given by

$$\left(\frac{\dot{m}}{A}\right) = \frac{\psi_g}{\Delta H_c} \left(\frac{Q}{A}\right)_{tot} . \qquad (2.2.2 - 1)$$

The ratio of the released gas volume to the volume of liquid decomposition products is in the order of 1000 : 1. Because of the dominance of the gaseous phase, a gas film of thickness δ is likely to be present between the core melt and the concrete at least at high heat flux densities. Through this gas film, heat will be transfered by conduction and radiation. So, the total heat flux density is

$$(Q/A)_{tot} = (Q/A)_{cond} + (Q/A)_{rad} \qquad (2.2.2 - 2)$$

with

$$(Q/A)_{cond} = \frac{A_{eff}}{A_{tot}} \frac{k_g \, (T_i - T_{dO})}{\delta} \qquad (2.2.2 - 3)$$

and

$$(Q/A)_{rad} = \varepsilon_{id} \, c_0 \, (T_i^4 - T_{dO}^4) \qquad (2.2.2 - 4)$$

where

$$\varepsilon_{id} = \frac{1}{1/\varepsilon_i + 1/\varepsilon_d - 1} \, . \qquad (2.2.2 - 5)$$

As the heat is transfered from a molten pool to a gas liberating wall, the process can be considered as inverse film boiling. Consequently, the derivation of the heat transfer correlations follows closely the ideas of Berenson /10/, Bromley /11/, and Hsu, Westwater /12/ with additionally taking into account the heat transfer by radiation.

To study the principles of an inverse film boiling process, model experiments with dry ice slabs in a water pool are helpful. As shown in /8/, the carbon dioxide gas film which covers a horizontal sublimating dry ice slab gives rise to the formation of a square grid of bubble release sites. Similar experiments were carried out by Dhir et al. /13/ who also proposed the Berenson model for this process. By passing over to strongly inclined or vertical walls, bubbles do not break away any longer and a continuous laminar gas layer streaming upwards separates the pool from the sublimating surface. After reaching a critical film thickness, the flow becomes increasingly turbulent. The different flow regimes as shown in Figure 3 and a model experiment showing the sublimation of a dry ice corner under water have been given in /14/.

For the sake of completeness, the heat transfer models from a hot melt to concrete as derived in /8/ for horizontal surfaces and in /15/ for inclined and vertical surfaces will be summarized here.

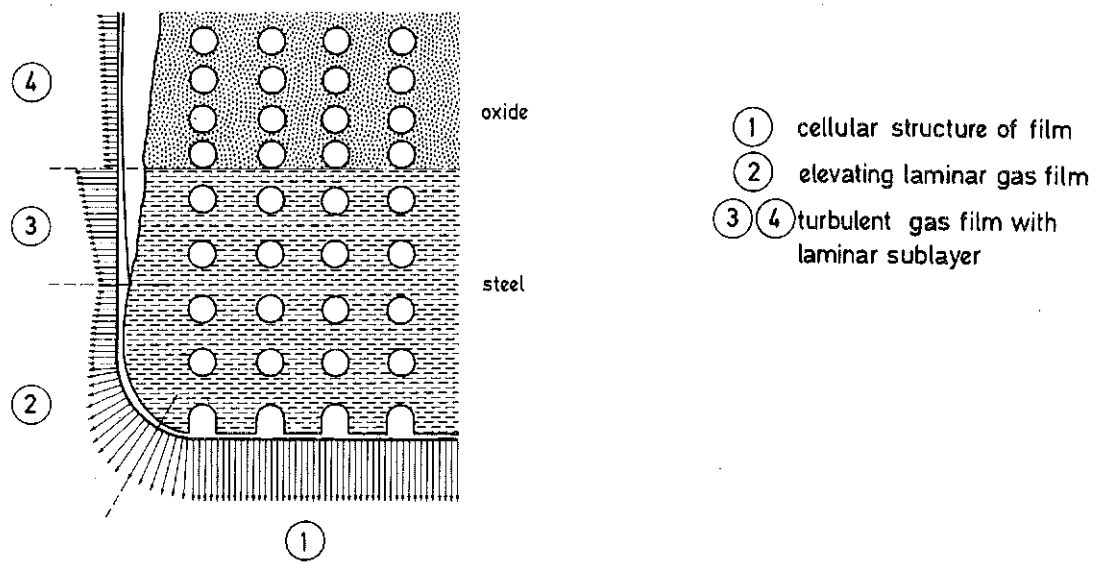

Figure 3: Schematic representation of gas film, bubble rise, and heat transfer coefficient

At horizontal or slightly inclined surfaces, the gases make up an unstable gas layer at the interface of the decomposing solid with the liquid pool. This unstable gas layer breaks up in a regular pattern of bubble formation sites, where gas bubbles are growing and then leave the film. Due to instability theory of stratified layers (Taylor instability), the most probable wave length between two bubble formation sites

$$\lambda = 2 \pi \sqrt{3}\, a \qquad (2.2.2 - 6)$$

depends on the Laplace constant

$$a = \left(\frac{\sigma}{g\,(\rho_\ell - \rho_g)}\right)^{1/2} . \qquad (2.2.2 - 7)$$

In Figure 4 a time averaged rotational symmetric flow cell of the aerea

$$A_{tot} = \lambda^2 \qquad (2.2.2 - 8)$$

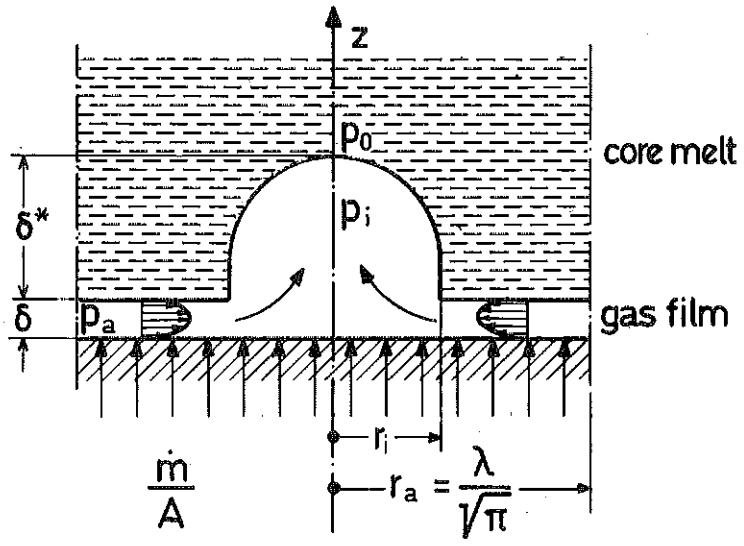

Figure 4: Flow cell on a horizontal wall

around a centre of bubble formation is shown. The quantities r_i and δ^* are connected with the wavelength λ by

$$r_i = \frac{\lambda}{4} \; ; \quad \delta^* = \frac{\lambda}{3} \; . \qquad (2.2.2 - 9)$$

The mean film thickness δ is determined from the balances of mass and momentum under the assumption that the gaseous decomposition products enter the film with a constant specific mass flux $\dot{m}/A_{tot}$ in z-direction. The mass balance

$$\frac{1}{r} \frac{d}{dr}\left(r \, \rho_g \, w_m \, \delta\right) = \left(\frac{\dot{m}}{A}\right) \qquad (2.2.2 - 10)$$

is integrated in radial direction to give

$$w_m = - \frac{1}{2} \left(\frac{\dot{m}}{A}\right) \frac{1}{\rho_g \, \delta} \left(\frac{r_a^2}{r} - r\right) \qquad (2.2.2 - 11)$$

for the mean velocity of the gas flowing in radial direction.

The momentum balance in the radial direction taking into account pressure forces and friction forces reads

$$\frac{\partial p}{\partial r} = \mu_g \frac{\partial^2 w}{\partial z^2} \; . \qquad (2.2.2 - 12)$$

The integration of this equation results in

$$w_m = - \frac{(3\phi-2)}{12} \frac{\delta^2}{\mu_g} \frac{\partial p}{\partial r} \quad . \qquad (2.2.2 - 13)$$

Upon combining Equs. (2.2.2-11,13) and performing a radial integration one gets

$$p_a - p_i = \frac{6}{(3\phi-2)} \frac{\mu_g}{\rho_g \delta^3} \left(r_a^2 \ln \frac{r_a}{r_i} - \frac{r_a^2 - r_i^2}{2} \right) . \qquad (2.2.2 - 14)$$

In the above equation, the parameter ϕ characterizes the boundary condition at the gas/liquid interphase. In equation (2.2.2 - 13) $\phi = 1$ applies for the liquid acting as a solid wall and $\phi = 2$ applies for a slip condition. In practice, the boundary condition will lie somewhere between these two conditions.

A hydrostatic pressure balance around the flow cell gives

$$p_a - p_0 = g \delta^* \rho_\ell \ , \qquad (2.2.2 - 15)$$

$$p_i - p_0 = g \delta^* \rho_g + \frac{2\sigma}{r_i} . \qquad (2.2.2 - 16)$$

The combination of Equs. (2.2.2-9,14,15,16) yields

$$\left(\frac{\dot{m}}{A}\right)_{tot} = 0.3724 \frac{(3\phi-2)}{12} \frac{g \rho_g \Delta\rho \delta^3}{\mu_g a} \qquad (2.2.2 - 17)$$

for the specific mass flux of the gases released from the concrete and entering the flow cell.

In the idealized flow cell, the heat transfer by conduction through the gas film of thickness δ is effective on the area given by the ratio

$$A_{eff}/A_{tot} = (1 - \frac{\pi}{16}) = 0.804 \qquad (2.2.2 - 18)$$

By combining Equs. (2.2.2-1,2,3,4 and 17,18), and by introducing the dimensionless quantities

$$\bar{\delta} = \delta/L$$

$$Nu = \frac{(\dot{Q}/A)\ L}{k_g\ (T_i - T_{dO})}$$

$$Gr = \frac{g\ \rho_g\ \Delta\rho\ L^3}{\mu_g^2} \qquad (2.2.2 - 19)$$

$$Pr\ Ste = \frac{\mu_g\ \Delta H_c}{k_g\ (T_i - T_{dO})}$$

the dimensionless film thickness can be determined from the following equation as

$$\frac{\bar{\delta}}{\delta} = 0.825 \left\{ \frac{(3\phi-2)}{12} \frac{Gr\ Pr\ Ste}{\psi_g} \frac{L}{a} \frac{1}{1+1.244\ \bar{\delta}\ Nu_{rad}} \right\}^{1/4} . \qquad (2.2.2 - 20)$$

The Nusselt number based on total heat transfer rate is obtained as

$$Nu_{tot} = Nu_{rad} + \frac{A_{eff}}{A_{tot}} \frac{1}{\bar{\delta}} . \qquad (2.2.2 - 21)$$

It is now assumed that the wave length λ is small compared to the radius of curvature while going from a horizontal to a strongly inclined concrete surface. It could be seen in model experiments with dry ice slabs that up to an inclination $\alpha = 30^o$, the unstable gas film with bubbles breaking away was the governing mechanism of gas release. So, in this intermediate region the heat transfer is assumed to be constant as given by Equs. (2.2.2-20,21). If the inclination goes beyond 30^o, a continuous gas layer streaming along the wall is formed. Now, the conductive heat transport across the gas film is effective on the whole surface, i.e.

$$A_{eff}/A_{tot} = 1 . \qquad (2.2.2 - 22)$$

With the denotations of Figure 5, the mass balance reads

$$\frac{d}{ds}(\dot{m}_{ax}) = (\frac{\dot{m}}{A}) \qquad (2.2.2 - 23)$$

with

$$\dot{m}_{ax} = \rho_g\ w_m\ \delta \qquad (2.2.2 - 24)$$

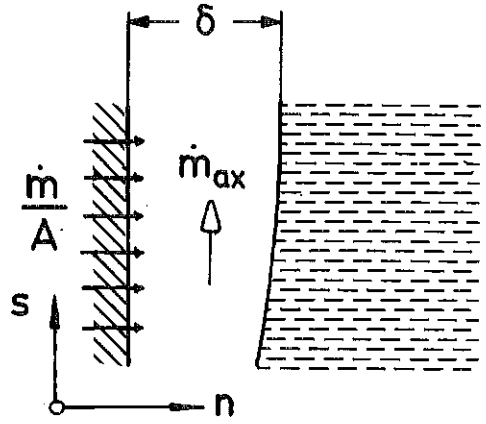

Figure 5: Laminar gas film on an inclined or vertical wall

and the integration of the simplified momentum equation taking into account friction forces and buoyancy forces yields

$$\mu_g \frac{d^2w}{dn^2} = - g \Delta\rho \sin\alpha \qquad (2.2.2 - 25)$$

or, after integration

$$w_m = \frac{(3\phi-2)}{12} \delta^2 \frac{g \Delta\rho}{\mu_g} \sin\alpha \ , \qquad (2.2.2 - 26)$$

By introducing the dimensionless variable

$$\xi = s/L \qquad (2.2.2 - 27)$$

and by using the dimensionless groups as defined in Equs. (2.2.2-19), the combination of Equs. (2.2.2-1,2,3,4,22, 23,24) results in a differential equation for determining the film thickness δ :

$$\frac{d\tilde{\delta}}{d\xi} = \frac{4}{(3\phi-2)} \frac{\psi_g}{Gr\ Pr\ Ste \sin\alpha} \frac{1 + Nu_{rad}\ \tilde{\delta}}{\tilde{\delta}^3} \ , \qquad (2.2.2 - 28)$$

and the total heat transfer is evaluated again with Equation (2.2.2-21).

The thickness of the laminar gas film increases up to a critical value which can be determined from the relations for a single-phase fluid (see i.e. Schlichting /16/). By introducing the wall shear velocity

$$v = (\tau_w/\rho_g)^{1/2} \ , \qquad (2.2.2 - 29)$$

the dimensionless velocity

$$w^+ = w/v \ , \qquad (2.2.2 - 30)$$

and the dimensionless distance

$$y^+ = n \frac{\rho_g v}{\mu_g} \qquad (2.2.2 - 31)$$

can be defined. Within the framework of a two layer concept for a single-phase fluid flow, a limiting value for the layer thickness is

$$y^+ = 10 . \qquad (2.2.2 - 32)$$

By assuming a linear velocity profile

$$w^+ = y^+ , \qquad (2.2.2 - 33)$$

the critical Reynolds number is defined as

$$Re^* = \frac{\rho_g w_m \delta}{\mu_g} = w^+ y^+ = 100 . \qquad (2.2.2 - 34)$$

This results in a critical film thickness given by

$$\delta_{crit} = \left\{ \frac{12}{(3\phi-2)} \frac{Re^*}{Gr \sin\alpha} \right\}^{1/3} . \qquad (2.2.2 - 35)$$

Above this point, a turbulent core (subscript c) with a laminar sublayer (subscript g) is present as indicated in Figures 4,6. The mass flux through the film is

$$\dot{m}_{ax} = \rho_c w_c \left(\delta_c - \delta \left(1 - \frac{1}{2} \frac{\rho_c}{\rho_g} \right) \right) \qquad (2.2.2 - 36)$$

with the velocity w_c in the turbulent core as

$$w_c = y^{+2} \frac{\mu_g}{\rho_g \delta} . \qquad (2.2.2 - 37)$$

Inserting Equs. (2.2.2 - 36,37) in Equ. (2.2.2-23) and combining the result with Equs. (2.2.2-1,2,3) yields

$$\frac{d}{d\xi} \frac{\tilde{\delta}_c}{\tilde{\delta}} = \frac{\rho_g}{\rho_c} \frac{\psi_g}{y^{+2} Pr\, Ste} \frac{1}{\tilde{\delta}} \left(1 + Nu_{rad} \tilde{\delta}\right) \qquad (2.2.2 - 38)$$

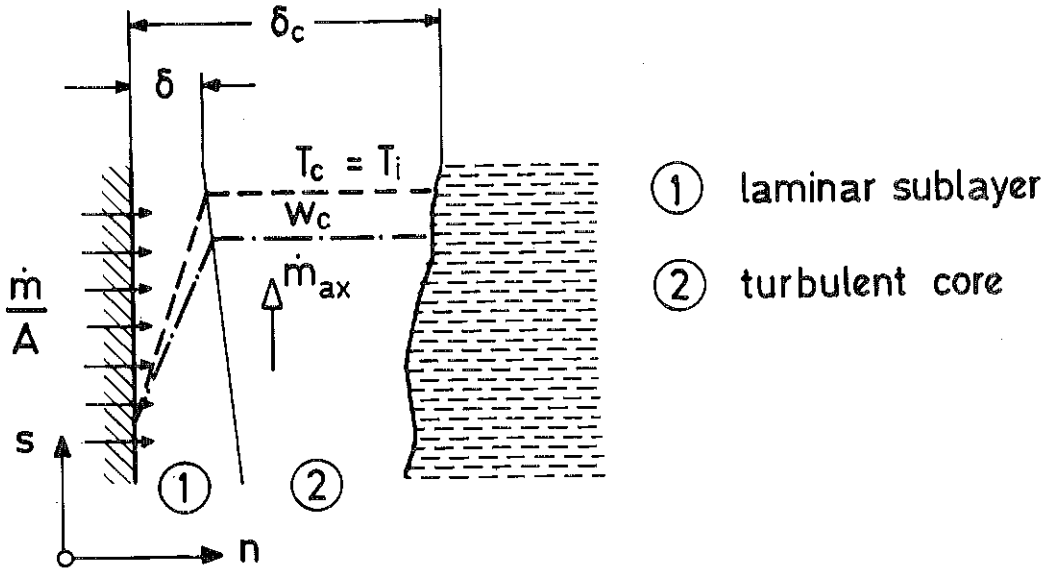

Figure 6: Turbulent gas film on an inclined or vertical wall

In a second step, a momentum balance is applied on a control element as shown in Figure 7:

Figure 7: Forces acting on an element of the turbulent gas film

$$\rho \int_{(K)} \vec{w}\, dQ - dF_1 - dF_2 + dF_3 = 0. \qquad (2.2.2 - 39)$$

(Q: volume flux in the film; F: forces)

Evaluating the momentum integral yields

$$\rho \int_{(K)} w\, dQ = -\frac{\rho_c}{\rho_g} y^{+4} \frac{\mu_g^2}{\rho_g} \frac{d}{ds} \left(\frac{1}{\delta} \left\{ \frac{\delta_c}{\delta} - \left(1 - \frac{1}{3} \frac{\rho_g}{\rho_c}\right) \right\} \right) ds\,. \qquad (2.2.2 - 40)$$

The forces acting in direction of the flow are the wall friction force

$$dF_1 = \tau_w \, ds = y^{+2} \frac{\mu_g^2}{\rho_g} \frac{1}{\delta^2} \, ds \, , \qquad (2.2.2 - 41)$$

the interphase friction force

$$dF_2 = \tau_i \, ds = \frac{\rho_c}{\rho_g} \, y^{+4} \frac{\mu_g^2}{\rho_g} \frac{f_{TP}}{2} \frac{1}{\delta^2} \, ds \, , \qquad (2.2.2 - 42)$$

and the buoyancy force

$$dF_3 = g \, \Delta\rho \, \delta_c \, \sin\alpha \, ds \qquad (2.2.2 - 43)$$

Combination of Equs. (2.2.2-39,40,41,42,43) and use of Equation (2.2.2-38) results in

$$\frac{d\tilde{\delta}}{d\xi} = \frac{\frac{\rho_g}{\rho_c} \frac{\psi_g}{y^{+2} \, Pr \, Ste} (1+Nu_{rad} \, \tilde{\delta}) + \left(\frac{f_{TP}}{2} + \frac{\rho_g}{\rho_c} \frac{1}{y^{+2}}\right) - \frac{\rho_g}{\rho_c} \frac{Gr \sin\alpha}{y^{+4}} \tilde{\delta}_c \, \tilde{\delta}^2}{\frac{\tilde{\delta}_c}{\tilde{\delta}} - (1 - \frac{1}{3} \frac{\rho_g}{\rho_c})} \qquad (2.2.2 - 44)$$

Equs. (2.2.2-38,44) are a system of differential equations for the total layer thickness δ_c and the laminar sublayer thickness δ. This system of differential equations as well as the differential equation (2.2.2-28) for laminar flow are integrated in WECHSL numerically by means of a Runge-Kutta-method.

In the turbulent film model, the heat is assumed to be transferred by conduction through the laminar sublayer of thickness δ, and by radiation from the liquid/gas interface to the concrete surface. Consequently, the total heat transfer can again be evaluated by Equ. (2.2.2-21).

2.2.3 Pool Boundary Layer

In all flow regimes of the gas film model, the temperature difference $T_i - T_{d0}$ is decisive for the heat transfer, where T_i is the temperature of the melt at the interphase with the gas film and T_{d0} is the surface temperature of the decomposing concrete. In the bottom region of the pool, a thin boundary layer driven by micro-convection between bubble release sites is assumed to exist. . Along the inclined walls, a boundary

layer is created by drag forces exerted by the gas flowing in the film. Both the boundary layers result in a temperature drop of the pool temperature T_m to the interface temperature T_i. Because of the excellent thermal conductivity and the low viscosity of the metals which are normally at the bottom of the pool, this temperature drop across the boundary layer is only on the order of few degrees. However, in the oxide region (region 4 in Figure 3), the temperature drop across the boundary layer is quite significant because of the low thermal conductivity and the high viscosity of the oxides. This reduces considerably the total heat transfer from the molten pool to the concrete. To describe the attack of a two-phase melt on the concrete properly, a boundary layer analysis especially for inclined and vertical walls in the oxide region is important. The results of this approach can also be applied as an first-order approximation on the bottom region where the metallic melt interacts.

In reference /17/, the complete analysis of the boundary layer formation at a laminar gas film/liquid interface is given. Boundary layer calculations were carried out for vertical plates of sublimating dry ice in water and water-glycerine mixtures as well as for concrete slabs being attacked by metallic or oxidic melts.

In all of these computations, the coefficient ϕ in Equ. (2.2.2-28) determining the coupling of the gas film with the liquid was found to be near unity. Consequently, the use of

$$\phi = 1 \qquad (2.2.3 - 1)$$

in Equs. (2.2.2-20,28) is very near correct for obtaining heat transfer results.

Following a proposal of Lock /18/, the ratio of the hydrodynamical boundary layer thickness between two fluids is

$$\frac{\delta_{h1}}{\delta_{h2}} = 0.844 \left(\frac{\mu_1}{\mu_2}\right)^{2/3} \left(\frac{\rho_2}{\rho_1}\right)^{1/3} \qquad (2.2.3 - 2)$$

when fluid 2 is at rest. In the gas film, the thermal boundary layer thickness equals the film thickness, and the hydrodynamic boundary layer thickness can be set as the thickness of the layer where the velocity drops from the maximum to the interface value. This is

$$\frac{\delta_{hg}}{\delta_{tg}} = \frac{1}{2} \qquad (2.2.3 - 3)$$

for $\phi = 1$. On the other hand, the ratio of the hydrodynamical and the thermal boundary layer thickness in the liquid is approximated by

$$\frac{\delta_{h\ell}}{\delta_{t\ell}} \sim Pr_{\ell}^{1/2} \quad . \qquad (2.2.3 - 4)$$

(see i.e. Schlichting /16/).

With these assumptions, a good approximation for the heat transfer results of all boundary layer calculations could be found by

$$\frac{\delta_{t\ell}}{\delta_{tg}} = 1.236\ Pr_{\ell}^{-1/2} \left(\frac{\mu_{\ell}}{\mu_g}\right)^{2/3} \left(\frac{\rho_g}{\rho_{\ell}}\right)^{1/3} \quad . \qquad (2.2.3 - 5)$$

The comparison of this equation with the results of the boundary layer theory is shown in Figure 8.

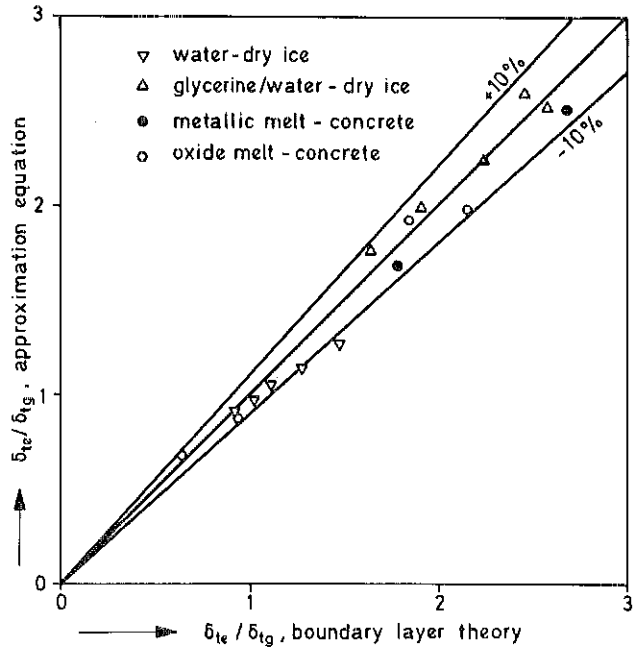

Figure 8: Comparison of Equation (2.2.3 - 4) with the results of the boundary layer theory

The boundary layer analysis was carried out for laminar film flow. However, in the model experiments with dry ice slabs of a length of 25 cm and sublimating in water and water/glycerine mixtures, transition to turbulent gas film flow occured. As shown in /17/, a good representation of the heat transfer results of these model experiments could be found when calculating the interface temperature

$$T_i = \frac{T_\ell + \left(\frac{\delta_{t\ell}}{\delta_{tg}}\right) \frac{k_g}{k_\ell} T_{dO}}{1 + \left(\frac{\delta_{t\ell}}{\delta_{tg}}\right) \frac{k_g}{k_\ell}} \qquad (2.2.3 - 6)$$

from the laminar analysis (Equ. 2.2.3-5), applying this result also on the turbulent gas film region and setting the friction coefficient f_{TP} in the turbulent film zone as function of the viscosity ratio (μ_ℓ / μ_g) determined at the interface temperature T_i.

$$f_{TP} = 3.414\ 10^{-4}\ (\mu_\ell/\mu_g)^{2/3} \qquad (2.2.3 - 7)$$

Figure 9 gives this comparison.

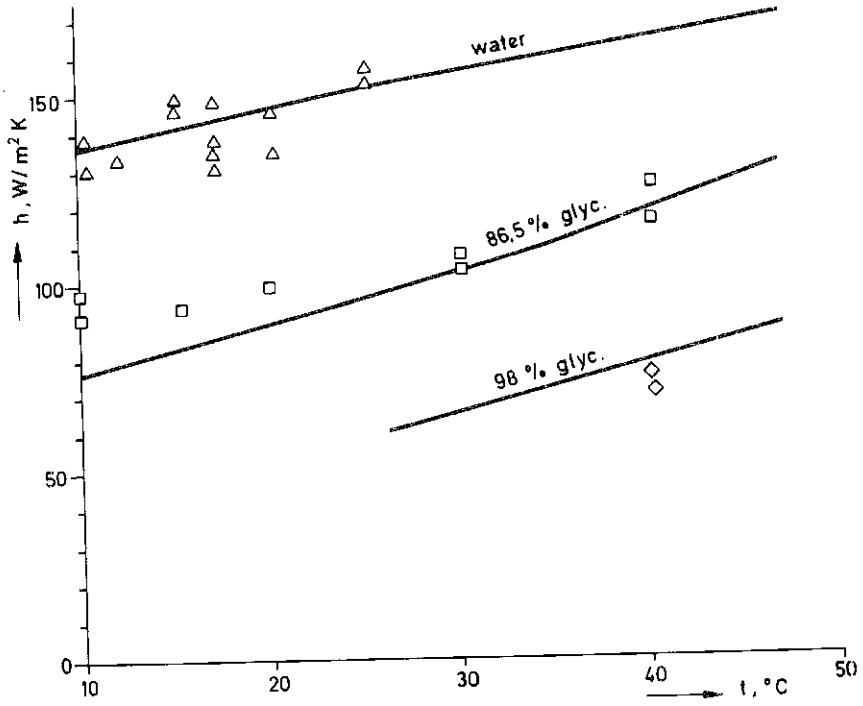

Figure 9: Comparison of experimental and calculated heat transfer results of vertical dry ice slabs sublimating in liquid pools

2.2.4 Discrete Bubble Model

During the course of the interaction of a core melt with concrete the pool temperature of the melt drops down continuously. Moreover, a concrete with a low weight fraction of gaseous decomposition, products can be attacked by the melt. So, the mass flux density of the released gases as defined in Equ. (2.2.2-1) could drop down to a value where a stable gas film can no longer exist. By defining a Reynolds number based on the mass flux

$$Re = \frac{(\dot{m}/A)\ a}{\mu_g} \qquad (2.2.4 - 1)$$

and following again the approach of Berenson /10/ for film boiling on horizontal surfaces, the minimum Reynolds-number is

$$Re_{min} = 0.045 \left(Gr \frac{\rho_g}{\rho_\ell - \rho_g}\right)^{1/2} \qquad (2.2.4 - 2)$$

when assuming the formation of one bubble per oscillation in the area λ^2.

After the Reynolds number has dropped below the minimum value, the melt will get into direct contact with the concrete surface and the heat will be transfered through a boundary layer on the melt/concrete interface driven by microconvection between the gas bubble formation sites. Such a discrete bubble model was derived by Reineke et al. /19/ for horizontal surfaces and was extended in the meantime for inclined and vertical walls /20/.

In terms of the dimensionless quantities based on the properties of the melt

$$\left.\begin{aligned} Nu_\ell &= \frac{(Q/A)\ a}{k_\ell\ (T_\ell - T_{dO})} \\ Pr_\ell &= \frac{\mu_\ell\ c_{p\ell}}{k_\ell} \\ (Pr\ Ste)_\ell &= \frac{\mu_\ell\ \Delta H_c}{k_\ell\ (T_\ell - T_{dO})} \end{aligned}\right\} \qquad (2.2.4 - 3)$$

the heat transfer is determined by

$$Nu_{\ell} = \frac{C(\alpha)^2}{6^{1/2}} \psi_g \frac{Pr_{\ell}^{0.84}}{(Pr\ Ste)_{\ell}} \frac{\rho_{water}}{\rho_g} \qquad (2.2.4 - 4)$$

with an expression taking into account the angle of inclination α

$$C(\alpha) = 1.65 + 7.47\alpha - 8.77\alpha^2 + 3.65\alpha^3 . \qquad (2.2.4 - 5)$$

As an option, the heat transfer from the melt to the concrete can be calculated in the WECHSL code only with the discrete bubble model for the whole period of interaction.

2.3 Pool Behavior

2.3.1 Bubble Size and Rise Velocity

Gas bubbles rising through the melt are responsible for the melt stirring. They also cause a swelling of the melt, so that the surface aerea for heat transfer is effectively increased. The bubble behavior is important because of the large volume fluxes of gas released, and the void fraction in the melt can be considerable.

It has been assumed in the gas film model that bubbles of uniform size and spacing are formed. This is well confirmed by experiments with simple materials such as water over dry ice. However, also in experiments with water over inhomogeneous materials, i.e. frozen xylene and carbon dioxide snow simulating the liquid and gaseous decomposition products of the concrete /8/, it could be seen that the gas bubbles have a similar average diameter as in the experiments with pure materials.

The mean equivalent sphere radius of the bubbles detatching from the gas film has been estimated in Equn. (2.2.2-9) to be

$$r_{eq} = \frac{\lambda}{4} = 2.74\ a . \qquad (2.3.1 - 1)$$

The bubble radius as estimated in the discrete bubble model is of the same order of magnitude.

For the bubble rise behavior, the bubble Reynolds number

$$Re_\ell = \frac{\rho_\ell \, r_{eq} \, u_b}{\mu_\ell} \qquad (2.3.1 - 2)$$

is important. For small Reynolds-Numbers, i.e. for small bubble dimensions or for a high kinematic viscosity of the fluid, the buoyancy forces are balanced by the friction forces:

$$\frac{4\pi}{3} r_{eq}^3 \, g \, \Delta\rho = \zeta \, \pi \, r_{eq}^2 \, \frac{\rho \, u_b^2}{2} \qquad (2.3.1 - 3)$$

where ζ is the friction coefficient, or from above equation, the bubble velocity can be written as

$$u_b = \left(\frac{8 \, g \, \Delta\rho \, r_{eq}}{3 \, \rho_\ell \, \zeta}\right)^{1/2} . \qquad (2.3.1 - 4)$$

For very small bubbles, - which are not of interest here - the friction coefficient for a rigid sphere is applicable (Stokes flow and transition region). For higher Reynolds numbers, the friction coefficient is, as proposed by Levich /21/, double as high as for Stokes flow around a rigid sphere:

$$\zeta = \frac{24}{Re_\ell} \qquad (2.3.1 - 5)$$

and the bubble rise velocity is obtained as

$$u_{bl} = \frac{1}{9} \, g \, \frac{\Delta\rho}{\rho_\ell} \, r_{eq}^2 \, \nu^{-1} . \qquad (2.3.1 - 6)$$

In low viscous fluids, the rise velocity increases up to a maximum value. Beyond this value, the rise behavior is changed completely.

The spherical cap bubbles start to oscillate and rise along zig-zag or helical lines. With increasing bubble radius, the rise velocity

decreases to reach a minimum value. Then, the rise velocity increases again. Mendelson /22/ formulated this complicated behavior in a single equation by balancing basically the inertia forces with the gravity and capillary forces. By introducing the dimensionless groups

$$\left.\begin{aligned} Eö &= \frac{g\,\rho_\ell\,r_{eq}^{\,2}}{\sigma} \\ We &= \frac{r_{eq}\,\rho_\ell\,u_b^{\,2}}{\sigma}\,, \end{aligned}\right\} \qquad (2.3.1-7)$$

the result is

$$We = Eö + 1\,, \qquad (2.3.1-8)$$

or, for the bubble rise velocity

$$u_{b2} = \left(g\,r_{eq} + \frac{\sigma}{\rho_\ell\,r_{eq}}\right)^{1/2}. \qquad (2.3.1-9)$$

For large bubbles, the capillary forces can be neglected and the rise velocity approaches

$$u_{b2}^{\,*} = (g\,r_{eq})^{1/2}. \qquad (2.3.1-10)$$

In high viscous fluids, the bubbles rise straight without oscillations. Here, the rise velocity grows continuously with increasing bubble radius and finally approaches Equation (2.3.1-10).

The effective bubble rise velocity is determined by

$$u_b = \min(u_{b1}, u_{b2}). \qquad (2.3.1-11)$$

Some data from the experimental work of Habermann and Morton /23/ is shown in Figure 10, along with the values computed by Equation (2.3.1-11).

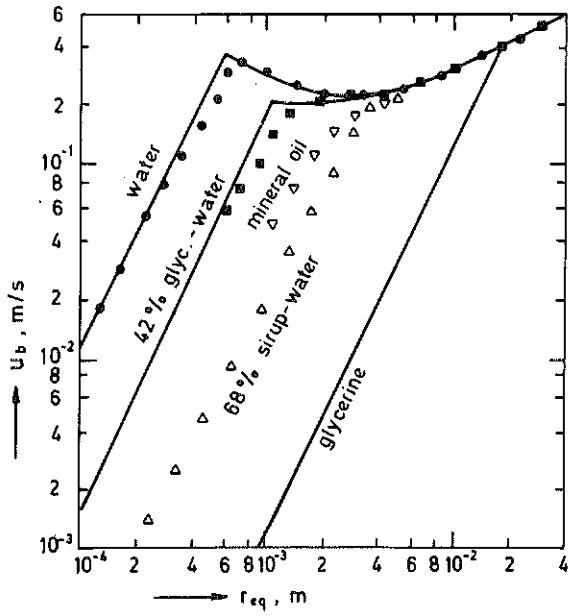

Figure 10: Rise velocity for air bubbles rising in a tank of stagnant liquid /23/

The maximum possible equivalent bubble radius is given by Levich /21/ to be

$$r_{eq\ max} = \frac{\sigma}{u_b^2} \left(\frac{12}{\rho_g\ \rho_\ell^2}\right)^{1/3} . \qquad (2.3.1 - 12)$$

When a bubble exceeds this dimension, it bursts into smaller bubbles.

2.3.2 Void Fraction

In the foregoing section, the rise behavior of a single bubble in a stagnant liquid was discussed. However, when large numbers of bubbles rise, the rise velocity is reduced to u_{bs}. Le Clair and Hamielec /24/ gave a plot of the quotient u_{bs}/u_b over the void fraction ε of the liquid with the single bubble Reynolds number Re_b as parameter. Their figure can be closely approximated by

$$\frac{u_{bs}}{u_b} = (1-\varepsilon)^n \qquad (2.3.2 - 1)$$

with

$$Re_b \leq 50: \; n = -1.14 \log(Re_b) + 4.11$$
$$Re_b > 50: \; n = -0.52 \log(Re_b) + 3.05 \qquad (2.3.2 - 2)$$

The above ratio is limited to $(u_{bs}/u_b)_{min} = 0.2$.

By introducing the artificial gas velocity as

$$v_g = \frac{(\dot{m}/A)}{\rho_g} \qquad (2.3.2 - 3)$$

the void fraction, artificial gas velocity and the rise velocity of a bubble swarm are correlated according to Nicklin /25/ by

$$\frac{v_g}{\varepsilon} = u_{bs} + v_g \; . \qquad (2.3.2 - 4)$$

By inserting Equ. (2.3.2.-1), the void fraction can be evaluated from

$$\varepsilon = \frac{v_g}{(v_g + (1-\varepsilon)^n u_b)} \qquad (2.3.2 - 5)$$

In WECHSL, the void fraction is arbitrarily limited to $\varepsilon_{max} = 0.55$.

2.3.3 Phase Segregation

It has been experimentally observed /4,5/, that a melt containing metal and oxide phases undergoes a rapid, density driven phase segregation, and that this segregation is maintained even throughout the period of the most vigorous gas flow. This behavior is modelled in the WECHSL code. It is assumed that two distinct layers are present: an upper oxide layer and a lower metal layer. In a core melt, the oxide is initially composed of a mixture of ZrO_2 and UO_2, which has, according to Ondracek /26/, a lower density than the metallic phase. This is the maximum possible density for the oxide. The accretion of molten concrete constituents in the oxide layer causes the density to become significantly lower.

2.3.4 Heat Transfer between the Molten Layers

Wehrle /27/ has studied the heat transfer between liquid layers in the presence of gas percolation using simulant materials. For liquid layers without gas percolation, heat is transfered by natural convection. Haberstroh and Reinders /28/ performed an analysis of this case based on the heat transport through a single layer heated from below and obtained

$$Nu = 0.0535 \{Gr\ Pr\}^{1/3}\ Pr^{n} \qquad (2.3.4 - 1)$$

By assuming an odd symmetric temperature profile in each layer, the heat flux transfered from the metal (index m) to the oxide (index o) layer or vice versa is

$$\left(\frac{Q}{A}\right)_{i,O} = \left| \frac{2}{\left(\frac{1}{h_m^{*}\ k_m}\right)^{3/4} + \left(\frac{1}{h_o^{*}\ k_o}\right)^{3/4}} \right|^{4/3} \left|\{T_m - T_o\}\right|^{4/3}, \qquad (2.3.4 - 2)$$

where T_m and T_o are the different bulk temperatures and

$$h_{m,o}^{*} = 0.0535\ 2^{4/3} \left(\frac{g\ \beta_{m,o}}{\nu_{m,o}^{2}}\right)^{1/3} Pr_{m,o}^{0.417}\ k_{m,o} \qquad (2.3.4 - 3)$$

is a special quantity related with the heat transfer coefficient by

$$h_{m,o} = h_{m,o}^{*} \left|\{T_{m,o} - T_i\}\right|^{1/3}. \qquad (2.3.4 - 4)$$

The interface temperature is determined by

$$T_i = T_m + \frac{\left(\frac{1}{h_m + k_m}\right)^{3/4}}{\left(\frac{1}{h_m + k_m}\right)^{3/4} + \left(\frac{1}{h_o + k_o}\right)^{3/4}} (T_o - T_m). \qquad (2.3.4 - 5)$$

Wehrle evaluated his model experiments using silicone oil/water and silicone oil/wood metal systems by determining the factor

$$\gamma = (Q/A)_i / (Q/A)_{i,O} \qquad (2.3.4 - 6)$$

describing the enhancement of the heat transfer by the gas percolation in comparison with pure thermal convection. A reasonable fit of his data is

$$\gamma = 1 + 608 \left(\frac{v_g}{u_b}\right) Ar^{-0.43} \qquad (2.3.4 - 7)$$

with the Archimedes number

$$Ar = \frac{\rho_m - \rho_o}{\rho_o} . \qquad (2.3.4 - 8)$$

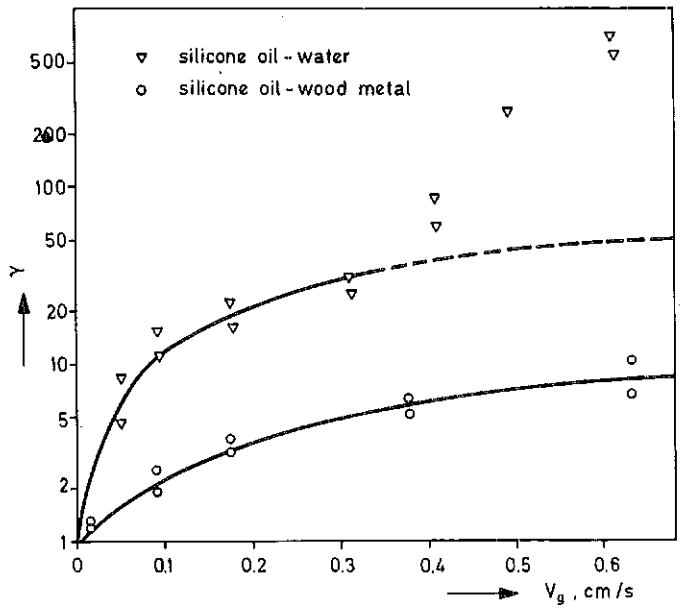

Figure 11: Enhancement of the heat transfer between liquid layers percolated by gas bubbles

In Figure 11, a comparison of the experimental data with Equ. (2.3.4-7) is given. The above equation holds as long as a distinct interface between the liquid layer exists and emulsifying effects are not decisive. The formation of emulsions, however, was only observed when the density of the liquid layers was nearly equal. In Figure 11, the onset of emulsion formation is marked by a further increase of the heat transfer in the oil/water system. In the oil/wood metal system, such a behavior could not be observed up to the maximum superficial gas velocity. However, in a core melt down accident higher superficial gas velocities may occur. On the other hand, the heat exchange between the molten layers is rather intense even without consideration of the emulsifying effects so that the temperature differences between the layers are generally small. A further improvement of the modelling would result only in a minor effect.

2.3.5 Heat Radiation from the Top of the Melt

The gas bubbles rise through the oxide layer and break through the surface. By this mechanism, heated liquid is "pumped" to the free surface and a thermal boundary layer is formed.
The heat transfer is represented by an expression similar to the microconvective heat transport induced by a discrete bubble detaching from a gas emitting wall /19/

$$Nu_{o,s} = 0.66\ Re_b^{1/2}\ Pr_o^{0.42} \qquad (2.3.5 - 1)$$

with

$$Nu_{o,s} = \frac{h_{o,s}\ r_{eq}}{k_o} \qquad (2.3.5 - 2)$$

and the bubble Reynolds-number as defined in Equ. (2.3.1 - 2)
The resulting heat flux

$$(Q/A)_{o,s} = h_{o,s}\ (T_o - T_{o,s}) \qquad (2.3.5 - 3)$$

is equated to the heat radiation from the surface to the surrounding

$$(Q/A)_{rad,s} = \varepsilon_{s\infty}\ c_0\ (T_{o,s}^4 - T_\infty^4) \qquad (2.3.5 - 4)$$

with

$$\varepsilon_{s\infty} = \frac{1}{\frac{1}{\varepsilon_{o,s}} + \frac{1}{\varepsilon_\infty} - 1} \qquad (2.3.5 - 5)$$

The resulting equation is solved for the surface temperature.

2.3.6 Oxidation Reactions

It has been observed that a large fraction of the steam and carbon dioxide bubbling through a metallic melt is reduced according to the reactions

$$Zr + 2\ H_2O \rightarrow ZrO_2 + 2\ H_2\ , \qquad (2.3.6 - 1)$$

$$Zr + 2\ CO_2 \rightarrow ZrO_2 + 2\ CO\ , \qquad (2.3.6 - 2)$$

$$2\ Cr + 3\ H_2O \rightarrow Cr_2O_3 + 3\ H_2\ , \qquad (2.3.6 - 3)$$

$$2\ Cr + 3\ CO_2 \rightarrow Cr_2O_3 + 3\ CO\ , \qquad (2.3.6 - 4)$$

$$Fe + H_2O \rightarrow FeO + H_2 \,, \qquad (2.3.6 - 5)$$

$$Fe + CO_2 \rightarrow FeO + CO \,. \qquad (2.3.6 - 6)$$

Other reactions are also theoretically possible, but it can be found in the literature that the equilibrium constants for reactions yielding Fe_2O_3, Fe_3O_4 and NiO are such that only a very small fraction of the gases can be reduced in these reactions.

Calculations based on a diffusion model /40/ show that the above reactions proceed rapidly to equilibrium. The equilibrium constants for the reactions (2.3.6-1) through (2.3.6-4) lie very near to complete reduction of H_2O and CO_2. Reactions (2.3.6-5,6), however, will not completely reduce the gases. The equilibrium constants for these reactions are approximated by

$$\log_{10} K_5 = 0.04 + \frac{301.5}{T} \qquad (2.3.6 - 7)$$

and

$$\log_{10} K_6 = 1.25 - \frac{854.3}{T} \qquad (2.3.6 - 8)$$

with the absolute temperature T in Kelvin.

Reaction (2.3.6-1) through (2.3.6-4) are strongly exothermic. Reaction (2.3.6-5) can be either endothermic or exothermic, depending on temperature, and in any case is quite small. Reaction (2.3.6-6) is weakly endothermic.

The reactions are assumed to proceed in the order Zr:Cr:Fe; so that Fe is oxidized only when all available Zr and Cr has been burnt out.

It is assumed that each bubble contains a single gas constituent; therefore, the water-gas reactions does not compete with the gas-metal reactions within the melt. The rationale for this assumption is that each bubble is probably generated from a relatively small

area of concrete. Some bubbles are expected to contain mostly CO_2, from decomposition of a lump of limestone; other bubbles will contain mostly H_2O, from decomposition of the cement matrix. However, above the melt the gases will be well mixed, and the homogeneous water gas reaction can be expected:

$$H_2O + CO \rightleftharpoons H_2 + CO_2 . \qquad (2.3.6 - 9)$$

An additional reaction considered in the WECHSL code is the thermite reaction

$$Zr + 2\ FeO \rightarrow ZrO + 2\ Fe . \qquad (2.3.6 - 10)$$

This reaction is strongly exothermic and extremely rapid. In combination with the reactions (2.3.6-1.2) the result is that any metallic zirconium will be depleted within a short period of time.

2.3.7 Material Properties

Powers and Frazier have described in /29/ the VISRHO subroutine, a method for accurate computation of densities and viscosities of magmatic melts containing silicates. This method is applied in WECHSL on the constituents of a core melt in a core melt accident respectively a thermite melt in a simulation test. The formation of $CaAl_2O_4$ is taken into account if CaO and Al_2O_3 are components of the melt.

The density of each phase is computed from the mole fraction χ_i, the molecular weight M_i, the partial molar volume V_{Mi}, the thermal coefficient of volumetric expansion β_i, and the bulk temperature T by

$$\rho = \frac{\sum_{i=1}^{n} \chi_i M_i}{\sum_{i=1}^{n} \chi_i V_{Mi} \left(1 + \beta_i (T-1613)\right)} \qquad (2.3.7 - 1)$$

In VISRHO the dynamic viscosity of a magmatic melt in Poise is obtained from

$$\mu = \exp\left\{\sum_{i=1}^{n} \chi_i D_i\right\} \qquad (2.3.7 - 2)$$

where the coefficients D_i are given in /29/ in tables for different ranges of silica contents between 35 Mol% and 85 Mol% and for temperatures ranging between 1200 °C and 1800 °C. From these tables, Arrhenius coefficients A_i, B_i are evaluated and used in WECHSL describing the temperature dependence of the coefficients D_i by

$$D_i = A_i + \frac{B_i}{T}. \qquad (2.3.7 - 3)$$

For the constituents UO_2 and ZrO_2 no data is available in /29/. For these substances, the coefficients for TiO_2 are used. The Arrhenius coefficients are extrapolated for low silica fractions to give reasonable results for pure Corium respectively pure Al_2O_3 and for high silica fractions to reproduce the viscosity data of pure silicate.

The method originally described in /29/ used coefficients which were considered to be constant within a range of silica contents. However, it has been found that the jumps in viscosity in passing from one silica range to the next can cause severe numerical disturbances under some circumstances. Therefore, linear interpolation is used to give smooth transitions.

Skoutajan et al. /30/ investigated experimentally the viscosity of Corium/silicate melts at temperatures between 1300 °C and 1600 °C. They found that the VISRHO calculations give values far below the experimental data. A much better representation of their experimental data can be found by presuming the precipitation of solid particles of the high melting oxides (i.e. UO_2, ZrO_2, CaO) between the liquidus and the solidus temperature of the melt. The empirical Kunitz-formula /31/ for liquid/solid mixtures

$$\frac{\mu_{LS}}{\mu} = \frac{1 + 0.5\,\Gamma}{(1 - \Gamma)^4} \qquad (2.3.7 - 4)$$

with

$$\Gamma = \frac{T_L - T_{LS}}{T_L - T_S} \sum_{i=1}^{n_h} \psi_i \qquad (2.3.7 - 5)$$

is used, where μ_{LS} is the viscosity of the liquid/solid mixture at a temperature T_{LS} between the liquidus temperature T_L and the solidus temperature T_S, and $\sum\psi_i$ is the sum of weight fractions of the high melting constituents (i.e. UO_2, ZrO_2, CaO).

In Figure 12, the results of the modified VISRHO calculations are compared with the experimental data. As can be seen, the measurements are located for the most part between case A (reactor concrets as given in /30/ with a 73.1 wt.-% SiO_2) and case B (87.2 wt.-% SiO_2). For 0%/100 % and 10 %/90 % Corium/concrete mixtures, the measurements have been carried out beyond the liquidus temperature, for the 30 %/70 % and 50 %/50 % Corium/concrete mixtures the measurements have been carried out between the solidus and the liquidus temperature where Equation (2.3.7-4) acts.

In the simulation experiments in the BETA test facility, the oxidic Corium melt is replaced by the oxidic part of a thermite melt which is usually Al_2O_3. Consequently, the knowledge of the viscosity of mixtures containing Al_2O_3 and SiO_2 is also important with respect to the evaluation of the simulation tests. In /29/, measurements of the dynamic viscosity of Al_2O_3/SiO_2 mixtures are compiled from the literature at temperatures between 1900 ^{o}C and 2350 ^{o}C which is always beyond the relevant liquidus temperature. Figure 13 gives the comparison of the modified VISRHO calculation with the experimental data.

For the metallic phase, the viscosity is assumed to be that of pure iron, the major metallic constituent, following the data of /32/.

Specific heat, latent heat of freezing, thermal conductivity and surface tension are computed by simple mixture theory.

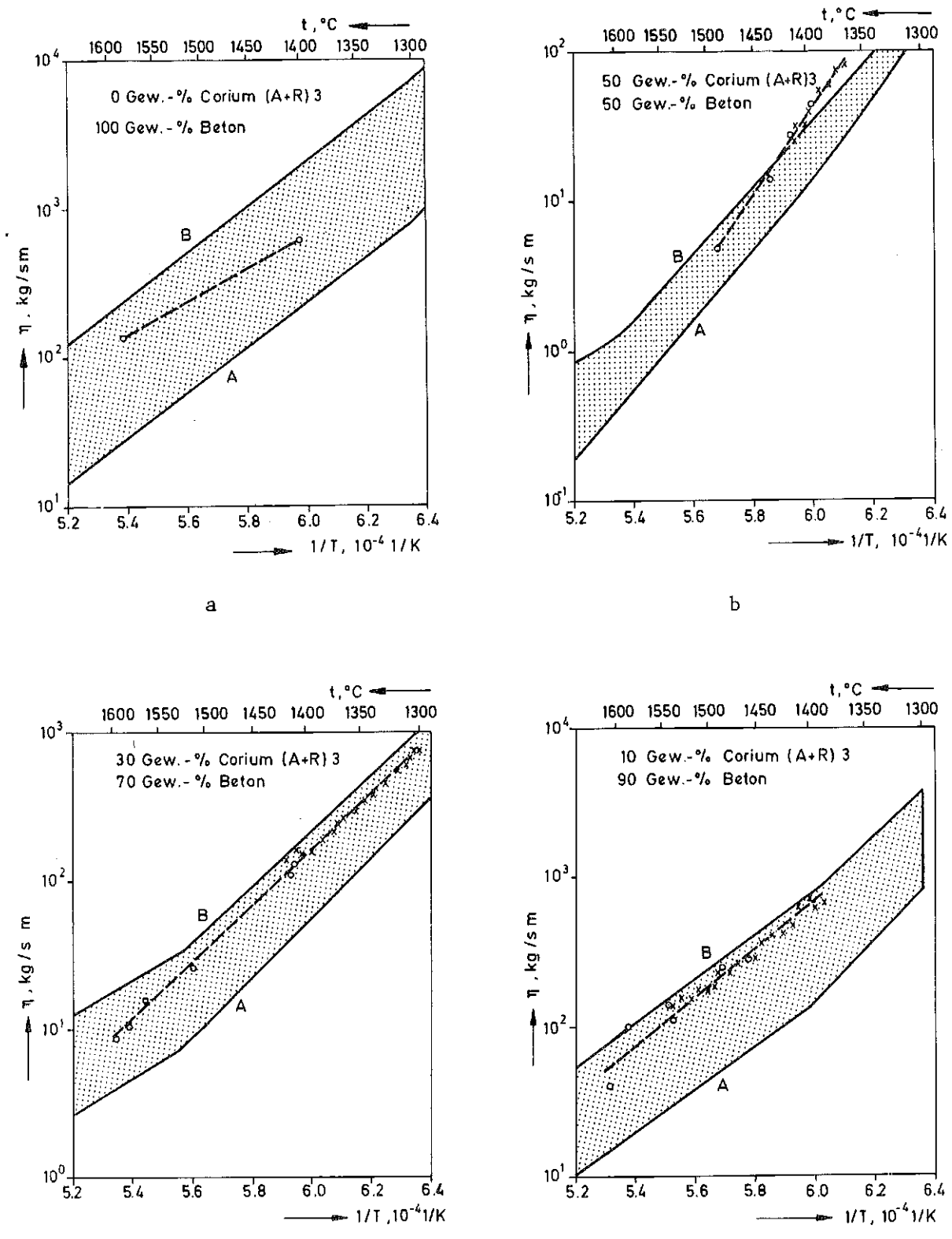

Figure 12: Comparison of viscosity measurements with calculated results of Corium mixed with siliceous concrete

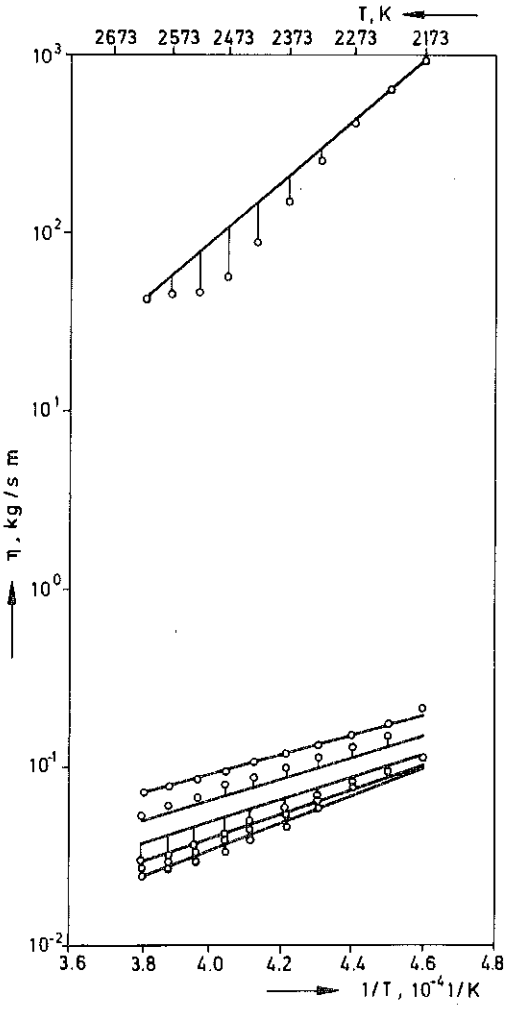

Figure 13: Comparison of viscosity measurements with computed results for molten Al_2O_3/SiO_2 - mixtures

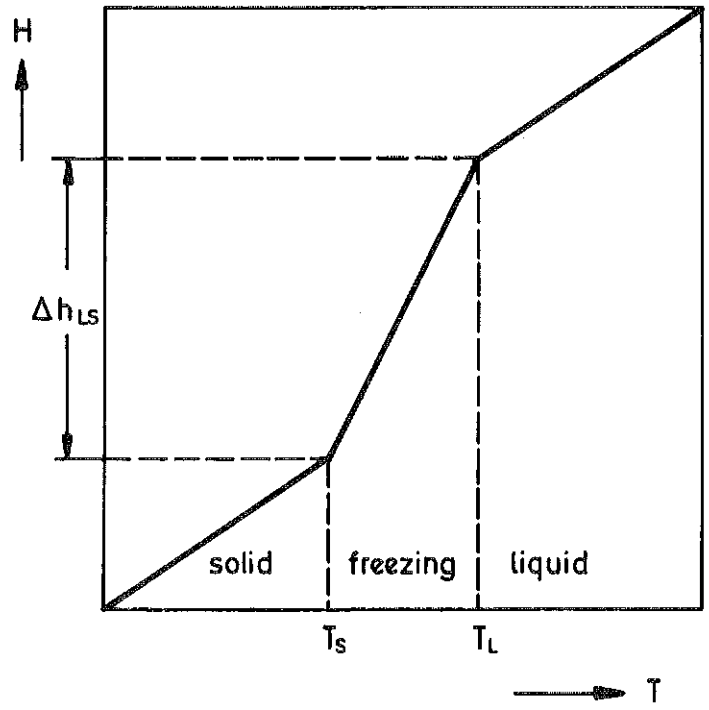

Figure 14: Enthalpy determination for each layer of the melt

Enthalpies are determined as shown in Figure 14. The enthalpy is approximated by

$$h = c\,T \qquad (2.3.7 - 6)$$

in the solid region,

$$h = c\,T + \Delta h_{LS}\,\frac{T - T_S}{T_L - T_S} \qquad (2.3.7 - 7)$$

in the region between liquidus and solidus temperature and

$$h = c\,T + \Delta h_{LS} \qquad (2.3.7 - 8)$$

in the liquid region of each molten layer. Note that it is assumed that specific heat capacity is constant over the temperature range of interest. This approximation is reasonably good for liquid metal, but it is not quite accurate for some of the oxide constituents.

2.3.8 Freezing Behavior

The solidus and liquidus temperatures of the oxide phase are computed by a method suggested by Ondracek /33/. In this procedure, the multiphase melt is reduced to a binary system having a high melting point component (the molten Corium oxides UO_2, ZrO_2 and CaO, Cr_2O_3 with melting temperatures between 2700 K and 3000 K, index 1) and a low melting point component SiO_2, FeO, $CaSiO_3$ with melting temperatures around 1800 K, index 2).

By assuming ideal mixing of the liquid components and formation of ideal mixture crystals, the van Laar Equations (see i.e. /34/ are valid:

$$\chi_L = \frac{\exp(N_L) - 1}{\exp(N_L) - \exp(M_L)} \qquad (2.3.8 - 1)$$

and

$$\chi_S = \frac{\exp(N_S) - 1}{\exp(N_S + M_S) - 1} \qquad (2.3.8 - 2)$$

with

$$N_{L,S} = \frac{\Delta H_{LS,2}}{\mathbf{R}}\left(\frac{1}{T} - \frac{1}{T_{(L,S),2}}\right) \qquad (2.3.8 - 3)$$

and

$$M_{L,S} = \frac{\Delta H_{LS,1}}{\mathbb{R}} \left(\frac{1}{T_{(L,S),1}} - \frac{1}{T} \right) \quad , \qquad (2.3.8 - 4)$$

where

χ - molar concentration ,
ΔH_{LS} - molar latent heat of freezing ,
$T_{L,S}$ - liquidus resp. solidus temperature ,
T - melt bulk temperature ,
$\mathbb{R}$ - ideal gas constant .

The data for the molar latent heat of freezing ΔH_{LS} given in the literature ranges for the constituents of the oxide melt between 7680 J/mol for SiO_2 and 138 000 J/mol for FeO.

By selecting values for ΔH_{LS} and $T_{L,S}$ of the low and high melting point components and by solving the above equations, the composition dependent liquidus and solidus temperatures of the fictitious two-phase melt with ideal mixing behavior are found.

Skokan et al. /35/ measured the composition dependent solidification temperature for mixtures of Corium at different oxidation levels with different types of concrete. As shown in Figure 15, their experimental data for silicaceous concrete can be reproduced with sufficient accuracy when selecting for completely oxidized Corium (A+R, E+R) 3

$$T_{S,1} = 2323 \text{ K}, \ \Delta H_{LS,1} = 80\,000 \text{ J/mol} ,$$
$$T_{S,2} = 1423 \text{ K}, \ \Delta H_{LS,2} = 24\,840 \text{ J/mol} , \qquad (2.3.8 - 5)$$

and for partly or not oxidized Corium (A+R, E+R)1,2

$$T_{S,1} = 2723 \text{ K}, \ \Delta H_{LS,1} = 110\,000 \text{ J/mol} ,$$
$$T_{S,2} = 1423 \text{ K}, \ \Delta H_{LS,2} = 14\,000 \text{ J/mol} . \qquad (2.3.8 - 6)$$

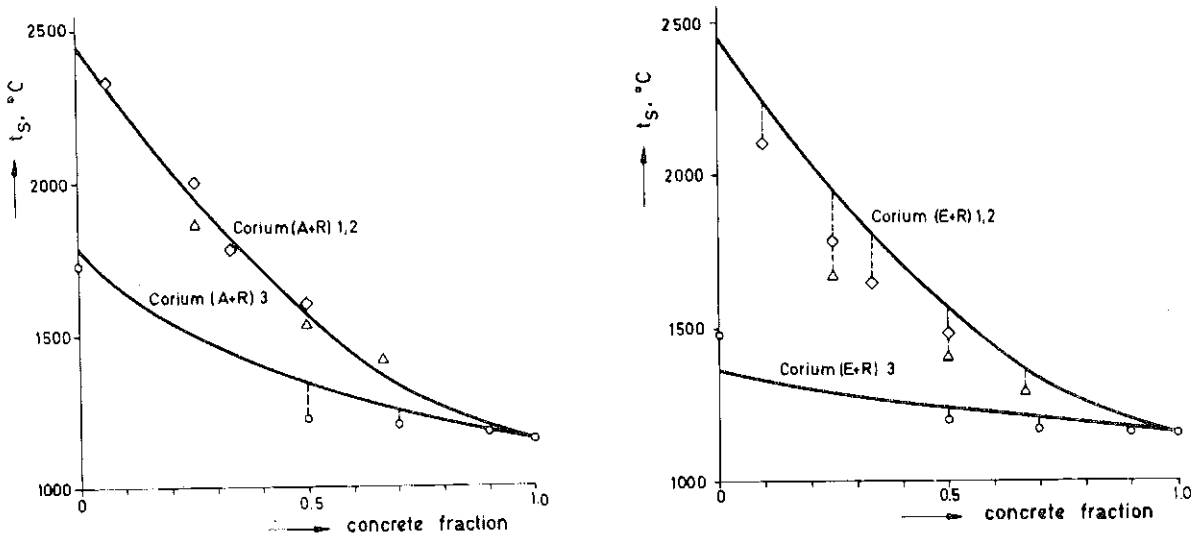

Figure 15: Solidification temperature of Corium/concrete mixtures: Comparison of measured and calculated values

It should be noted that the liquidus and solidus points in the oxide phase are constantly being depressed as the silicaceous concrete constituents dilute the oxide material. At the same time, the melt temperature drops because of cooling. The apparent specific heat of the melt is higher between the solidus and liquidus temperatures because of partial solidification of the melt; this naturally decreases the cooling rate.

For calcareous concrete without any silicates, the concept of ideal mixing is not applicable. The measurements /35/ show a minimum for the solidification temperature at 50 wt.-% Corium/ 50 % wt.-% calcareous concrete indicating strong deviations from the ideal mixing behavior.

If the core melt accident sequence freezing is likely, the principal constituents of the metal melt are Cr, Fe, and Ni. Consequently, the phase diagram of this ternary system must be considered for the solidification process. A single fit to the ternary Cr-Fe-Ni phase diagram was constructed by Bartel et al. /36/. The liquidus and solidus temperatures in Kelvin are approximated by

$$
\begin{aligned}
T_L = \max\ (&2130 - 510\ \psi_{Fe} - 1140\ \psi_{Ni},\\
&1809 - 90\ \psi_{Cr} - 440\ \psi_{Ni},\\
&1728 - 200\ \psi_{Cr} - 40\ \psi_{Fe},\\
&1793 - 230\ \psi_{Cr} - 130\ \psi_{Ni})\\
T_S = \max\ (&2130 - 730\ \psi_{Fe} - 3310\ \psi_{Ni},\\
&1809 - 90\ \psi_{Cr} - 560\ \psi_{Ni},\\
&1728 - 250\ \psi_{Cr} - 100\ \psi_{Fe},\\
&1783 - 310\ \psi_{Cr} - 140\ \psi_{Ni},\\
&1613)
\end{aligned}
\qquad (2.3.8 - 7)
$$

where ψ_{Cr}, ψ_{Fe}, and ψ_{Ni} are the weight fraction of the metal melt. The current coding ignores the presence of other elements in the metallic phase, and renormalizes so that

$$\psi_{Cr} + \psi_{Fe} + \psi_{Ni} = 1\ . \qquad (2.3.8 - 8)$$

In general, the surface temperatures of the molten pool are below the bulk temperatures. Consequently, these temperatures will drop at first below the freezing temperature of the melt and crust formation will occur. The crust growth of course is a transient process. But, the pool temperatures change rather slowly so that the assumption that always the stable crust thickness with steady state heat conduction through the crust will apply seems to be justified.

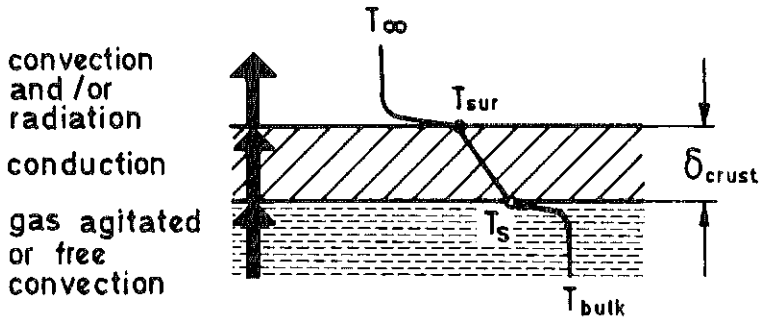

Figure 16: Crust formation model

A conceptual model for this process is sketched in Figure 16. The heat is transfered from the bulk to the crust surface which is at solidification temperature T_S by a convective process to give

$$(Q/A) = h_{conv} (T_{bulk} - T_S) \; ; \qquad (2.3.8 - 10)$$

this heat flux density is transfered by heat conduction through the crust

$$(Q/A) = \frac{k}{\delta_{crust}} (T_S - T_{sur}) \qquad (2.3.8 - 11)$$

and from the crust surface, the heat is released by convective and/or radiative processes:

$$(Q/A) = h_{sur} (T_{sur} - T_\infty) \; . \qquad (2.3.8 - 12)$$

So, the unknown surface temperature can be determined by

$$T_{sur} = T_\infty + \frac{h_{conv}}{h_{sur}} (T_{bulk} - T_S) \; , \qquad (2.3.8 - 13)$$

and the crust thickness follows from

$$\delta_{crust} = \frac{k}{h_{conv}} \frac{T_S - T_{sur}}{T_{bulk} - T_S} \; . \qquad (2.3.8 - 14)$$

At the beginning of the crust formation process, the convective heat transfer from the bulk to the surface is through gas agitation. As a first approach it is assumed that in the first period of crust formation all gas release nodes remain active. Consequently, the gas driven heat transfer models can be applied without changes until the crust has reached a thickness of 0.5 cm. In the further process of crust growths, an increasing number of gas release nodes close. This behavior is approximated by assuming that the convective heat transfer from the bulk to the crust changes linearly from gas agitated convection to free convection when the crust thickness is between 0.5 and 1.5 cm.

Numerous experiments with model substances are planed to give a better physical understanding of the process of crust formation in order to allow an improved modelling.

Because the heat transfer models are only applicable to liquid pools, the results of the code are not valid after the pool temperature drops below the solidus point of either phase. However, this problem is recognized and the code will be extended to be applicable also in the regime, where one or both phases are frozen.

2.4 Supplementary Features of the WECHSL Code

2.4.1 Cavity Shape

The cavity is constrained to be axially symmetric; subject to this constraint, the shape is entirely free. Because of the variation in erosion rate around the periphery and the constantly changing level of the melt, the cavity shape undergoes permanent alteration.

The pool is divided into segments, chosen so that the peripherial lengths Δs are equal, except that the phase boundary and the upper surface are always at segment boundaries. Each segment is in the form of a conical frustrum between two nodes (Figure 17).

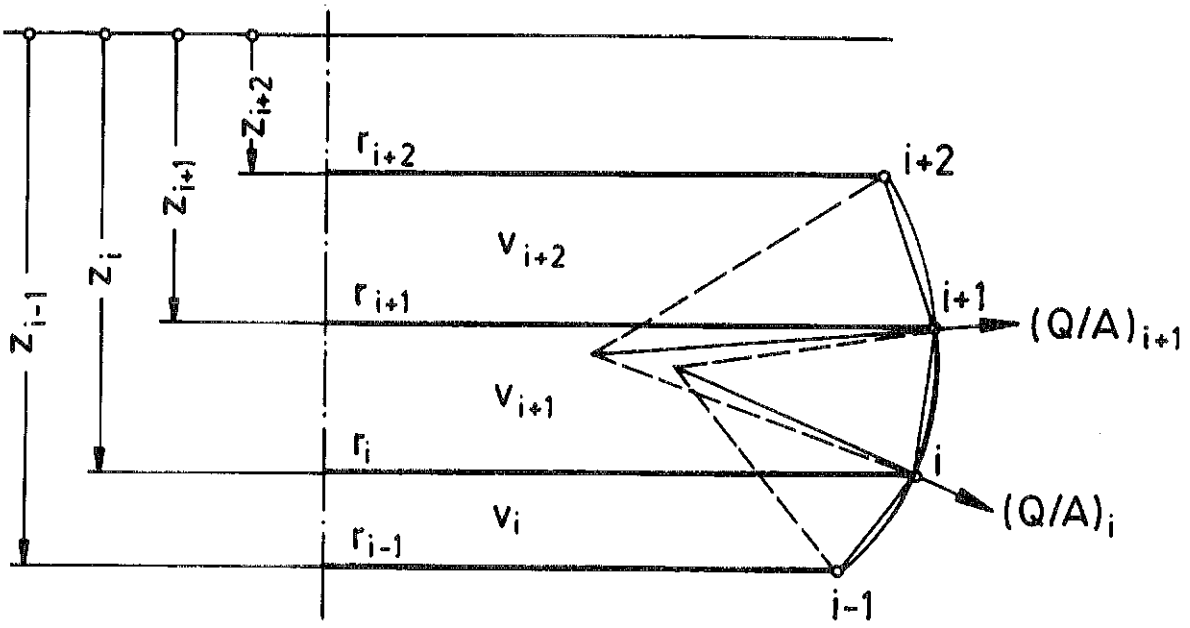

Figure 17: Cavity Geometry

The heat fluxes and the resulting erosion velocity are computed at the nodes; it is assumed that the velocity vector at each node is in the direction of the outward normal to the rotational symmetric segment limited by a circle through that node and the two adjoining nodes. New node positions are computed, and the periphery is rezoned so that all nodes are again equidistant from each other (except the nodes at the phase boundary and at the free surface). This rezoning introduces a rough form of filtering, so that bizarre cavity shapes caused by numerical problems are inhibited.

Because of time limitations, the true velocity at each node is only computed at every fifth time step (time τ^j), using the detailed procedure given in the sections 2.2.2 and 2.2.3. At the intervening time steps τ^{j+n}, n = 1..4, the erosion velocity on the bottom surface $\dot{\zeta}_{bott}^{\,j+1}$ is computed for the current pool temperature, and the velocities at all other nodes i of the cavity are computed by

$$\dot{\zeta}_i^{\,j+n} = \dot{\zeta}_i^{\,j+n-1} \frac{\dot{\zeta}_{bott}^{\,j+n}}{\dot{\zeta}_{bott}^{\,j+n-1}} \,. \qquad (2.4.1 - 1)$$

In this procedure, the distribution of the metal and the oxide layer in the cavity changing with time is considered.

It should be pointed out that the velocity vector is based on a rotational symmetric segment limited by a circle through three adjacent nodes, whereas the surface integral of heat flux and the new volumes are computed as if the cavity is composed of conical frusta. The new positions of the nodes are based on the first assumptions. This could lead to discrepancies between mass and volume. The mass discrepancy has been checked for a number of typical runs and found to amount less than 1 % after several thousand time steps if the cavity zoning is sufficiently fine.

2.4.2 Energy Balance

The internal heat sources can be prescribed in WECHSL time dependent for each layer of the melt. The energy flux balance considers the energy gain by these internal sources and by the enthalpy fluxes into each phase; the energy gain or loss by interchange of energy between the phases and by exothermal or endothermal chemical reactions, and the energy losses from each phase by heat transfer to the concrete, enthalpy fluxes out of the phase, and heat radiation from the upper surface to the environment.

At each time step, properties are computed with the bulk temperatures and the melt composition from the previous time step; heat transfer rates are computed on the basis of these properties. New temperatures for the time τ^{j+1} are then computed by the approximate relationship

$$H^{j+1} - H^{j} = \sum_{i} Q_i^{\,j} \, \delta\tau \,, \qquad (2.4.2 - 1)$$

where H is the total enthalpy of the phase, $\sum_i Q_i$ is the net rate of energy change (i.e. the algebraic sum of energy gains and losses) evaluated at the time τ^{j}, and

$$\delta\tau = \tau^{j+1} - \tau^{j} \qquad (2.4.2 - 2)$$

is the time step.

This expression is not precisely centered; the rate of energy change would be more correctly evaluated at $\tau^{j+1/2}$. However, material properties and heat rates vary only slightly during a time step, provided $\delta\tau$ is sufficiently small. In the code, $\delta\tau$ is chosen in a way that the relative temperature change $\Delta T/T$ is always less than $2 \cdot 10^{-4}$ in each time step.

An alternate procedure would be to compute properties and energy rates at the beginning and the end of the time step and to center the energy balance; this would effectively double the computation time, however, the increase in accuracy would be small.

An integrated energy balance is maintained and can be printed out periodically. Because of numerical round off and approximations, the enthalpy at any time will not be identically equal to that computed from the initial enthalpy and the integrated gains and losses. However, the error is always less than 1 % and is normally insignificantly small.

3. Instructions for the Use of the Code

3.1 WECHSL Code Characteristics

The WECHSL Code is at present operational on the IBM/370 computer system at Kernforschungszentrum Karlsruhe. The code is written in FORTRAN IV and takes input and output data in SI units. The amount of print output and of plot output data is user controlled.

The WECHSL Code is capable of restart. The following input and output files must be provided:

- data input file (IRD=5)
- print output file (IWT=6)
- common block input file (ICOR=9)
- common block output file (ICOW=10).

If plot output is required, a further file must be allocated:

- plot file (IPL=8).

The principal structure of the MAIN program operating the WECHSL subroutine is shown in Figure 18. The program starts by reading the variable ISTART from the data input file.

For an initial WECHSL run, ISTART=0. In that case, the subroutine WECHSL (Figure 19) is entered directly and the further data input is required by the subroutine READIN. Then, the time loop is executed until a time limit prespecified in the subroutine READIN is exceeded. If the downward erosion is reduced to zero or if both the metal and the oxide layers are frozen, the time loop will be aborted before the time limit is reached. After terminating the WECHSL execution, the common block data will be catalogued on the common block output file.

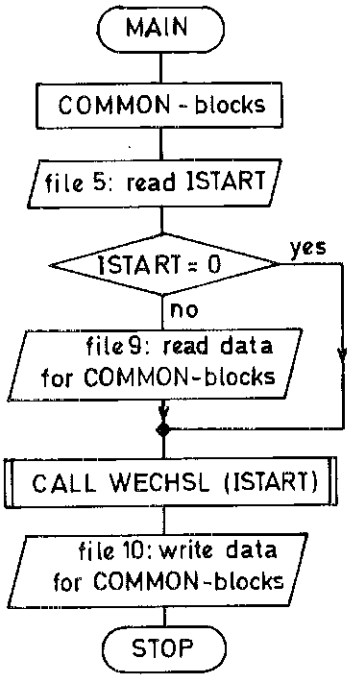

Figure 18: Principal structure of the MAIN program

For a restart WECHSL run, i.e. continuating the execution of the same problem, ISTART≠0. Then, the catalogued common block data are read from the common block input file in the MAIN program. After entering the subroutine WECHSL, some selected input parameters can be modified by means of the subroutine REREAD before the time loop begins.
The problem can be restarted as many times as desired.
Besides the catalogue output on the common block output file, the information output can also be seen in Figure 19. In the time loop, the print output is executed when the print time prescribed by the user is exeeded. Then, the new print time is calculated by summing up the present print time interval. In equivalence, plot data is written on the plot file when the plot time is exeeded. After termination of the time loop, a final print and plot output of the complete final cavity coordinates is executed.
In the next sections, the input data for the subroutines READIN and REREAD will be described in detail. Furthermore, the WECHSL output on the print and plot files will be presented.

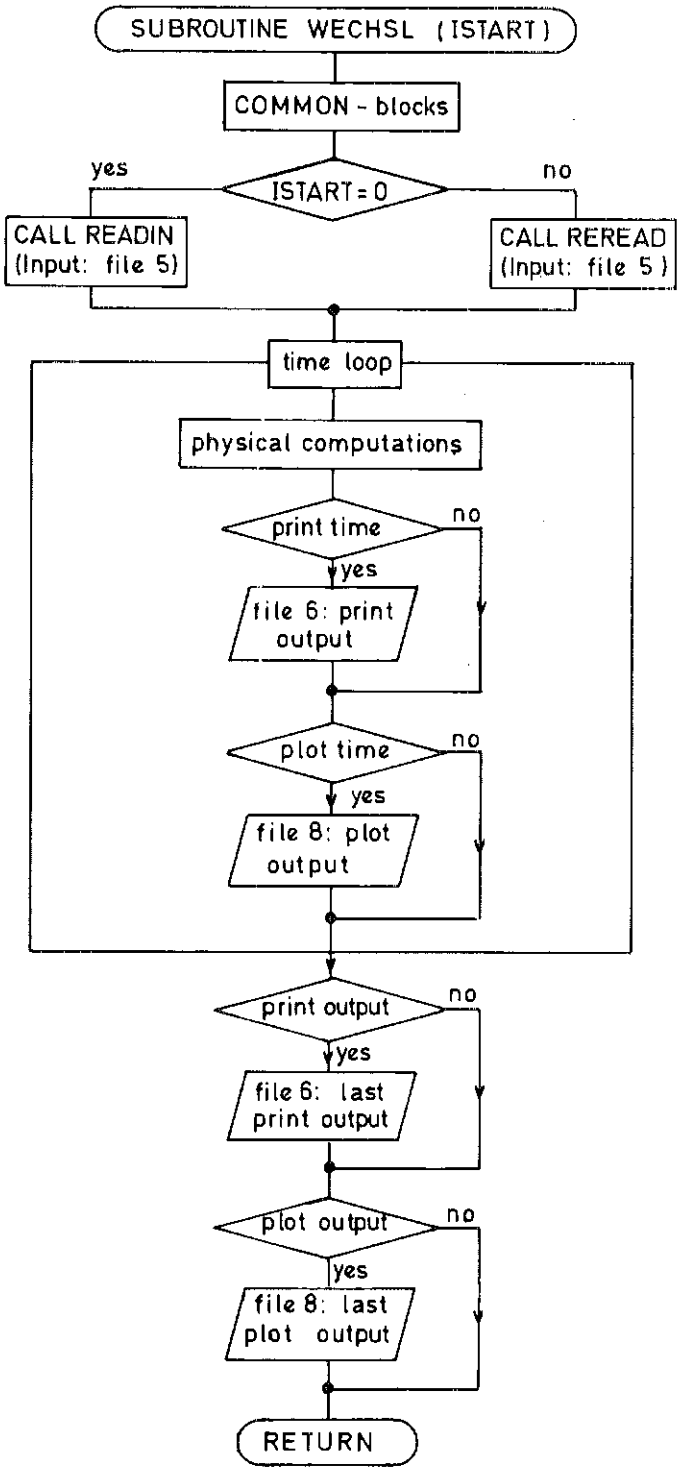

Figure 19: Simplified layout of the WECHSL subroutine

3.2 Input Description for the Subroutine READIN

The number of input data cards is variable, and depends on the type of the problem. These cards which must always be present are marked with the symbol *.

Data Cards

* Card 1: Format(20a4) - 80 columns of alphanumeric problem identification.

* Card 2: Format(i5) - Option for the heat transfer model from the molten pool to the concrete.

  Columns 1 - 5: IBLAS = 0: Gas film model for high gas mass fluxes or after the formation of massive crusts. When the pool remains liquid and the gas mass flux drops below a minimum value, the heat transfer is calculated with the discrete bubble model.

  IBLAS = 1: Discrete bubble model in the whole region.

Cards 3,4,5, and 6 are to be used for simulation tests in which a known quantity of melt is poured into or splashed out of the crucible. When the code is to be used only for meltdown accidents, these cards must be present, but all variables can be entered as zero.

* Card 3: Format(2e10.3) - Thermite addition.

  Columns 1 - 10: WTHERM - Rate of thermite addition, kg/s.

  Columns 11 - 20: THERM - Final time for thermite addition, s.

Thermite is assumed to be added at a uniform rate of WTHERM kg/s for THERM seconds.

* Card 4: Format(3e10.3) - Steel pouring

  Columns 1 - 10: WSTL - Rate of steel addition, kg/s.

  Columns 11 - 20: ZSTL - Final time for steel addition, s.

  Columns 21 - 30: TSTL - Temperature of added steel, K.

Steel pour is assumed to take place at a constant rate of WSTL kg/s, at a temperature of TSTL Kelvin, for TSTL seconds.

* Card 5: Format(3e10.3) - Steel splashout.
  Columns 1 - 10: WOUT - rate of steel splashout, kg/s.
  Columns 11 - 20: START - Time at which splashout begins, s.
  Columns 21 - 30: END - Time at which splashout ends, s.

Steel is removed at a constant rate of WOUT kg/s from START seconds to END seconds.

* Card 6: Format(3e10.3) - Oxide splashout.
  Columns 1 - 10: WOUX - Rate of oxide splashout, kg/s.
  Columns 11 - 20: STOX - Time at which oxide splashout begins, s.
  Columns 21 - 30: ENOX - Time at which oxide splashout ends, s.

Oxide is removed at a constant rate of WOUX kg/s from STOX seconds to ENOX seconds.

* Card 7: Format(8e10.3) - Concrete description
  Columns 1 - 10: FC1 - Weight fraction $CaCO_3$
  Columns 11 - 20: FC2 - Weight fraction $Ca(OH)_2$
  Columns 21 - 30: FC3 - Weight fraction SiO_2
  Columns 31 - 40: FC4 - Weight fraction H_2O
  Columns 41 - 50: RBR - Reinforcing steel, kg steel/kg concrete.
  Columns 51 - 60: TSB - Melt temperature, K.
  Columns 61 - 70: HB - Concrete decomposition enthalpy, J/kg.
  Columns 71 - 80: DENSC - Concrete density, kg/m^3.

See Note 1.

Cards 8,9,10, and 11 set up the liquidus and solidus curves for the oxide phase. A high melting point group and a low melting point group are considered. See Note 2.

* Card 8: Format(10i5) - Low temperature group.
  Columns 1 - 5: NCOM1 - Number of components in low temperature group
  $1 \leq NCOM1 \leq 5$
  Columns 5 - 10: ICOM(1) - Index of first component in the low temperature group.
  Repeat up to ICOM1(NCOM1), as required.
  Indices for the components are as follows:
  1 = UO_2
  2 = ZrO_2
  3 = FeO
  4 = CaO

5 = SiO_2
6 = Al_2O_3

* Card 9: Format(3e10.3) - Properties of the low temperature group.
Columns 1 - 10: DHS1 - Effective latent heat of melting, J/mol.
Columns 11 - 20: TS1 - Solidus temperature for 'pure' low temperature group.
Columns 21 - 30: TL1 - Liquidus temperature for 'pure' low temperature group.

* Card 10: Format(10i5) - High temperature group.
Columns 1 - 5: NCOM2 - Number of components in high temperature group
$1 \leq NCOM1 \leq 5$
Columns 5 - 10: ICOM2(1) - Index of first component in the high temperature group.
Repeat up to ICOM2(NCOM2), as required.
Indices for the components are the same as for the low temperature group.

* Card 11: Format(3e10.3) - Properties of the high temperature group.
Columns 1 - 10: DHS2 - Effective latent heat of melting, J/mol.
Columns 11 - 20: TS2 - Solidus temperature for 'pure' high temperature group.
Columns 21 - 30: TL2 - Liquidus temperature for 'pure' high temperature group.

* Card 12: Format(8e10.3) - Initial oxide description.
Columns 1 - 10: WT(1) - Initial mass of UO_2, kg.
Columns 11 - 20: WT(2) - Initial mass of ZrO_2, kg.
Columns 21 - 30: WT(3) - Initial mass of FeO, kg.
Columns 31 - 40: WT(4) - Initial mass of CaO, kg.
Columns 41 - 50: WT(5) - Initial mass of SiO_2, kg.
Columns 51 - 60: WT(6) - Initial mass of Al_2O_3, kg.
Columns 61 - 70: WCR2O3 - Initial mass of Cr_2O_3, kg.
Columns 71 - 80: TO - Temperature, K.
See Note 3.

Cards 13 and 14 give the internal energy sources in the oxide as a function of time.

* Card 13: Format(i5)
Columns 1 - 5: NIO - Number of time power points for oxide.
$0 \leq NIO \leq 10$. See Note 4

Card 14: Not used if NIO = 0.
Format(8e10.3) - Time,power points (4 points per card)
Columns 1 - 10: TIO(1) - Time for first point, s.
Columns 11 - 20: QIO(1) - Power for first point, W.
Repeat up to TIO(NIO),QIO(NIO), using additional cards, if required.
See Note 5.

* Card 15: Format(5e10.3) - Initial metal description.
Columns 1 - 10: WT(7) - Initial mass of Fe, kg.
Columns 11 - 20: WT(8) - Initial mass of Zr, kg.
Columns 21 - 30: WT(9) - Initial mass of Cr, kg.
Columns 31 - 40: WT(10) - Initial mass of Ni, kg.
Columns 41 - 50: TM - Temperature, K.
See Note 6.

Cards 16 and 17 give the internal energy sources in the metal as a function of time.

* Card 16: Format(i5)
Columns 1 - 5: NIM - Number of time power points for metal.
$0 \leq NIM \leq 10$.
Card 17: Not used if NIM = 0.
Format(8e10.3) - Time,power points (4 points per card)
Columns 1 - 10: TIM(1) - Time for first point, s.
Columns 11 - 20: QIM(1) - Power for first point, W.
Repeat up to TIM(NIM),QIM(NIM), using additional cards, if required.
See Note 7.

* Card 18: Format(2e10.3) - Times
Columns 1 - 11: DT - Initial time step, s. See Note 8.
Columns 11 - 20: TF - Final time, s. See Note 9.

Cards 19 and 20 give the printout time intervals.

* Card 19: Format(i5)
Columns 1 - 5: NTPR - Number of different printout intervals.
$2 \leq NTPR \leq 10$.
* Card 20: Format(8e10.3) - Printout intervals
Columns 1 - 10: TPR(1) - Start time for first printout interval, s
Columns 11 - 20: DPR(1) - First printout interval, s.
Repeat as necessary up to TPR(NTPR),DPR(NTPR) using up to four points

per card. Use additional cards as required. See Note 10.

Cards 21 and 22 give the ambient atmospheric pressure as a function of time.

* Card 21: Format(i5)
  Columns 1 - 5: NPP - Number of time-pressure points.
  $0 \leq NPP \leq 10$.
* Card 22: Format(8e10.3) - Time-pressure points.
  Columns 1 - 10: TP(1) -First time, s
  Columns 11 - 20: PP(1) -First pressure, bar
  Repeat as necessary up to TP(NPP),PP(NPP) using up to four points per card. Use additional cards as required. See Note 11.

Cards 23 and 24 give the ambient temperature for radiation from the top of the melt as a function of time.

* Card 23: Format(i5)
  Columns 1 - 5: NTT - Number of time-temperature points.
  $0 \leq NTT \leq 10$.
* Card 24: Format(8e10.3) - Time-temperature points.
  Columns 1 - 10: TIT(1) -First time, s
  Columns 11 - 20: TAM(1) -First temperature, K.
  Repeat as necessary up to TIT(NTT),TAM(NTT) using up to four points per card. Use additional cards as required. See Note 12.

Cards 25 and 26 give the initial cavity shape. The card types and numbers depend on the value given in card 25.

* Card 25: Format(i5)
  Columns 1 - 5: NB - Initial cavity shape option.
  If $NB \geq 2000$: Option I
  If $1000 \leq NB < 1500$: Option II
  If $1500 \leq NB < 2000$: Option IIa
  If $NB < 1000$: Option III

Option I : The initial cavity shape is a hemisphere/cylinder.

* Card 26: Format(4e10.3)
  Columns 1 - 10: DPHI - Initial central angle between points in hemisphere, degrees.
  Columns 11 - 20: DELZ - Initial interval between points in cylinder, m.
  Columns 21 - 30: R0 - Initial radius of hemisphere, m.

Columns 31 - 40: ZMX - Initial total height of cavity, m.

See Note 13.

Option II : The initial shape is a cylinder with rounded corners.

* Card 26: Format(2i5,4e10.3)

Columns 1 - 5: NR - Initial number of points on the flat part of the cavity floor.

Columns 5 - 10: NC - Initial number of points in the rounded corner.

Columns 11 - 20: RO - Initial radius of cylinder, m.

Columns 21 - 30: RKL - Initial radius of corner, m.

Columns 31 - 40: DELZ - Initial interval between points in cylindrical section, m.

Columns 41 - 50: ZMX - Initial height of cavity, m.

See Note 14.

Option IIa: Additional input for conical section on the top of the cylinder.

Card 27: Format(2e10.3)

Columns 1 - 10: ZMXE - Total height of the cavity, m.

Columns 11 - 20: WIN - Angle of inclination, deg.

See Note 15.

Option III: Arbitrary initial shape. There are NB initial points.

* Card 26: Format(8e10.3)

Columns 1 - 10: RCAV(1) - Radius of first point, m.

Columns 11 - 20: YCAV(1) - Height of first point, m.

Continue up to RCAV(NB),YCAV(NB), with four points per card. Use as many continuation cards as necessary. See Note 16. Note 14 also applies.

* Card 28: Format(e10.3)

Columns 1 - 10: SMX - Interval between points to be used during the running of the program in m. All points will be set to the same peripherial distance apart. See Note 17.

Cards 29 and 30 give the printing and plotting options. Card 31 is not used unless a plot file is to be written.

* Card 29: Format(7i5) - Print options.

Columns 1 - 5: KTEM - Temperature print option.

Columns 6 - 10: KPROP - Properties print option.

Columns 11 - 15: KINT - Interface print option.

Columns 16 - 20: KMAS - Mass print option.

Columns 21 - 25: KBAL - Heat balance print option.

Columns 26 - 30: KGAS - Gas release print option.
Columns 31 - 35: KCAV - Cavity shape print option.
Columns 36 - 40: KDIAG - Diagnostic print option.
If any of the quantities is greater than zero, the corresponding print option will be exercized. A zero value bypasses this print option.

* Card 30: Format(7i5) - Plot options.
Columns 1 - 5: JTEM - Temperature plot file option.
Columns 6 - 10: JPROP - Properties plot file option.
Columns 11 - 15: JINT - Interface plot file option.
Columns 16 - 20: JMAS - Mass plot file option.
Columns 21 - 25: JBAL - Heat balance plot file option.
Columns 26 - 30: JGAS - Gas release plot file option.
Columns 31 - 35: JCAV - Cavity shape plot file option.
If any of the quantities is greater than zero, the corresponding plot file will be written. A zero value bypasses the corresponding plot option.
Card 31: Format(2e10.3)
Columns 1 - 10: TPL - First time to write plot files, s.
Columns 11 - 20: DPL - Time interval for writing plot files, s.

Note 1: The weight fraction of Al_2O_3 is assumed to be (1.-FC1-FC2-FC3-FC4).

Note 2: For simulation of a core melt down accident, the high temperature group would normally be UO_2 and ZrO_2. Note, however, that very small amounts of iron oxide drastically reduces the melting point, and the reduced melting point should be used here. The low temperature group would normally be the concrete constituents, i.e. CaO and SiO_2. The latent heat is due to phase change only, and is not equivalent to the decomposition enthalpy.

Note 3: The problem must start with a finite mass of oxides.

Note 4: If NIO=0, the code resets NIO=2,TIO(1)=0.,QIO(1)=0.,TIO(2)=10^{10}, QIO(2)=0.

Note 5: TIO(I+1) must be greater than TIO(I), for all I.

Note 6: The initial mass of metal can be zero.

Note 7: The provisions of Note 4 and 5 apply also for metal

Note 8: The initial time step should be chosen so that the temperature change is small, say $\leq$ 5 K. It is suggested that an initial trial be made with a roughly estimated time step, and that the time step be varied upward and downward by a factor of two. Too large a time step will cause instability. Too small a time step will cause built up of round off errors.
Note 9: If the downward erosion is reduced to zero or if metal and oxide are are frozen, the program will stop before TF is reached.

Note 10: TPR(I+1) must be greater than TPR(I).

Note 11: TP(I+1) must be greater than TP(I).

Note 12: TIT(I+1) must be greater than TIT(I).

Note 13: The cavity must be deep enough to contain the entire melt including the effects of level swell. The program will not allow the cavity to run over.

Note 14: The maximum allowable number of points is 300. However, the initial shape should not use more than 150 points in order to allow for cavity growth.

Note 15: WIN is the angle between the conical part and the vertical centre line of the crucible.

Note 16: If SMX is too small, an excessive number of cavity points will be used. If SMX is too large, much of the cavity detail will be lost.

3.3 Input Description for the Subroutine REREAD

Data Cards

* Card 1: Format(20a4) - 80 columns of alphanumeric problem identification.

* Card 2: Format(e10.3) - Time
  Columns 1 - 10: TF - Final time, s. See Note 9.

Cards 3 and 4 give the printout time intervals.

* Card 3: Format(i5)

  Columns 1 - 5: NTPR - Number of different printout intervals.

  $2 \leq NTPR \leq 10$.

* Card 4: Format(8e10.3) - Printout intervals

  Columns 1 - 10: TPR(1) - Start time for first printout interval, s
  Columns 11 - 20: DPR(1) - First printout interval, s.

  Repeat as necessary up to TPR(NTPR),DPR(NTPR) using up to four points per card. Use additional cards as required. See Note 10.

Cards 5 and 6 give the printing and plotting options. Card 7 is not used unless a plot file is to be written.

* Card 5: Format(7i5) - Print options.

  Columns 1 - 5: KTEM - Temperature print option.
  Columns 6 - 10: KPROP - Properties print option.
  Columns 11 - 15: KINT - Interface print option.
  Columns 16 - 20: KMAS - Mass print option.
  Columns 21 - 25: KBAL - Heat balance print option.
  Columns 26 - 30: KGAS - Gas release print option.
  Columns 31 - 35: KCAV - Cavity shape print option.
  Columns 36 - 40: KDIAG - Diagnostic print option.

  If any of the quantities is greater than zero, the corresponding print option will be exercized. A zero value bypasses this print option.

* Card 6: Format(7i5) - Plot options.

  Columns 1 - 5: JTEM - Temperature plot file option.
  Columns 6 - 10: JPROP - Properties plot file option.
  Columns 11 - 15: JINT - Interface plot file option.
  Columns 16 - 20: JMAS - Mass plot file option.
  Columns 21 - 25: JBAL - Heat balance plot file option.
  Columns 26 - 30: JGAS - Gas release plot file option.
  Columns 31 - 35: JCAV - Cavity shape plot file option.

  If any of the quantities is greater than zero, the corresponding plot file will be written. A zero value bypasses the corresponding plot option.

  Card 7: Format(2e10.3)

  Columns 1 - 10: TPL - First time to write plot files, s.
  Columns 11 - 20: DPL - Time interval for writing plot files, s.

3.4 Print Output Description

The initial data will be printed out. In addition, a regular print out for each print interval DPR(I) beginning at TPR(I). For each print interval, the following data are always given: time, maximum depth, maximum radius, and next time step. Additional data output depends on the contents of card 29 (READIN) respectively card 5 (REREAD).

KTEM>0:

(a) Pool (bulk) and surface temperatures,
(b) Temperatures at the surface of the oxide and at the metal/oxide interface.
(c) Temperature of the gases leaving the melt.
(d) Temperatures at the interface of the metallic pool with the gas film. and at the interface of the oxidic pool with the gas film,
(e) Liquidus and solidus temperatures of metal and oxide layers.

KPROP>0:

Bulk properties: density, thermal conductivity, specific heat, surface tension, and viscosity of metal and oxide.

KMAS>0:

(a) Mass, volume (including voids), volume of liquid fraction, void fraction, and depth of each layer.
(b) Weight fractions of each constituents in each layer.
(c) If crust formation at the boundaries of the melt layers occurs, the crust thicknesses (in cm) are printed out.

KBAL>0:

(a) Internal energy source, entering and leaving enthalpy fluxes, heats of chemical reactions, heat delivered to concrete, heat interchanged between the phases, heat radiated from surface, and net heat gain or loss (labeled 'sensible heat').
(b) An energy balance integrated from t = 0; the initial enthalpy, internal energy, entering and leaving enthalpy fluxes, reaction energy ,energy to concrete, energy radiated from the top of the melt, totals of positive and negative energy, and the energy error.

KINT>0:

For the pool/concrete interface the erosion velocities and effective heat transfer coefficients at the pool bottom and side walls.

KGAS>0:

Mass and molar rates, weight and mole fractions of the gases currently beeing released, plus total weights and mols delivered since t = 0.

KCAV>0:

Cavity coordinates (in cm), number of cavity points.

KDIAG>0:

Diagnostics indicating numerical problems:
'RUNGE-KUTTA STEP HALVING CURTAILED'
'ITERATION FOR TK CURTAILED'
'ITERATION FOR TSUR CURTAILED'
'ITERATION FOR VOID CURTAILED'
The occasional appearance of these diagnostics does not necessarily indicate a severe problem.

3.5 Plot Output Description

If the sum (JTEM+JPROP+JINT+JMAS+JBAL+JGAS+JCAV) is not equal to zero, a plot file must be allocated. Then, plot data is written on this file in aequidistant time intervals DPL beginning with the first plot time TPL. The amount of plot data is user controlled and depends on the content of card 30 (READIN) respectively of card 6 (REREAD):

JTEM>0:

Bulk temperatures of the metal and the oxide layers, surface temperature at the top of the melt, interface temperature between the molten layers, boundary layer temperatures of the metal and the oxide melt facing the gas film.

JPROP>0:

Densities of the metal and the oxide layers

JINT>0:

Heat transfer coefficients for the bottom and sidewall heat transfer of the metal and oxide layers to the concrete.

JMAS>0:

Masses, volumes, void fractions, and heights of each layer.

JBAL>0:

Heat fluxes transferred from the melt to the concrete, and into the containment by radiation and by enthalpy transport of the gases leaving the melt.

JGAS>0:

Mass fluxes of the gas components CO_2, CO, H_2O, H_2.

JCAV>0:

(a) number of cavity points.

(b) r,z - coordinates of the cavity

3.6 Test Sample

In accordance with the German Risk Study /2/, core melt down of a German Standard PWR with a thermal power of Q_0 = 3731 MW is postulated. In the most pessimistic case, melt through of the reactor pressure vessel would occur 1 h 50 min after the initiation of the accident sequence. At that time, about 60 % of the Zirconium would be oxidized.

The core melt will slump onto the concrete basement with a temperature of about t = 2400 ^{o}C. The initial mass at the beginning of the melt/concrete interaction phase (4th phase) are given in Table 3 for the metallic and the oxidic constituents of the molten core.

The distribution of the decay heat sources in the metal and the oxide layers have been

oxide layer	UO_2	103 000 kg
	ZrO_2	24 730 kg
metal layer	Zr	12 000 kg
	Cr	11 000 kg
	Fe	53 000 kg
	Ni	6 400 kg

Table 3: Initial constituents and masses of the molten core at the beginning of the 4th phase

evaluated from ORIGEN computations /37/ carried out at GRS Köln for a German Standard PWR /38/ by taking into account fission product release into the containment on the base of /39/ and the oxidation behavior of the fission products in the molten pool. The result of this investigation is compiled in Table 4. (τ= 0: beginning of the core/concrete interaction).

τ	Q_{oxide}	Q_{metal}
s	MW	MW
0	17.78	6.57
500	18.49	5.24
1 000	19.99	3.33
2 000	19.55	3.12
3 000	19.17	2.97
5 000	18.64	2.68
10 000	17.29	2.47
25 000	14.84	2.13
65 400	12.01	1.71
353 400	8.42	1.14

Table 4: Decay heat source distribution

The idealized composition of an averaged german reactor concrete is given in Table 5. For this siliceous concrete, the density is

$$\rho_c = 2200 \text{ kg/m}^3$$

and the decomposition enthalpy is

$$\Delta H_c = 2.075 \cdot 10^6 \text{ J/kg}.$$

constituent	$CaCO_3$	$Ca(OH)_2$	SiO_2	H_2O
weight fraction	0.08	0.17	0.71	0.04

Table 5: Idealized concrete composition

Furthermore, this concrete is assumed to contain 0.1 kg iron from the concrete reinforcement per kg concrete.

The complete WECHSL input for this test sample is given in Appendix A, whereas the WECHSL print output between 0 and 10 000 s is compiled in Appendix B. In Figure 20, the surface temperature at the top of the melt, and the metal and the oxide bulk temperatures are plotted vs. time. Figure 21 gives on the same time scale a plot of the molar gas release rates for the constituents CO_2, CO, H_2O, H_2. Finally, the cavity formation resulting from the penetration of the core melt into the reactor basement is shown in Figure 22 in time steps of 1000 s.

After about 9000 s of interaction, the metal bulk temperature has dropped to a value close to the freezing temperature and a massive metal crust is being formed which reduces the heat transfer from the metal layer to the concrete considerably. As a further consequence, the gas percolation through the melt is stopped so that the strong stirring effects in the bulk are brought to an end. This reduces the heat transfer from the oxide bulk to the surface so that a strong crust is also formed at the top of the oxide melt. This behavior is indicated by the strong decrease of the surface temperature in Figure 20 and by the reduction of the gas blowing rates in Figure 21.

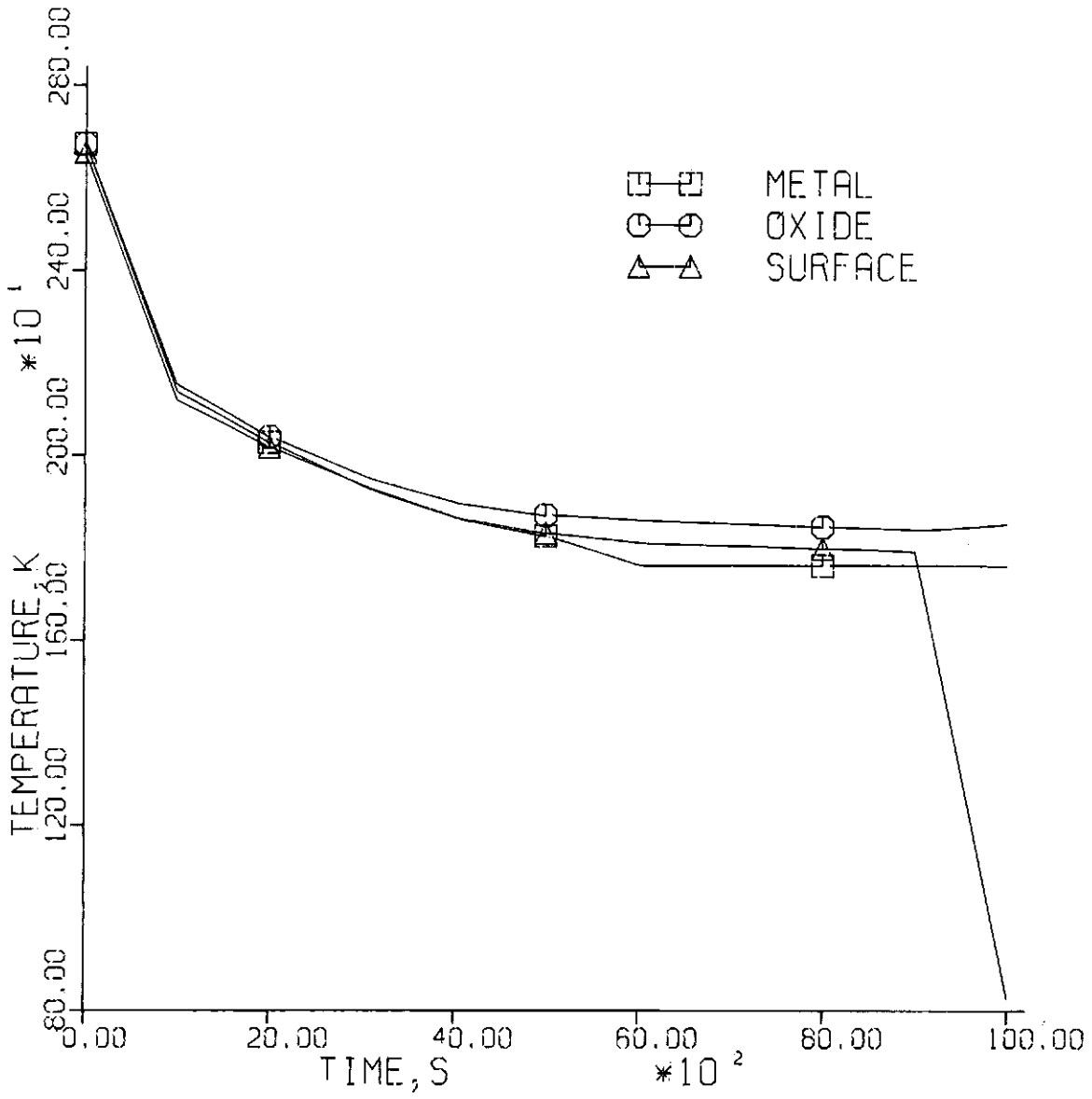

Figure 20: Sample plot of the metal, the oxide, and the surface temperatures

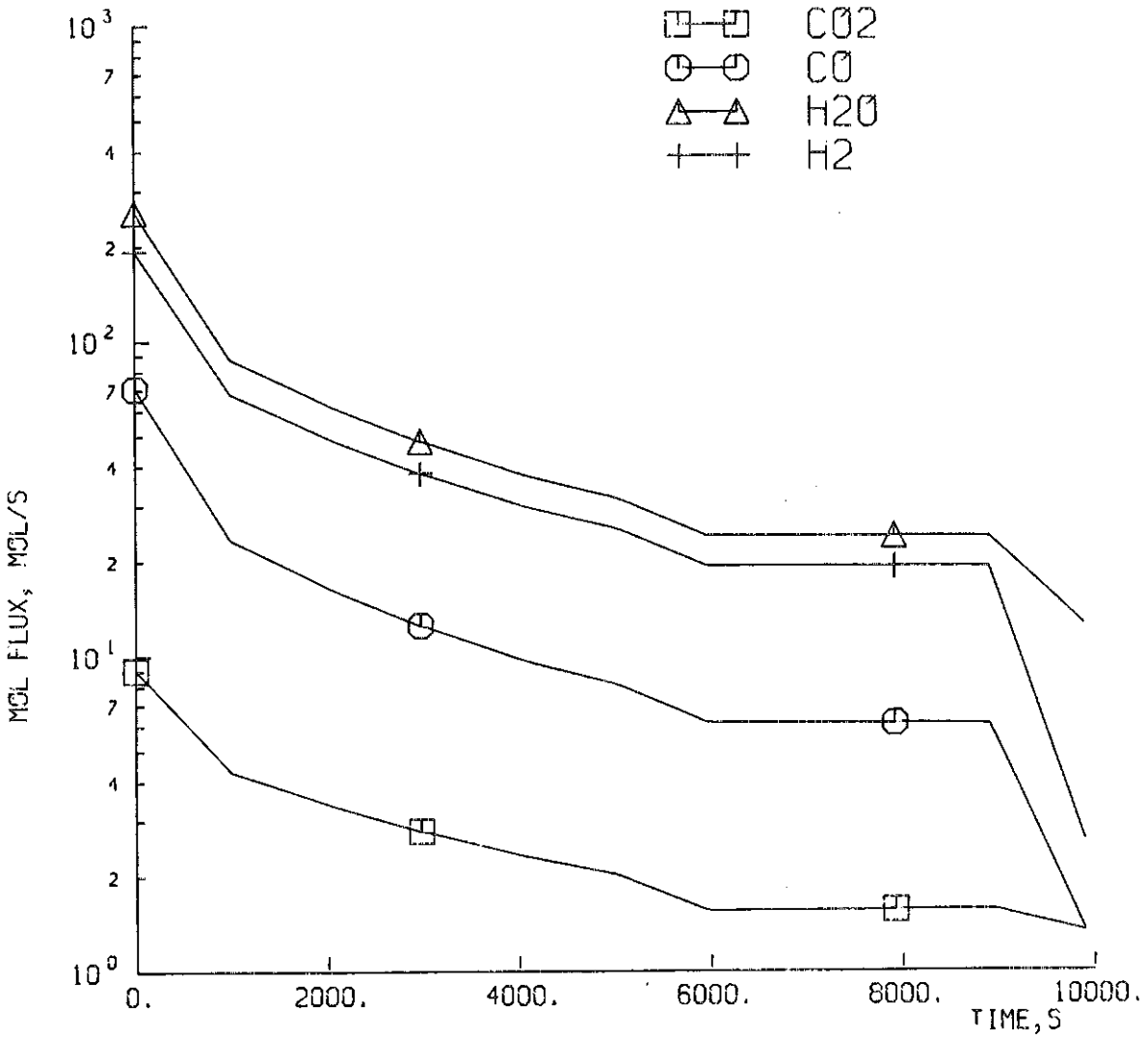

Figure 21: Sample plot of the molar gas release rates

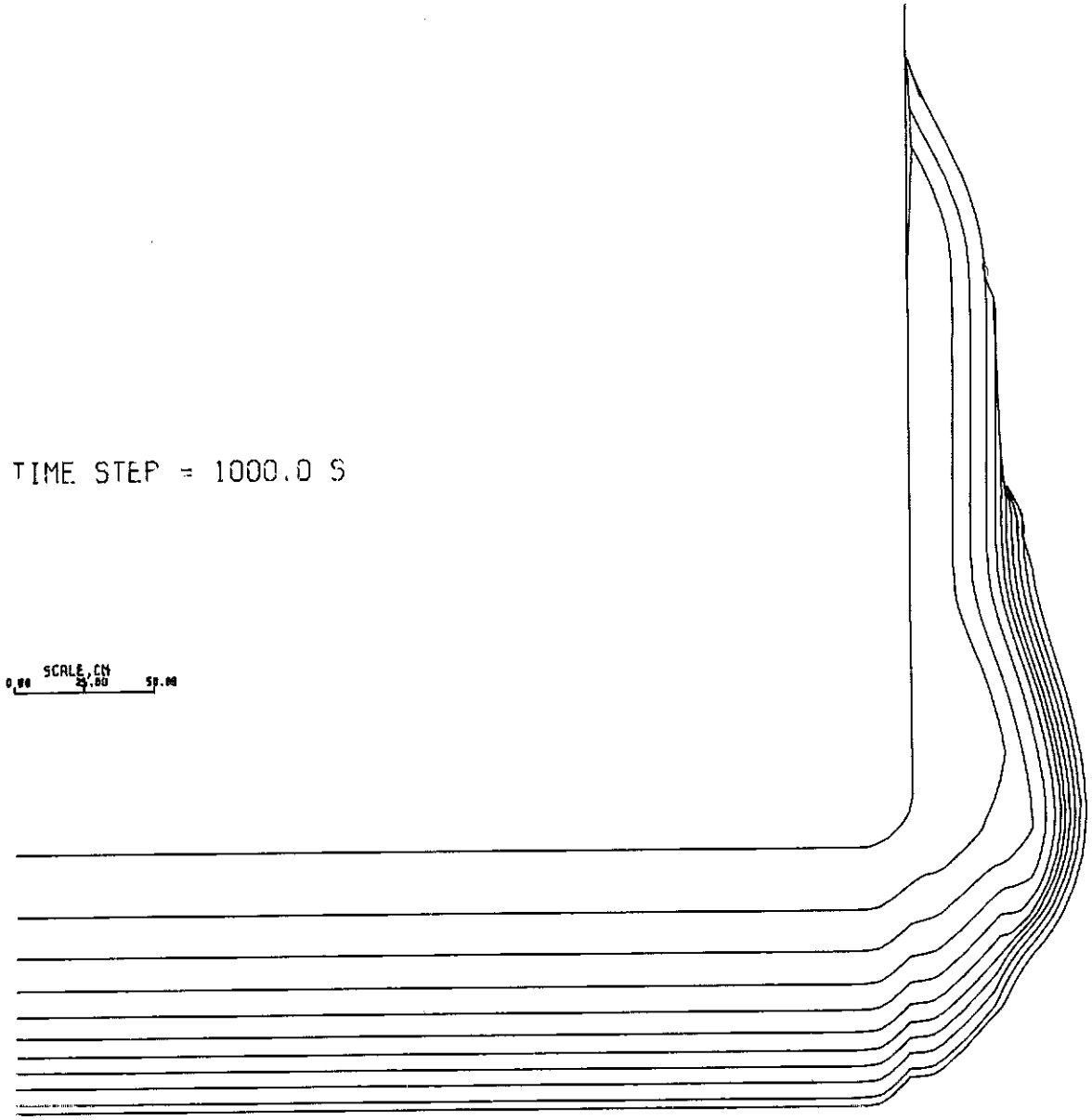

Figure 22: Sample plot of the cavity formation

4. Conclusions

The present state of modelling of the WECHSL code is due to experimental evidence restricted on phase segregation (metal layer under oxide) and includes the following separate effects:

- quasi stationary concrete decomposition;
- heat transfer from the melt to the concrete by
  - gas film model with adjacent pool boundary layer,
  - discrete bubble model;
- gas bubble rise and void fraction;
- gas driven heat transfer between the molten layers;
- gas driven heat transfer from the pool to the surface and radiation from the top of the melt;
- oxidation of the metal pool,
- temperature and composition dependent properties
- initial phase of crust formation.

The WECHSL code appears from its present state of modelling to be useable for calculating the penetration of concrete and the release of gases at least during the important initial period of a core/concrete interaction. However, a more definitive statement on the adequacy of the code must await the results of the forthcoming sustained temperature experiments in the BETA test facility.

As can be seen from the results of the test sample, massive crust formation brings the period of strong concrete erosion to an end after about 2 1/2 hours of interaction. This behavior is dependent on the type of concrete used for the construction of the reactor basement. The test sample computation has been carried out with a siliceous type of concrete as it is typical for german reactor power plants. By using a more refractive concrete with a higher decomposition enthalpy and a higher surface melting temperature, the temperature of the molten pool would be stabilized at a higher level and the pool would remain liquid for a much longer period of time.

Nevertheless, the penetration of semi-solid bodies into concrete structures is an important phenomenon for the long-time behavior

of the interaction. Model experiments and theoretical efforts are planned and finally, this phase should also be investigated in the BETA test facility.

It should be kept in mind that the dominant question for the consequences of a core melt accident of a German Standard PWR is the overpressurization of the containment by the gas release from the concrete and by sump water evaporation. On the base of WECHSL calculations under the assumption that freezing of the metal pool is supressed, the containment burst is predicted to happen 4 1/2 days after the initiation of the accident, long before reactor basement melt through could occur. Proper modelling of the freezing phenomena will however reduce the gas release rates, and the sump water evaporation, and therefore probably cause a further delay on containment failure. Moreover, the freezing behavior also reduces the penetration rate of the core into the basement structure, so that it might be doubtful whether basement melt through occurs.

Given the low entrance probability of a core melt down, the uncertainty in knowledge about the initial conditions of such an accident sequence, and the natural scattering of the results of integral experiments with hot melts in concrete crucibles, it is useful and necessary to restrict the code development to the most important physical and chemical effects. Intensive research on second order effects is not worth an extensive effort.

Literature

/1/ Rasmussen, N.C.:
"Reactor Safety Study - An Assessment of Accident Risks in US Commercial Nuclear Power Plants", USNRC, WASH 1400 (NUREG-75/014), Oct. 1975

/2/ Der Bundesminister für Forschung und Technologie (editor):
"Deutsche Risikostudie Kernkraftwerke", Verlag TÜV Rheinland, Köln 1979

/3/ Murfin, W.B.:
"A Preliminary Model for Core/Concrete Interactions", SAND77-0370, Sandia Laboratories, Albuquerque N.M., Aug. 1977

/4/ Powers, D.A.,Dahlgren, D.A., Muir, J.F., and Murfin, W.B.:
"Exploratory Study of Molten Core Material/Concrete Interactions", SAND77-2042, Sandia Laboratories, Albuquerque N.M., Feb. 1978

/5/ Perinic, D., Kammerer, B., Knauß, H., Mack, A., and Stuka, B.:
"Betontiegelversuche mit Thermitschmelzen", KfK 2572, Kernforschungszentrum Karlsruhe, Juli 1979

/6/ Peehs, M., Skokan, A., and Reimann, M.:
"The Behavior of Concrete in Contact with Molten Corium in the Case of a Hypothetical Core Melt Accident",
Nucl.Techn. 46(1979)2, p.192-198

/7/ Powers, D.A.:
"Kinetics and Stochiometry of the Thermal Decomposition of Concrete", LWR Safety Program, Quaterly Report Jan.-March 1976, SAND76-9369, Sandia Laboratories, Albuquerque N.M., Sept. 1976

/8/ Alsmeyer, H., Reimann, M.:
"On the Heat and Mass Transport Processes of a Horizontal Melting or Decomposing Layer under a Molten Pool",
Nucl.React.Safety Heat Transf., Winter Annual Meeting ASME, Atlanta Ga., Nov.1977, p.47-53

/9/ Landau, H.G.:
"Heat Conduction in a Melting Solid", Quat.Appl.Math. 8(1951), p.81-94

/10/ Berenson, P.J.:
"Film Boiling Heat Transfer from a Horizontal Surface",
Journ.Heat Transf., 38C(1961), p.351-358

/11/ Bromley, L.A.:
"Heat Transfer in Stable Film Boiling", Chem.Engng.Progr. 46 (1950)5, p.221-227

/12/ Hsu, Y.Y., Westwater, J.W.:
"Approximate Theory for Filmboiling on Vertical Surfaces",
Chem.Engng.Progr.Symp.Ser. 56(1960)30, p.15-24

/13/ Dhir, V.K., Castle, J.N., and Catton, I.:
"Role of Taylor Instability on Sublimation of a Horizontal Slab of Dry Ice", Journ.Heat Transf 99(1977)3, p.411-418

/14/ Reimann, M., Murfin, W.B., and Alsmeyer, H.:
"On the Penetration of Hot Melts into Concrete Structures", The European Nuclear Conference, Trans.ANS 31(1979), p.371-373

/15/ Reimann, M., Murfin, W.B.:
"Calculations for the Decomposition of Concrete Structures by a Molten Pool", Europ.Appl.Res.Rept. 1(1979)6, p.1554-1566

/16/ Schlichting, H.:
"Grenzschichttheorie", Karlsruhe 1975, p.556f.

/17/ Reimann, M., Alsmeyer, H.:
"Hydrodynamische und thermische Modelle zur Wechselwirkung einer Kernschmelze mit Beton" in: PNS-Halbjahresbericht 1978/2, KfK 2750, Kernforschungszentrum Karlsruhe, Oct. 1979

/18/ Lock, R.C.:
"The Velocity Distribution in the Laminar Boundary Layer Between Parallel Streams", Quart.Journ.Mech.Appl.Math. 4(1951)1, p.42-63

/19/ Reineke, H.H., Rinkleff, L., and Schramm, R.:
"Heat Transfer Between Molten Core Material and Concrete", Proc. 3rd Post Accident Heat Removal Int. Exch., ANL-78-10, Argonne Ill., Nov.2-4, 1977

/20/ Schrammm, R.:
"Untersuchungen zur Wechselwirkung von Kernschmelzen und Beton", BMFT-FB(RS166-79-05) Abschlußbericht Band Ib, TU Hannover, Sept. 1980

/21/ Levich, V.G.:
"Physicochemical Hydrodynamics", New York 1962

/22/ Mendelson, H.D.:
A.I.Ch.E.J. 13(1967), p.250

/23/ Haberman, W.F., Morton, R.K.:
"An Experimental Investigation of the Drag and Shape of Air Bubbles Rising in Various Liquids", Rept.802, David W. Taylor Basin, Sept. 1953

/24/ Le Clair, B.P., Hamielec, A.E.:
"Strömung durch Teilchenansammlungen" in "Kinetik metallurgischer Vorgänge bei der Stahlherstellung", Verlag Stahleisen, Düsseldorf 1972

/25/ Nicklin, D.J.:
Chem.Engng.Sci. 17(1962), p.693

/26/ Nikolopoulos, P., Ondracek, G.:
unpublished report of the Kernforschungszentrum Karlsruhe, 1979

/27/ Werle, H.:
"Einfluß eines Gasstroms auf den Wärmeübergang zwischen zwei Flüssigkeitsschichten" in: PNS-Halbjahresbericht 1978/2, KfK 2750, Kernforschungszentrum Karlsruhe, Okt. 1979

/28/ Haberstroh, R.D., Reinders, R.D.:
"Conduction Sheet Model for Natural Convection through a Density Stratified Interface", Int.J.Heat Mass Transf. 17(1974), p.307

/29/ Powers, D.A., Frazier, A.W.:
"VISRHO - A Computer Subroutine for Estimating the Viscosity and Density of Complex Silicate Melts", SAND76-0649, Sandia Laboratories, Albuquerque N.M., June 1977

/30/ Skoutajan, P., Baukal, W., König, R., Wagner, W., and Walter, G.:
"Durchführung von Viskositätsmessungen an oxidischen Corium - Beton - Schmelzen", BMFT-RS214A, Battelle-Institut Frankfurt/Main, Mai 1979

/31/ Kunitz, W.:
Journ.General Physiology 9(1926), p.715

/32/ Gmelin-Durrer:
"Metallurgie des Eisens" Vol.5, Berlin-Heidelberg-New York 1978, p.23a ff.

/33/ Misaelidis, P., Ondracek, G.:
unpublished report of the Kernforschungszentrum Karlsruhe, 1978

/34/ Prigogine, J., Defay, R.:
"Chemische Thermodynamik", VEB Verlag für Grundstoffindustrie, Leipzig 1962, p.378ff

/35/ Skokan, A., Hollek, H., and Peehs, M.:
"Chemical Reactions Between Light Water Reactor Core Melt and Concrete", Nucl.Techn. 46(1979)2, p.255

/36/ Muir, J.F.:
Sandia Laboratories, Albuquerque N.M., (private communication)

/37/ Bell, M.J.:
"ORIGEN, the ORNL Isotope Generation and Depletion Code", ORNL 4628, Oak Ridge, Tenn. 1973

/38/ Friederichs, H.G.:
Gesellschaft für Reaktorsicherheit, Köln, (private communication)

/39/ Albrecht, H., Wild, H.:
"Investigation of Fission Product Release by Annealing and Melting of LWR Fuel Pins in Air and Steam", ANS/ENS Topical Meeting on Reactor Safety, Aspects of Fuel Behavior, Sun Valley, Idaho, Aug. 2 - 6, 1981

/40/ Alsmeyer, H., Barleon, L., Koster, J., Michael, I., Müller, U., and Reimann, M.:
"Ein Modell zur Beschreibung der Wechselwirkung einer Kernschmelze mit Beton", KfK 2395, Kernforschungszentrum Karlsruhe, Okt. 1977

Acknowledgement

The development of the WECHSL code has required the effort of many people. The authors wish to express their gratitude to Messrs. H. Alsmeyer, D. Perinic, and H. Werle for their careful and thorough experimental work; to Messrs. L. Barleon, D.A. Dahlgren, V.K. Dhir, W. Hame, K. Hassmann, J.P. Hosemann, J.F. Muir, U. Müller, D.A. Powers, and A. Skokan for many helpful discussions and constructive suggestions; and to Projekt Nukleare Sicherheit and U.S. Nuclear Regulatory Commission for their support.

The programming assistance of Mrs. S. Stiefel is gratefully acknowledged. Thanks are also due to Mrs. U. Holzwarth for drawing the illustrations, and to Mrs. I.G. Rößler for typing of the manuscript.

APPENDIX A: WECHSL Input for Test Sample

```
0
 CORE MELT DOWN ACCIDENT (SILICEOUS CONCRETE (TYPE 1))
0
     0.        0.
     0.        0.        0.
     0.        0.        0.
     0.        0.        0.
    .08       .17       .71       .04        .1     1573.   2.075E6     2.2E3
2    3    5
24840.     1423.     1473.
3    1    2    4
80000.     2323.     2373.
1.0300E5  2.473E4       0.        0.        0.        0.        0.     2673.
10
     0.   1.778E7      5.E2   1.849E7      1.E3   1.999E7      2.E3   1.955E7
   3.E3   1.917E7      5.E3   1.864E7      1.E4   1.729E7     2.5E4   1.484E7
 6.54E4   1.201E7  3.534E5   0.842E7
5.300E4   1.200E4   1.10E4    6.40E3     2673.
10
     0.   6.57E6      5.E2   5.24E6       1.E3   3.33E6      2.E3   3.12E6
   3.E3   2.97E6      5.E3   2.68E6       1.E4   2.47E6     2.5E4   2.13E6
 6.54E4   1.71E6   3.534E5   1.14E6
    1.5   10000.
3
     0.      5.E2      2.E3      1.E3      5.E4      5.E3
2
     0.        1.      1.E7        1.
2
     0.      773.      1.E7      773.
1032
 40   10       3.2        .2       .075       4.
  .0375
 1    1    1    1    1    1    1    1
 0    0    0    0    0    0    0
     0.     1000.
```

APPENDIX B: WECHSL Output for Test Sample

```
        CORE MELT DOWN ACCIDENT (SILICEOUS CONCRETE (TYPE 1))
    GAS FILM HEAT TRANSFER MODEL

      0.0         KG/S THERMITE ADDED FOR  0.0         SEC.
 CONCRETE COMPOSITION
 CACO3     CA(OH)2   SIO2      H2O       AL2O3
0.080      0.170     0.710     0.040     0.000
 TSB=1573. K  HB=0.208E+07 J/KG  RHO=2200. KG/M3
     0.100  KG FE PER KG CONCRETE
    HB FOR CONC.+FE=  0.2200E+07 J/KG
 INITIAL MASS OF OXIDES, KG
 UO2          ZRO2         FEO          CAO          SIO2         AL2O3        CR2O3
0.1030E+06 0.2473E+05 0.0          0.0          0.0          0.0          0.0
 T=2673. K
 INTERNAL HEAT GENERATION IN OXIDES (W)
    T            Q
 0.0          0.1778E+08
 0.5000E+03   0.1849E+08
 0.1000E+04   0.1999E+08
 0.2000E+04   0.1955E+08
 0.3000E+04   0.1917E+08
 0.5000E+04   0.1864E+08
 0.1000E+05   0.1729E+08
 0.2500E+05   0.1484E+08
 0.6540E+05   0.1201E+08
 0.3534E+06   0.8420E+07
 INITIAL MASS OF METAL, KG
 FE           ZR           CR           NI
0.5300E+05 0.1200E+05 0.1100E+05 0.6400E+04
 T=2673. K
 INTERNAL HEAT GENERATION IN METALS (W)
    T            Q
 0.0          0.6570E+07
 0.5000E+03   0.5240E+07
 0.1000E+04   0.3330E+07
 0.2000E+04   0.3120E+07
 0.3000E+04   0.2970E+07
 0.5000E+04   0.2680E+07
 0.1000E+05   0.2470E+07
 0.2500E+05   0.2130E+07
 0.6540E+05   0.1710E+07
 0.3534E+06   0.1140E+07

 COMPUTATIONS MADE EVERY  1.50 SECONDS UNTIL  10000.0 SEC.
  PRINTOUT EVERY  500.SEC., BEGINNING AT    0. SEC.
  PRINTOUT EVERY 1000.SEC., BEGINNING AT 2000. SEC.
  PRINTOUT EVERY 5000.SEC., BEGINNING AT50000. SEC.

 FEO   SIO2

 UO2   ZRO2  CAO
    LIQUIDUS
     C            T
 0.0          0.1473E+04
 0.1513E-01   0.1563E+04
 0.3927E-01   0.1653E+04
 0.7490E-01   0.1743E+04
 0.1249E+00   0.1833E+04
 0.1927E+00   0.1923E+04
 0.2826E+00   0.2013E+04
 0.4000E+00   0.2103E+04
 0.5518E+00   0.2193E+04
 0.7475E+00   0.2283E+04
 0.1000E+01   0.2373E+04
    SOLIDUS
```

```
    C            T
 0.0          0.1423E+04
 0.1299E+00   0.1513E+04
 0.2395E+00   0.1603E+04
 0.3360E+00   0.1693E+04
 0.4248E+00   0.1783E+04
 0.5100E+00   0.1873E+04
 0.5950E+00   0.1963E+04
 0.6829E+00   0.2053E+04
 0.7771E+00   0.2143E+04
 0.8813E+00   0.2233E+04
 0.1000E+01   0.2323E+04

 PRESSURE HISTORY, BAR
    T            P
 0.0          0.1000E+01
 0.1000E+08   0.1000E+01

 AMBIENT TEMPERATURE HISTORY, K
    T          TAMB
 0.0          0.7730E+03
 0.1000E+08   0.7730E+03


 T=      2. SEC      Z= -0.0006 M    R= 3.2012 M
    NEXT TIME STEP= 1.2120 SEC


 TEMPERATURES, K:
 POOL - TM=2673.   TO=2673.   TSUR=2655.   TI2=2673.
 GAS  - TG=2633.
 TQMW=2614.   TQOW=2438.
 LIQ./SOL. TLM=1755.   TMM=1744.     TLO=2373.   TMO=2323.


 PROPERTIES
                                    METAL           OXIDE
         DENS.,KG/M3                6669.           6629.
         COND.,W/(M*K)             56.215           3.000
         C.P.,J/(KG*K)               690.            520.
         SIGMA,KG/S2                1.536           0.445
         VISC.,KG/(S*M)       0.1979E-02      0.5716E-02


 POOL-CONCRETE INTERFACE
                        BOTTOM     MET. WALL     OX. WALL
    VELOC.,M/S       0.4039E-01   0.8113E-01   0.6917E-01
    H,W/(M2*K)       0.1877E+04   0.3772E+04   0.3872E+04


 MASSES AND VOLUMES
                       METAL         OXIDE
 MASS,KG          0.8239E+05   0.1279E+06
 VOL.,M3          0.2745E+02   0.4294E+02
 VO,M3            0.1235E+02   0.1932E+02
 VF               0.5500E+00   0.5500E+00
 DEPTH,M          0.7800E+00   0.1208E+01
 WT. FRACTIONS
 UO2   ZRO2    FEO    CAO   SIO2   AL2O3  CR2O3
0.81   0.19   0.0    0.00   0.00   0.00   0.00
 FE     ZR     CR     NI
0.64   0.15   0.13   0.08

      HEAT FLUX BALANCE,W:
                                    METAL           OXIDE
          INTERNAL             0.6566E+07      0.1778E+08
```

ENTERING	0.1388E+09	0.3194E+09
LEAVING	-0.2218E+09	-0.6058E+08
REACTIONS	0.9527E+08	0.0
CONCRETE	-0.1099E+09	-0.7751E+08
INTERCHANGE	0.0	0.0
RADIATED	0.0	-0.4952E+08
SENSIBLE HT.	-0.9111E+08	0.1495E+09

INTEGRATED ENERGY BALANCE,W

ENTHO	0.3953E+12	ENTH	0.3954E+12	
INT	0.3652E+08	CONCR	0.2811E+09	
ENT	0.3544E+09	LEAVE	0.9087E+08	
REACT	0.1429E+09	RAD	0.7428E+08	
TOTALS	0.3959E+12		0.3959E+12	
ERROR	-0.1212E+08		-0.3063E-02	PER CENT

GASES ADDED TO ATMOSPHERE

	CO2	CO	H2O	H2
MASS FLUX,KG/S	0.3973E+00	0.1985E+01	0.4621E+01	0.3898E+00
MOL FLUX,MOL/S	0.9028E+01	0.7086E+02	0.2565E+03	0.1930E+03
WT. FRACT.	0.5374E-01	0.2685E+00	0.6251E+00	0.5272E-01
MOL FRACT.	0.1706E-01	0.1339E+00	0.4845E+00	0.3645E+00
TOT.MASS,KG	0.5960E+00	0.2977E+01	0.6932E+01	0.5847E+00
TOT.MOLS,MOL	0.1354E+02	0.1063E+03	0.3847E+03	0.2894E+03

CAVITY DIMENSIONS,CM

R	Z	R	Z	R	Z	R	Z
0.0	-0.1	7.5	-0.1	11.2	-0.1	15.0	-0.1
18.7	-0.1	22.5	-0.1	26.2	-0.1	30.0	-0.1
33.7	-0.1	37.5	-0.1	41.2	-0.1	45.0	-0.1
48.7	-0.1	52.5	-0.1	56.2	-0.1	60.0	-0.1
63.7	-0.1	67.5	-0.1	71.2	-0.1	75.0	-0.1
78.7	-0.1	82.5	-0.1	86.2	-0.1	90.0	-0.1
93.7	-0.1	97.5	-0.1	101.2	-0.1	105.0	-0.1
108.7	-0.1	112.5	-0.1	116.2	-0.1	120.0	-0.1
123.7	-0.1	127.5	-0.1	131.2	-0.1	135.0	-0.1
138.7	-0.1	142.5	-0.1	146.2	-0.1	150.0	-0.1
153.7	-0.1	157.5	-0.1	161.2	-0.1	165.0	-0.1
168.7	-0.1	172.5	-0.1	176.2	-0.1	180.0	-0.1
183.7	-0.1	187.5	-0.1	191.2	-0.1	195.0	-0.1
198.7	-0.1	202.5	-0.1	206.2	-0.1	210.0	-0.1
213.7	-0.1	217.5	-0.1	221.2	-0.1	225.0	-0.1
228.7	-0.1	232.5	-0.1	236.2	-0.1	240.0	-0.1
243.7	-0.1	247.5	-0.1	251.2	-0.1	255.0	-0.1
258.7	-0.1	262.5	-0.1	266.2	-0.1	270.0	-0.1
273.7	-0.1	277.5	-0.1	281.2	-0.1	285.0	-0.1
288.7	-0.1	292.5	-0.1	296.2	-0.1	300.0	-0.1
303.7	0.3	307.3	1.4	310.7	3.1	313.7	5.4
316.2	8.1	318.1	11.4	319.4	14.9	320.0	18.6
320.1	22.4	320.1	26.1	320.1	29.9	320.1	33.6
320.1	37.4	320.1	41.1	320.1	44.9	320.1	48.6
320.1	52.4	320.1	56.1	320.1	59.9	320.1	63.6
320.1	67.4	320.1	71.1	320.1	74.9	320.1	78.0
320.1	82.4	320.1	86.1	320.1	89.9	320.1	93.6
320.1	97.4	320.1	101.1	320.1	104.9	320.1	108.6
320.1	112.4	320.1	116.1	320.1	119.9	320.1	123.6
320.1	127.4	320.1	131.1	320.1	134.9	320.1	138.6
320.1	142.4	320.1	146.1	320.1	149.9	320.1	153.6
320.1	157.4	320.1	161.1	320.1	164.9	320.1	168.6
320.1	172.4	320.1	176.1	320.1	179.9	320.1	183.6
320.1	187.4	320.1	191.1	320.1	194.9	320.1	198.8
320.0	202.4	320.0	206.1	320.0	209.9	320.0	213.6
320.0	217.4	320.0	221.1	320.0	224.9	320.0	228.6

```
  320.0     232.4      320.0     236.1      320.0     239.9      320.0     243.6
  320.0     247.4      320.0     251.1      320.0     254.9      320.0     258.6
  320.0     262.4      320.0     266.1      320.0     269.9      320.0     273.6
  320.0     277.4      320.0     281.1      320.0     284.9      320.0     288.6
  320.0     292.4      320.0     296.1      320.0     299.9      320.0     303.6
  320.0     307.4      320.0     311.1      320.0     314.9      320.0     318.6
  320.0     322.4      320.0     326.1      320.0     329.9      320.0     333.6
  320.0     337.4      320.0     341.1      320.0     344.9      320.0     348.6
  320.0     352.4      320.0     356.1      320.0     359.9      320.0     363.6
  320.0     367.4      320.0     371.1      320.0     374.9      320.0     378.6
  320.0     382.4      320.0     386.1      320.0     389.9      320.0     393.6
  320.0     397.4      320.0     401.1      320.0     406.2
191


T=   501. SEC      Z= -0.1316 M    R= 3.4258 M
   NEXT TIME STEP= 1.4366 SEC


TEMPERATURES, K:
POOL - TM=2238.   TO=2246.   TSUR=2224.   T12=2238.
GAS  - TG=2236.
TQMW=2213.   TQOW=1969.
LIQ./SOL. TLM=1757.   TMM=1746.     TLO=2264.   TMO=2076.


PROPERTIES
                              METAL          OXIDE
        DENS.,KG/M3           6814.          5524.
        COND.,W/(M*K)        54.005          3.025
        C.P.,J/(KG*K)          709.          2563.
        SIGMA,KG/S2          1.665          1.787
        VISC.,KG/(S*M)   0.2952E-02     0.2172E+01


POOL-CONCRETE INTERFACE
                     BOTTOM     MET. WALL     OX. WALL
   VELOC.,M/S     0.2023E-01   0.3300E-01   0.9753E-02
   H,W/(M2*K)     0.1531E+04   0.2501E+04   0.1198E+04


MASSES AND VOLUMES
                    METAL         OXIDE
MASS,KG         0.8093E+05   0.1547E+06
VOL.,M3         0.2639E+02   0.6227E+02
VO,M3           0.1188E+02   0.2802E+02
VF              0.5500E+00   0.5500E+00
DEPTH,M         0.7499E+00   0.1801E+01
WT. FRACTIONS
 UO2   ZRO2    FEO    CAO   SIO2   AL2O3  CR2O3
0.67   0.19   0.0    0.03   0.11   0.00   0.00
 FE     ZR     CR     NI
0.69   0.10   0.14   0.08
CRUST THICKN.,CM
INT.MET.     INT.OX.      SURFACE      WALL MET.    WALL OX.
0.0          0.0          0.0          0.0          0.4806E-01

    HEAT FLUX BALANCE,W:
                              METAL          OXIDE
        INTERNAL          0.5235E+07     0.1849E+08
        ENTERING          0.6520E+08     0.1249E+09
        LEAVING          -0.9262E+08    -0.2497E+08
        REACTIONS         0.4304E+08     0.0
        CONCRETE         -0.5248E+08    -0.2092E+08
        INTERCHANGE       0.1644E+08    -0.1644E+08
        RADIATED          0.0           -0.2441E+08
```

SENSIBLE HT.	-0.1519E+08	0.5666E+08

INTEGRATED ENERGY BALANCE,W

ENTH0	0.3953E+12	ENTH	0.4243E+12	
INT	0.1205E+11	CONCR	0.5406E+11	
ENT	0.7020E+11	LEAVE	0.1796E+11	
REACT	0.2985E+11	RAD	0.1584E+11	
TOTALS	0.5074E+12		0.5122E+12	
ERROR	-0.4775E+10		-0.9410E+00	PER CENT

GASES ADDED TO ATMOSPHERE

	CO2	CO	H2O	H2
MASS FLUX,KG/S	0.2440E+00	0.9134E+00	0.2185E+01	0.1886E+00
MOL FLUX,MOL/S	0.5545E+01	0.3261E+02	0.1212E+03	0.9337E+02
WT. FRACT.	0.6911E-01	0.2587E+00	0.6188E+00	0.5342E-01
MOL FRACT.	0.2194E-01	0.1290E+00	0.4797E+00	0.3694E+00
TOT.MASS,KG	0.1495E+03	0.6296E+03	0.1488E+04	0.1272E+03
TOT.MOLS,MOL	0.3397E+04	0.2248E+05	0.8259E+05	0.6297E+05

CAVITY DIMENSIONS,CM

R	Z	R	Z	R	Z	R	Z
0.0	-13.2	7.5	-13.2	11.2	-13.2	15.0	-13.2
18.7	-13.2	22.5	-13.2	26.2	-13.2	30.0	-13.2
33.7	-13.2	37.5	-13.2	41.2	-13.2	45.0	-13.2
48.7	-13.2	52.5	-13.2	56.2	-13.2	60.0	-13.2
63.7	-13.2	67.5	-13.2	71.2	-13.2	75.0	-13.2
78.7	-13.2	82.5	-13.2	86.2	-13.2	90.0	-13.2
93.7	-13.2	97.5	-13.2	101.2	-13.2	105.0	-13.2
108.7	-13.2	112.5	-13.2	116.2	-13.2	120.0	-13.2
123.7	-13.2	127.5	-13.2	131.2	-13.2	135.0	-13.2
138.7	-13.2	142.5	-13.2	146.2	-13.2	150.0	-13.2
153.7	-13.2	157.5	-13.2	161.2	-13.2	165.0	-13.2
168.7	-13.2	172.5	-13.2	176.2	-13.2	180.0	-13.2
183.7	-13.2	187.5	-13.2	191.2	-13.2	195.0	-13.2
198.7	-13.2	202.5	-13.2	206.2	-13.2	210.0	-13.2
213.7	-13.2	217.5	-13.2	221.2	-13.2	225.0	-13.2
228.7	-13.2	232.5	-13.2	236.2	-13.2	240.0	-13.2
243.7	-13.2	247.5	-13.2	251.2	-13.2	255.0	-13.2
258.7	-13.2	262.5	-13.2	266.2	-13.2	270.0	-13.2
273.7	-13.2	277.5	-13.2	281.2	-13.2	285.0	-13.2
288.7	-13.2	292.5	-13.2	296.2	-13.2	300.0	-13.1
303.7	-12.8	307.4	-12.0	310.8	-10.3	313.8	-8.1
316.9	-5.9	320.1	-4.0	323.5	-2.5	326.6	-0.4
329.4	2.2	331.7	5.1	333.6	8.3	335.3	11.7
336.6	15.2	337.6	18.8	338.5	22.5	339.1	26.2
339.7	29.9	340.2	33.6	340.6	37.3	341.0	41.0
341.4	44.8	341.8	48.5	342.1	52.2	342.4	56.0
342.6	59.7	341.6	61.9	339.4	66.6	337.9	70.0
336.4	73.4	335.1	76.9	334.0	80.5	333.1	84.1
332.4	87.8	332.0	91.6	331.8	95.3	331.6	99.0
331.6	102.8	331.6	106.5	331.6	110.3	331.6	114.0
331.6	117.8	331.6	121.5	331.7	125.3	331.7	129.0
331.7	132.8	331.7	136.5	331.7	140.3	331.8	144.0
331.8	147.8	331.8	151.5	331.8	155.3	331.8	159.0
331.8	162.8	331.9	166.5	331.9	170.3	331.9	174.0
331.9	177.8	331.9	181.5	331.9	185.3	331.9	189.0
331.9	192.8	331.9	196.5	331.9	200.3	331.8	204.0
331.7	207.8	331.4	211.5	330.9	215.2	330.1	218.9
329.1	222.5	327.8	226.1	326.5	229.6	325.0	233.0
323.6	236.5	322.3	240.0	321.7	241.9	320.3	247.2
320.0	202.4						

157

```
T=  1000. SEC      Z= -0.2228 M    R= 3.5309 M
   NEXT TIME STEP= 2.3667 SEC


TEMPERATURES, K:
POOL - TM=2138.  TO=2154.  TSUR=2119.  T12=2139.
GAS  - TG=2147.
TQMW=2119.  TQOW=1889.
LIQ./SOL. TLM=1758.  TMM=1747.     TLO=2228.  TMO=1997.


PROPERTIES
                                  METAL           OXIDE
        DENS.,KG/M3               6877.           5079.
        COND.,W/(M*K)            52.591           3.036
        C.P.,J/(KG*K)              721.           2271.
        SIGMA,KG/S2               1.694           2.333
        VISC.,KG/(S*M)      0.3309E-02      0.9095E+01


POOL-CONCRETE INTERFACE
                      BOTTOM     MET. WALL     OX. WALL
   VELOC.,M/S      0.1667E-01  0.2265E-01  0.6712E-02
   H,W/(M2*K)      0.1481E+04  0.2012E+04  0.1037E+04


MASSES AND VOLUMES
                    METAL         OXIDE
MASS,KG         0.7988E+05  0.1704E+06
VOL.,M3         0.2145E+02  0.7459E+02
VO,M3           0.1161E+02  0.3356E+02
VF              0.4585E+00  0.5500E+00
DEPTH,M         0.5933E+00  0.2085E+01
WT. FRACTIONS
 UO2   ZRO2    FEO    CAO   SIO2   AL2O3  CR2O3
0.60   0.20   0.0    0.04   0.16   0.00   0.00
 FE     ZR     CR     NI
0.71   0.07   0.14   0.08
CRUST THICKN.,CM
INT.MET.     INT.OX.      SURFACE      WALL MET.    WALL OX.
0.0          0.0          0.0          0.0          0.6362E-01

    HEAT FLUX BALANCE,W:
                                  METAL           OXIDE
        INTERNAL              0.3330E+07      0.1999E+08
        ENTERING              0.4739E+08      0.8879E+08
        LEAVING              -0.6557E+08     -0.1777E+08
        REACTIONS             0.3089E+08      0.0
        CONCRETE             -0.3816E+08     -0.1493E+08
        INTERCHANGE           0.1260E+08     -0.1260E+08
        RADIATED              0.0            -0.2022E+08
        SENSIBLE HT.         -0.9514E+07      0.4325E+08

    - INTEGRATED ENERGY BALANCE,W
       ENTHO      0.3953E+12      ENTH       0.4439E+12
       INT        0.2379E+11      CONCR      0.8491E+11
       ENT        0.1112E+12      LEAVE      0.2839E+11
       REACT      0.4792E+11      RAD        0.2689E+11

       TOTALS     0.5783E+12                 0.5841E+12
       ERROR     -0.5810E+10                -0.1005E+01  PER CENT


GASES ADDED TO ATMOSPHERE
                  CO2          CO           H2O          H2
```

MASS FLUX,KG/S	0.1897E+00	0.6564E+00	0.1584E+01	0.1377E+00
MOL FLUX,MOL/S	0.4309E+01	0.2344E+02	0.8789E+02	0.6817E+02
WT. FRACT.	0.7386E-01	0.2557E+00	0.6168E+00	0.5363E-01
MOL FRACT.	0.2344E-01	0.1275E+00	0.4782E+00	0.3709E+00
TOT.MASS,KG	0.2563E+03	0.1013E+04	0.2410E+04	0.2071E+03
TOT.MOLS,MOL	0.5823E+04	0.3618E+05	0.1338E+06	0.1025E+06

CAVITY DIMENSIONS,CM

R	Z	R	Z	R	Z	R	Z
0.0	-22.3	7.5	-22.3	11.3	-22.3	15.0	-22.3
18.8	-22.3	22.5	-22.3	26.3	-22.3	30.0	-22.3
33.8	-22.3	37.5	-22.3	41.3	-22.3	45.0	-22.3
48.8	-22.3	52.5	-22.3	56.3	-22.3	60.0	-22.3
63.8	-22.3	67.5	-22.3	71.3	-22.3	75.0	-22.3
78.8	-22.3	82.5	-22.3	86.3	-22.3	90.0	-22.3
93.8	-22.3	97.5	-22.3	101.3	-22.3	105.0	-22.3
108.8	-22.3	112.5	-22.3	116.3	-22.3	120.0	-22.3
123.8	-22.3	127.5	-22.3	131.3	-22.3	135.0	-22.3
138.8	-22.3	142.5	-22.3	146.3	-22.3	150.0	-22.3
153.8	-22.3	157.5	-22.3	161.3	-22.3	165.0	-22.3
168.8	-22.3	172.5	-22.3	176.3	-22.3	180.0	-22.3
183.8	-22.3	187.5	-22.3	191.3	-22.3	195.0	-22.3
198.8	-22.3	202.5	-22.3	206.3	-22.3	210.0	-22.3
213.8	-22.3	217.5	-22.3	221.3	-22.3	225.0	-22.3
228.8	-22.3	232.5	-22.3	236.3	-22.3	240.0	-22.3
243.8	-22.3	247.5	-22.3	251.3	-22.3	255.0	-22.3
258.7	-22.3	262.5	-22.3	266.2	-22.3	270.0	-22.3
273.7	-22.3	277.5	-22.3	281.2	-22.3	285.0	-22.3
288.7	-22.3	292.5	-22.3	296.2	-22.3	300.0	-22.2
303.7	-21.9	307.4	-21.2	310.8	-19.5	313.9	-17.3
316.8	-15.0	319.8	-12.8	323.1	-10.9	326.6	-9.8
330.9	-8.1	333.0	-5.9	335.8	-3.4	338.4	-0.7
341.1	1.9	343.4	4.9	345.3	8.1	346.9	11.5
348.4	15.0	349.6	18.5	350.6	22.1	351.6	25.8
352.4	29.4	353.1	33.1	352.5	37.1	351.8	40.5
350.9	44.1	350.0	47.8	349.0	51.4	347.9	55.0
346.8	58.6	345.6	62.1	344.2	65.6	342.8	69.1
341.4	72.6	340.1	76.1	338.9	79.6	338.0	83.3
337.2	86.9	336.6	90.6	336.3	94.4	336.0	98.1
335.9	101.9	335.8	105.6	335.8	109.4	335.8	113.1
335.8	116.9	335.8	120.6	335.8	124.4	335.8	128.1
335.8	131.9	335.9	135.6	335.9	139.4	335.9	143.1
335.9	146.9	335.9	150.6	336.0	154.4	336.0	158.1
336.0	161.9	336.0	165.6	336.0	169.4	336.0	173.1
336.0	176.9	336.1	180.6	336.1	184.4	336.1	188.1
336.1	191.9	336.0	195.6	336.0	199.4	335.9	203.1
335.7	206.8	335.3	210.6	334.8	214.3	334.1	218.0
333.2	221.6	332.2	225.2	331.0	228.8	329.7	232.3
328.3	235.8	326.8	239.2	325.2	242.6	323.7	245.6
321.8	249.3	320.3	247.2				

162

T= 1503. SEC Z= -0.3007 M R= 3.5897 M
NEXT TIME STEP= 3.5043 SEC

TEMPERATURES, K:
POOL - TM=2076. TO=2093. TSUR=2063. T12=2076.
GAS - TG=2088.
TOMW=2059. TOOW=1871.
LIQ./SOL, TLM=1758. TMM=1748. TLO=2208. TMO=1952.

PROPERTIES

	METAL	OXIDE
DENS.,KG/M3	6925.	4818.
COND.,W/(M*K)	51.461	3.043
C.P.,J/(KG*K)	731.	2159.
SIGMA,KG/S2	1.712	2.690
VISC.,KG/(S*M)	0.3575E-02	0.7589E+01

POOL-CONCRETE INTERFACE

	BOTTOM	MET. WALL	OX. WALL
VELOC.,M/S	0.1457E-01	0.1785E-01	0.6167E-02
H,W/(M2*K)	0.1452E+04	0.1780E+04	0.1005E+04

MASSES AND VOLUMES

	METAL	OXIDE
MASS,KG	0.7908E+05	0.1828E+06
VOL.,M3	0.1837E+02	0.8435E+02
VO,M3	0.1142E+02	0.3796E+02
VF	0.3783E+00	0.5500E+00
DEPTH,M	0.5054E+00	0.2305E+01

WT. FRACTIONS

UO2	ZRO2	FEO	CAO	SIO2	AL2O3	CR2O3
0.56	0.20	0.0	0.05	0.19	0.00	0.00

FE	ZR	CR	NI
0.73	0.05	0.14	0.08

CRUST THICKN.,CM

INT.MET.	INT.OX.	SURFACE	WALL MET.	WALL OX.
0.0	0.0	0.0	0.0	0.5107E-01

HEAT FLUX BALANCE,W:

	METAL	OXIDE
INTERNAL	0.3224E+07	0.1977E+08
ENTERING	0.3943E+08	0.7489E+08
LEAVING	-0.5315E+08	-0.1450E+08
REACTIONS	0.2536E+08	0.0
CONCRETE	-0.3159E+08	-0.1519E+08
INTERCHANGE	0.1234E+08	-0.1234E+08
RADIATED	0.0	-0.1811E+08
SENSIBLE HT.	-0.4396E+07	0.3451E+08

INTEGRATED ENERGY BALANCE,W

ENTHO	0.3953E+12	ENTH	0.4604E+12	
INT	0.3543E+11	CONCR	0.1093E+12	
ENT	0.1436E+12	LEAVE	0.3638E+11	
REACT	0.6186E+11	RAD	0.3644E+11	
TOTALS	0.6362E+12		0.6426E+12	
ERROR	-0.6358E+10		-0.9994E+00	PER CENT

GASES ADDED TO ATMOSPHERE

	CO2	CO	H2O	H2
MASS FLUX,KG/S	0.1645E+00	0.5387E+00	0.1308E+01	0.1144E+00
MOL FLUX,MOL/S	0.3739E+01	0.1923E+02	0.7260E+02	0.5661E+02
WT. FRACT.	0.7740E-01	0.2534E+00	0.6154E+00	0.5380E-01
MOL FRACT.	0.2457E-01	0.1264E+00	0.4770E+00	0.3720E+00
TOT.MASS,KG	0.3443E+03	0.1310E+04	0.3128E+04	0.2696E+03
TOT.MOLS,MOL	0.7823E+04	0.4676E+05	0.1736E+06	0.1335E+06

CAVITY DIMENSIONS,CM

R	Z	R	Z	R	Z	R	Z
0.0	-30.1	7.5	-30.1	11.3	-30.1	15.0	-30.1
18.8	-30.1	22.5	-30.1	26.3	-30.1	30.0	-30.1
33.8	-30.1	37.5	-30.1	41.3	-30.1	45.0	-30.1

48.8	-30.1	52.5	-30.1	56.3	-30.1	60.0	-30.1
63.8	-30.1	67.5	-30.1	71.3	-30.1	75.0	-30.1
78.8	-30.1	82.5	-30.1	86.3	-30.1	90.0	-30.1
93.8	-30.1	97.5	-30.1	101.3	-30.1	105.0	-30.1
108.8	-30.1	112.5	-30.1	116.3	-30.1	120.0	-30.1
123.8	-30.1	127.5	-30.1	131.3	-30.1	135.0	-30.1
138.8	-30.1	142.5	-30.1	146.3	-30.1	150.0	-30.1
153.8	-30.1	157.5	-30.1	161.3	-30.1	165.0	-30.1
168.8	-30.1	172.5	-30.1	176.3	-30.1	180.0	-30.1
183.8	-30.1	187.5	-30.1	191.3	-30.1	195.0	-30.1
198.8	-30.1	202.5	-30.1	206.3	-30.1	210.0	-30.1
213.8	-30.1	217.5	-30.1	221.3	-30.1	225.0	-30.1
228.8	-30.1	232.5	-30.1	236.3	-30.1	240.0	-30.1
243.8	-30.1	247.5	-30.1	251.3	-30.1	255.0	-30.1
258.8	-30.1	262.5	-30.1	266.3	-30.1	270.0	-30.1
273.8	-30.1	277.5	-30.1	281.3	-30.1	285.0	-30.1
288.8	-30.1	292.5	-30.1	296.3	-30.1	300.0	-30.0
303.7	-29.7	307.4	-29.0	310.8	-27.4	313.9	-25.2
316.8	-22.8	319.7	-20.4	323.2	-19.3	326.7	-18.0
330.0	-16.1	333.0	-13.9	335.8	-11.4	338.6	-8.9
341.3	-6.3	344.4	-4.2	347.5	-2.0	350.1	0.7
352.3	3.7	354.3	6.9	356.1	10.2	357.6	13.7
359.0	17.2	358.8	20.5	358.1	24.6	357.3	28.3
356.6	32.0	355.8	35.6	355.0	39.3	354.1	42.9
353.2	46.6	352.2	50.2	351.2	53.8	350.1	57.4
348.9	60.9	347.6	64.5	346.3	68.0	345.0	71.5
343.7	75.0	342.6	78.6	341.6	82.2	340.7	85.9
340.1	89.5	339.6	93.3	339.2	97.0	339.0	100.7
338.9	104.5	338.8	108.2	338.7	112.0	338.7	115.7
338.8	119.5	338.8	123.2	338.8	127.0	338.8	130.7
338.8	134.5	338.9	138.2	338.9	142.0	338.9	145.7
338.9	149.5	338.9	153.2	338.9	157.0	339.0	160.7
339.0	164.5	339.0	168.2	339.0	172.0	339.0	175.7
339.0	179.5	339.0	183.2	339.0	187.0	339.0	190.7
339.0	194.5	338.9	198.2	338.8	202.0	338.6	205.7
338.2	209.5	337.7	213.2	337.1	216.9	336.3	220.5
335.3	224.2	334.3	227.8	333.0	231.3	331.7	234.8
330.2	238.3	328.6	241.6	326.9	245.0	325.1	248.2
323.7	251.0	321.7	255.0	321.8	249.3		

167
RUNGE-KUTTA STEP HALVING CURTAILED AT T= 0.1245E+04

T= 2003. SEC Z= -0.3697 M R= 3.6274 M
NEXT TIME STEP= 3.8116 SEC

TEMPERATURES, K:
POOL - TM=2028. TO=2040. TSUR=2018. T12=2029.
GAS - TG=2037.
TOMW=2014. TOOW=1873.
LIQ./SOL. TLM=1759. TMM=1749. TLO=2193. TMO=1918.

PROPERTIES

	METAL	OXIDE
DENS.,KG/M3	6967.	4620.
COND.,W/(M*K)	50.472	3.049
C.P.,J/(KG*K)	740.	2090.
SIGMA,KG/S2	1.726	2.979
VISC.,KG/(S*M)	0.3805E-02	0.3031E+01

POOL-CONCRETE INTERFACE

	BOTTOM	MET. WALL	OX. WALL
VELOC.,M/S	0.1307E-01	0.1484E-01	0.6613E-02

H,W/(M2*K) 0.1440E+04 0.1637E+04 0.1076E+04

MASSES AND VOLUMES

	METAL	OXIDE
MASS,KG	0.7850E+05	0.1943E+06
VOL.,M3	0.1671E+02	0.9348E+02
VO,M3	0.1127E+02	0.4207E+02
VF	0.3257E+00	0.5500E+00
DEPTH,M	0.4607E+00	0.2504E+01

WT. FRACTIONS

UO2	ZRO2	FEO	CAO	SIO2	AL2O3	CR2O3
0.53	0.20	0.0	0.05	0.22	0.00	0.00

FE	ZR	CR	NI
0.75	0.03	0.14	0.08

CRUST THICKN.,CM

INT.MET.	INT.OX.	SURFACE	WALL MET.	WALL OX.
0.0	0.0	0.0	0.0	0.2833E-01

HEAT FLUX BALANCE,W:

	METAL	OXIDE
INTERNAL	0.3120E+07	0.1955E+08
ENTERING	0.3470E+08	0.6850E+08
LEAVING	-0.4559E+08	-0.1249E+08
REACTIONS	0.2199E+08	0.0
CONCRETE	-0.2757E+08	-0.1769E+08
INTERCHANGE	0.8710E+07	-0.8710E+07
RADIATED	0.0	-0.1649E+08
SENSIBLE HT.	-0.4647E+07	0.3267E+08

INTEGRATED ENERGY BALANCE,W

ENTHO	0.3953E+12	ENTH	0.4754E+12	
INT	0.4684E+11	CONCR	0.1325E+12	
ENT	0.1734E+12	LEAVE	0.4312E+11	
REACT	0.7368E+11	RAD	0.4507E+11	
TOTALS	0.6892E+12		0.6960E+12	
ERROR	-0.6789E+10		-0.9850E+00	PER CENT

GASES ADDED TO ATMOSPHERE

	CO2	CO	H2O	H2
MASS FLUX,KG/S	0.1498E+00	0.4660E+00	0.1139E+01	0.1001E+00
MOL FLUX,MOL/S	0.3405E+01	0.1664E+02	0.6320E+02	0.4954E+02
WT. FRACT.	0.8078E-01	0.2513E+00	0.6140E+00	0.5395E-01
MOL FRACT.	0.2564E-01	0.1253E+00	0.4760E+00	0.3731E+00
TOT.MASS,KG	0.4229E+03	0.1560E+04	0.3739E+04	0.3231E+03
TOT.MOLS,MOL	0.9608E+04	0.5571E+05	0.2075E+06	0.1600E+06

CAVITY DIMENSIONS,CM

R	Z	R	Z	R	Z	R	Z
0.0	-37.0	7.5	-37.0	11.3	-37.0	15.0	-37.0
18.8	-37.0	22.5	-37.0	26.3	-37.0	30.0	-37.0
33.8	-37.0	37.5	-37.0	41.3	-37.0	45.0	-37.0
48.8	-37.0	52.5	-37.0	56.3	-37.0	60.0	-37.0
63.8	-37.0	67.5	-37.0	71.3	-37.0	75.0	-37.0
78.8	-37.0	82.5	-37.0	86.3	-37.0	90.0	-37.0
93.8	-37.0	97.5	-37.0	101.3	-37.0	105.0	-37.0
108.8	-37.0	112.5	-37.0	116.3	-37.0	120.0	-37.0
123.8	-37.0	127.5	-37.0	131.3	-37.0	135.0	-37.0
138.8	-37.0	142.5	-37.0	146.3	-37.0	150.0	-37.0
153.8	-37.0	157.5	-37.0	161.3	-37.0	165.0	-37.0
168.8	-37.0	172.5	-37.0	176.3	-37.0	180.0	-37.0
183.8	-37.0	187.5	-37.0	191.3	-37.0	195.0	-37.0
198.8	-37.0	202.5	-37.0	206.3	-37.0	210.0	-37.0

```
  213.8    -37.0      217.5    -37.0      221.3    -37.0      225.0    -37.0
  228.8    -37.0      232.5    -37.0      236.3    -37.0      240.0    -37.0
  243.8    -37.0      247.5    -37.0      251.3    -37.0      255.0    -37.0
  258.8    -37.0      262.5    -37.0      266.3    -37.0      270.0    -37.0
  273.8    -37.0      277.5    -37.0      281.3    -37.0      285.0    -37.0
  288.8    -37.0      292.5    -37.0      296.3    -37.0      300.0    -36.9
  303.7    -36.6      307.4    -36.0      310.8    -34.3      313.9    -32.1
  316.8    -29.7      319.6    -27.2      323.2    -26.4      326.8    -25.2
  330.0    -23.3      333.0    -21.0      335.8    -18.6      338.6    -16.0
  341.3    -13.4      344.1    -10.9      347.1     -8.8      350.5     -7.1
  353.6     -5.0      356.3     -2.4      358.7      0.5      360.9      3.6
  362.7      6.8      362.7      9.2      362.3     14.3      361.9     18.1
  361.4     21.8      360.8     25.5      360.2     29.2      359.4     32.9
  358.6     36.5      357.8     40.2      356.9     43.8      356.0     47.5
  355.0     51.1      354.0     54.7      352.9     58.3      351.7     61.8
  350.5     65.4      349.2     68.9      348.0     72.4      346.8     76.0
  345.7     79.6      344.8     83.2      344.0     86.9      343.3     90.6
  342.8     94.3      342.5     98.0      342.2    101.8      342.1    105.5
  342.0    109.3      342.0    113.0      341.9    116.8      341.9    120.5
  342.0    124.3      342.0    128.0      342.0    131.8      342.0    135.5
  342.1    139.3      342.1    143.0      342.1    146.8      342.1    150.5
  342.2    154.3      342.2    158.0      342.2    161.8      342.2    165.5
  342.2    169.3      342.3    173.0      342.3    176.8      342.3    180.5
  342.3    184.3      342.3    188.0      342.2    191.8      342.2    195.5
  342.1    199.3      341.9    203.0      341.6    206.7      341.2    210.5
  340.7    214.2      340.0    217.9      339.2    221.5      338.2    225.2
  337.1    228.8      335.9    232.3      334.6    235.8      333.1    239.3
  331.5    242.7      329.9    246.0      328.1    249.3      326.4    252.7
  324.6    256.0      323.0    259.6      321.4    262.7      321.7    255.0
172


T=  3003. SEC      Z= -0.4871 M    R= 3.6736 M
   NEXT TIME STEP= 3.7963 SEC


TEMPERATURES, K:
POOL - TM=1934.  TO=1956.  TSUR=1936.  T12=1935.
GAS  - TG=1955.
TQMW=1923.  TQOW=1811.
LIQ./SOL. TLM=1761.  TMM=1751.     TLO=2166.  TMO=1870.


PROPERTIES
                                  METAL          OXIDE
        DENS.,KG/M3                7037.          4350.
        COND.,W/(M*K)             49.091          3.079
        C.P.,J/(KG*K)               751.          2043.
        SIGMA,KG/S2                1.753          3.404
        VISC.,KG/(S*M)       0.4340E-02     0.2450E+01


POOL-CONCRETE INTERFACE
                     BOTTOM     MET. WALL     OX. WALL
   VELOC.,M/S     0.1031E-01  0.9438E-02  0.4819E-02
   H,W/(M2*K)     0.1430E+04  0.1310E+04  0.9868E+03


MASSES AND VOLUMES
                    METAL         OXIDE
MASS,KG        0.7783E+05  0.2142E+06
VOL.,M3        0.1471E+02  0.1095E+03
VO,M3          0.1106E+02  0.4926E+02
VF             0.2480E+00  0.5500E+00
DEPTH,M        0.4114E+00  0.2847E+01
MT. FRACTIONS
```

UO2	ZRO2	FEO	CAO	SIO2	AL2O3	CR2O3
0.48	0.19	0.0	0.06	0.26	0.00	0.00

FE	ZR	CR	NI
0.78	0.0	0.14	0.08

CRUST THICKN.,CM

INT.MET.	INT.OX.	SURFACE	WALL MET.	WALL OX.
0.0	0.0	0.0	0.0	0.4791E-01

HEAT FLUX BALANCE,W:

	METAL	OXIDE
INTERNAL	0.2970E+07	0.1917E+08
ENTERING	0.2654E+08	0.5213E+08
LEAVING	-0.3407E+08	-0.9282E+07
REACTIONS	0.4690E+07	0.0
CONCRETE	-0.2105E+08	-0.1414E+08
INTERCHANGE	0.1466E+08	-0.1468E+08
RADIATED	0.0	-0.1384E+08
SENSIBLE HT.	-0.6250E+07	0.1936E+08

INTEGRATED ENERGY BALANCE,W

ENTHO	0.3953E+12	ENTH	0.4996E+12
INT	0.6925E+11	CONCR	0.1734E+12
ENT	0.2252E+12	LEAVE	0.5396E+11
REACT	0.8993E+11	RAD	0.6017E+11
TOTALS	0.7797E+12		0.7872E+12
ERROR	-0.7516E+10		-0.9640E+00 PER CENT

GASES ADDED TO ATMOSPHERE

	CO2	CO	H2O	H2
MASS FLUX,KG/S	0.1229E+00	0.3505E+00	0.8663E+00	0.7680E-01
MOL FLUX,MOL/S	0.2792E+01	0.1251E+02	0.4807E+02	0.3802E+02
WT. FRACT.	0.8674E-01	0.2475E+00	0.6116E+00	0.5422E-01
MOL FRACT.	0.2753E-01	0.1234E+00	0.4741E+00	0.3750E+00
TOT.MASS,KG	0.5594E+03	0.1967E+04	0.4738E+04	0.4114E+03
TOT.MOLS,MOL	0.1271E+05	0.7024E+05	0.2629E+06	0.2036E+06

CAVITY DIMENSIONS,CM

R	Z	R	Z	R	Z	R	Z
0.0	-48.7	7.5	-48.7	11.3	-48.7	15.0	-48.7
18.8	-48.7	22.5	-48.7	26.3	-48.7	30.0	-48.7
33.8	-48.7	37.5	-48.7	41.3	-48.7	45.0	-48.7
48.8	-48.7	52.5	-48.7	56.3	-48.7	60.0	-48.7
63.8	-48.7	67.5	-48.7	71.3	-48.7	75.0	-48.7
78.8	-48.7	82.5	-48.7	86.3	-48.7	90.0	-48.7
93.8	-48.7	97.5	-48.7	101.3	-48.7	105.0	-48.7
108.8	-48.7	112.5	-48.7	116.3	-48.7	120.0	-48.7
123.8	-48.7	127.5	-48.7	131.3	-48.7	135.0	-48.7
138.8	-48.7	142.5	-48.7	146.3	-48.7	150.0	-48.7
153.8	-48.7	157.5	-48.7	161.3	-48.7	165.0	-48.7
168.8	-48.7	172.5	-48.7	176.3	-48.7	180.0	-48.7
183.8	-48.7	187.5	-48.7	191.3	-48.7	195.0	-48.7
198.8	-48.7	202.5	-48.7	206.3	-48.7	210.0	-48.7
213.8	-48.7	217.5	-48.7	221.3	-48.7	225.0	-48.7
228.8	-48.7	232.5	-48.7	236.3	-48.7	240.0	-48.7
243.8	-48.7	247.5	-48.7	251.3	-48.7	255.0	-48.7
258.8	-48.7	262.5	-48.7	266.3	-48.7	270.0	-48.7
273.8	-48.7	277.5	-48.7	281.3	-48.7	285.0	-48.7
288.8	-48.7	292.5	-48.7	296.3	-48.7	300.0	-48.6
303.7	-48.4	307.4	-47.7	310.8	-46.1	313.8	-43.8
316.7	-41.4	319.4	-38.8	323.1	-38.3	326.8	-37.3
330.0	-35.5	333.0	-33.1	335.8	-30.6	338.5	-28.1
341.2	-25.4	343.8	-22.8	346.5	-20.2	349.4	-17.8
352.5	-15.6	356.0	-14.4	359.5	-13.0	362.6	-10.9

```
   364.2     -7.5      365.2     -3.9      366.1     -0.2      366.8      3.4
   367.2      7.2      367.4     10.9      367.2     14.7      367.0     18.4
   366.5     22.1      366.0     25.8      365.4     29.5      364.7     33.2
   363.9     36.9      363.1     40.6      362.3     44.2      361.3     47.9
   360.4     51.5      359.3     55.1      358.3     58.7      357.1     62.3
   356.0     65.8      354.8     69.4      353.7     73.0      352.5     76.5
   351.5     80.1      350.6     83.8      349.8     87.4      349.2     91.1
   348.7     94.9      348.3     98.6      348.0    102.3      347.8    106.1
   347.7    109.8      347.7    113.6      347.7    117.3      347.7    121.1
   347.7    124.8      347.7    128.6      347.7    132.3      347.8    136.1
   347.8    139.8      347.8    143.6      347.9    147.3      347.9    151.1
   347.9    154.8      348.0    158.6      348.0    162.3      348.0    166.1
   348.1    169.8      348.1    173.6      348.1    177.3      348.1    181.1
   348.1    184.8      348.1    188.6      348.0    192.3      347.9    196.1
   347.8    199.8      347.6    203.6      347.2    207.3      346.8    211.0
   346.3    214.7      345.6    218.4      344.8    222.1      343.9    225.7
   342.8    229.3      341.7    232.9      340.4    236.4      339.0    239.9
   337.5    243.3      335.9    246.7      334.2    250.1      332.5    253.4
   330.8    256.8      329.2    260.1      327.5    263.5      326.0    266.9
   324.4    270.3      323.0    273.8      321.9    277.1      320.5    280.9
   321.4    262.7
 181


 T=  4004. SEC      Z= -0.5797 M    R= 3.7048 M
    NEXT TIME STEP= 4.5217 SEC


 TEMPERATURES, K:
 POOL - TM=1867.  TO=1900.  TSUR=1871.  T12=1868.
 GAS  - TG=1894.
 TQPW=1858.  TQOW=1730.
 LIQ./SOL. TLM=1762.  TMM=1752.     TLO=2150.  TMO=1841.


 PROPERTIES
                                  METAL          OXIDE
         DENS.,KG/M3               7079.          4207.
         COND.,W/(M*K)            48.801          3.154
         C.P.,J/(KG*K)              750.          2022.
         SIGMA,KG/S2               1.769          3.642
         VISC.,KG/(S*M)       0.4808E-02     0.6907E+01


 POOL-CONCRETE INTERFACE
                      BOTTOM     MET. WALL    OX. WALL
    VELOC.,M/S     0.8413E-02  0.7315E-02  0.2547E-02
    H,W/(M2*K)     0.1430E+04  0.1245E+04  0.7915E+03


 MASSES AND VOLUMES
                     METAL         OXIDE
 MASS,KG        0.7754E+05  0.2279E+06
 VOL.,M3        0.1362E+02  0.8440E+02
 VO,M3          0.1095E+02  0.5418E+02
 VF             0.1959E+00  0.3581E+00
 DEPTH,M        0.3857E+00  0.2094E+01
 WT. FRACTIONS
 UO2   ZRO2    FEO    CAO   SIO2   AL2O3  CR2O3
0.45   0.18   0.0    0.07   0.29   0.00   0.01
 FE     ZR     CR     NI
0.80   0.0    0.12   0.08
 CRUST THICKN.,CM
 INT.MET.     INT.OX.      SURFACE      WALL MET.    WALL OX.
 0.0          0.0          0.0          0.0          0.1420E+00
```

HEAT FLUX BALANCE,W:

	METAL	OXIDE
INTERNAL	0.2824E+07	0.1890E+08
ENTERING	0.2083E+08	0.3623E+08
LEAVING	-0.2642E+08	-0.7199E+07
REACTIONS	0.3517E+07	0.0
CONCRETE	-0.1679E+08	-0.6105E+07
INTERCHANGE	0.1229E+08	-0.1229E+08
RADIATED	0.0	-0.1326E+08
SENSIBLE HT.	-0.3763E+07	0.1628E+08

INTEGRATED ENERGY BALANCE,W

ENTHO	0.3953E+12	ENTH	0.5128E+12	
INT	0.9119E+11	CONCR	0.2018E+12	
ENT	0.2620E+12	LEAVE	0.6211E+11	
REACT	0.9397E+11	RAD	0.7375E+11	
TOTALS	0.8425E+12		0.8504E+12	
ERROR	-0.7932E+10		-0.9415E+00	PER CENT

GASES ADDED TO ATMOSPHERE

	CO2	CO	H2O	H2
MASS FLUX,KG/S	0.1036E+00	0.2761E+00	0.6888E+00	0.6151E-01
MOL FLUX,MOL/S	0.2353E+01	0.9856E+01	0.3822E+02	0.3045E+02
WT. FRACT.	0.9165E-01	0.2443E+00	0.6096E+00	0.5444E-01
MOL FRACT.	0.2909E-01	0.1219E+00	0.4725E+00	0.3765E+00
TOT.MASS,KG	0.6722E+03	0.2278E+04	0.5509E+04	0.4799E+03
TOT.MOLS,MOL	0.1527E+05	0.8132E+05	0.3057E+06	0.2376E+06

CAVITY DIMENSIONS,CM

R	Z	R	Z	R	Z	R	Z
0.0	-58.0	7.5	-58.0	11.3	-58.0	15.0	-58.0
18.8	-58.0	22.5	-58.0	26.3	-58.0	30.0	-58.0
33.8	-58.0	37.5	-58.0	41.3	-58.0	45.0	-58.0
48.8	-58.0	52.5	-58.0	56.3	-58.0	60.0	-58.0
63.8	-58.0	67.5	-58.0	71.3	-58.0	75.0	-58.0
78.8	-58.0	82.5	-58.0	86.3	-58.0	90.0	-58.0
93.8	-58.0	97.5	-58.0	101.3	-58.0	105.0	-58.0
108.8	-58.0	112.5	-58.0	116.3	-58.0	120.0	-58.0
123.8	-58.0	127.5	-58.0	131.3	-58.0	135.0	-58.0
138.8	-58.0	142.5	-58.0	146.3	-58.0	150.0	-58.0
153.8	-58.0	157.5	-58.0	161.3	-58.0	165.0	-58.0
168.8	-58.0	172.5	-58.0	176.3	-58.0	180.0	-58.0
183.8	-58.0	187.5	-58.0	191.3	-58.0	195.0	-58.0
198.8	-58.0	202.5	-58.0	206.3	-58.0	210.0	-58.0
213.8	-58.0	217.5	-58.0	221.3	-58.0	225.0	-58.0
228.8	-58.0	232.5	-58.0	236.3	-58.0	240.0	-58.0
243.8	-58.0	247.5	-58.0	251.3	-58.0	255.0	-58.0
258.8	-58.0	262.5	-58.0	266.3	-58.0	270.0	-58.0
273.8	-58.0	277.5	-58.0	281.3	-58.0	285.0	-58.0
288.8	-58.0	292.5	-58.0	296.3	-58.0	300.0	-57.9
303.7	-57.6	307.5	-57.0	310.8	-55.3	313.8	-53.0
316.6	-50.6	319.3	-48.0	323.0	-47.6	326.7	-46.7
330.0	-44.9	332.9	-42.6	335.7	-40.1	338.4	-37.5
341.1	-34.8	343.7	-32.2	346.3	-29.5	348.9	-26.8
351.6	-24.2	355.3	-23.8	358.9	-22.6	361.5	-19.4
363.6	-16.7	365.3	-13.4	366.7	-9.9	367.9	-6.3
368.9	-2.7	369.6	1.0	370.2	4.7	370.4	8.4
370.5	12.2	370.3	15.9	370.0	19.6	369.6	23.4
369.0	27.1	368.4	30.8	367.7	34.5	366.9	38.1
366.1	41.8	365.2	45.4	364.3	49.1	363.3	52.7
362.3	56.3	361.2	59.9	360.0	63.4	358.9	67.0
357.7	70.6	356.6	74.2	355.6	77.8	354.6	81.4
353.8	85.0	353.0	88.7	352.4	92.4	351.9	96.1

```
  351.6     99.9      351.3    103.6      351.1    107.4      351.0    111.1
  351.0    114.9      351.0    118.6      351.0    122.4      351.0    126.1
  351.0    129.9      351.1    133.6      351.1    137.4      351.2    141.1
  351.2    144.9      351.2    148.6      351.3    152.4      351.3    156.1
  351.3    159.9      351.4    163.6      351.4    167.4      351.4    171.1
  351.4    174.9      351.5    178.6      351.5    182.4      351.5    186.1
  351.1    190.0      350.7    193.6      320.5    280.9
159
   ITERATION FOR VOID CURTAILED AT T=  0.3615E+04


T=  5003. SEC     Z= -0.6577 M    R= 3.7256 M
   NEXT TIME STEP= 4.5217 SEC


TEMPERATURES, K:
POOL - TM=1826.  TO=1871.  TSUR=1832.  T12=1828.
GAS  - TG=1860.
TOMW=1819.  TOOW=1696.
LIQ./SOL. TLM=1764.  TMM=1754.    TLO=2140.  TMO=1823.


PROPERTIES
                                 METAL          OXIDE
        DENS.,KG/M3               7111.          4117.
        COND.,W/(M*K)            48.569          3.209
        C.P.,J/(KG*K)              749.          2013.
        SIGMA,KG/S2               1.779          3.796
        VISC.,KG/(S*M)      0.5131E-02     0.1237E+02


POOL-CONCRETE INTERFACE
                        BOTTOM     MET. WALL    OX. WALL
   VELOC.,M/S      0.7309E-02  0.4741E-02  0.1856E-02
   H,W/(M2*K)      0.1435E+04  0.9318E+03  0.7361E+03


MASSES AND VOLUMES
                    METAL         OXIDE
MASS,KG        0.7716E+05  0.2379E+06
VOL.,M3        0.1302E+02  0.6946E+02
VO,M3          0.1085E+02  0.5778E+02
VF             0.1669E+00  0.1682E+00
DEPTH,M        0.3718E+00  0.1683E+01
WT. FRACTIONS
 UO2   ZRO2    FEO    CAO   SIO2   AL2O3  CR2O3
0.43   0.17   0.0    0.07   0.30   0.00   0.02
 FE     ZR     CR     NI
0.82   0.0    0.10   0.08
CRUST THICKN.,CM
INT.MET.     INT.OX.      SURFACE      WALL MET.    WALL OX.
0.0          0.0          0.0          0.0          0.2115E+00

    HEAT FLUX BALANCE,W:
                                 METAL          OXIDE
        INTERNAL              0.2680E+07     0.1864E+08
        ENTERING              0.1744E+08     0.2878E+08
        LEAVING              -0.2189E+08    -0.5976E+07
        REACTIONS             0.2849E+07     0.0
        CONCRETE             -0.1415E+08    -0.3599E+07
        INTERCHANGE           0.1046E+08    -0.1046E+08
        RADIATED              0.0           -0.1217E+08
        SENSIBLE HT.         -0.2601E+07     0.1521E+08

     INTEGRATED ENERGY BALANCE,W
       ENTHO      0.3953E+12      ENTH       0.5257E+12
```

INT	0.1127E+12	CONCR	0.2219E+12	
ENT	0.2893E+12	LEAVE	0.6867E+11	
REACT	0.9713E+11	RAD	0.8636E+11	
TOTALS	0.8944E+12		0.9026E+12	
ERROR	-0.8216E+10		-0.9186E+00	PER CENT

GASES ADDED TO ATMOSPHERE

	CO2	CO	H2O	H2
MASS FLUX,KG/S	0.9014E-01	0.2308E+00	0.5791E+00	0.5196E-01
MOL FLUX,MOL/S	0.2048E+01	0.8239E+01	0.3214E+02	0.2572E+02
WT. FRACT.	0.9469E-01	0.2424E+00	0.6083E+00	0.5458E-01
MOL FRACT.	0.3006E-01	0.1209E+00	0.4716E+00	0.3775E+00
TOT.MASS,KG	0.7689E+03	0.2530E+04	0.6140E+04	0.5365E+03
TOT.MOLS,MOL	0.1747E+05	0.9033E+05	0.3407E+06	0.2656E+06

CAVITY DIMENSIONS,CM

R	Z	R	Z	R	Z	R	Z
0.0	-65.8	7.5	-65.8	11.3	-65.8	15.0	-65.8
18.8	-65.8	22.5	-65.8	26.3	-65.8	30.0	-65.8
33.8	-65.8	37.5	-65.8	41.3	-65.8	45.0	-65.8
48.8	-65.8	52.5	-65.8	56.3	-65.8	60.0	-65.8
63.8	-65.8	67.5	-65.8	71.3	-65.8	75.0	-65.8
78.8	-65.8	82.5	-65.8	86.3	-65.8	90.0	-65.8
93.8	-65.8	97.5	-65.8	101.3	-65.8	105.0	-65.8
108.8	-65.8	112.5	-65.8	116.3	-65.8	120.0	-65.8
123.8	-65.8	127.5	-65.8	131.3	-65.8	135.0	-65.8
138.8	-65.8	142.5	-65.8	146.3	-65.8	150.0	-65.8
153.8	-65.8	157.5	-65.8	161.3	-65.8	165.0	-65.8
168.8	-65.8	172.5	-65.8	176.3	-65.8	180.0	-65.8
183.8	-65.8	187.5	-65.8	191.3	-65.8	195.0	-65.8
198.8	-65.8	202.5	-65.8	206.3	-65.8	210.0	-65.8
213.8	-65.8	217.5	-65.8	221.3	-65.8	225.0	-65.8
228.8	-65.8	232.5	-65.8	236.3	-65.8	240.0	-65.8
243.8	-65.8	247.5	-65.8	251.3	-65.8	255.0	-65.8
258.8	-65.8	262.5	-65.8	266.3	-65.8	270.0	-65.8
273.8	-65.8	277.5	-65.8	281.3	-65.8	285.0	-65.8
288.8	-65.8	292.5	-65.8	296.3	-65.8	300.0	-65.7
303.7	-65.4	307.5	-64.8	310.8	-63.1	313.8	-60.8
316.6	-58.3	319.2	-55.6	322.9	-55.3	326.6	-54.6
329.9	-52.8	332.9	-50.5	335.6	-48.0	338.3	-45.4
341.0	-42.7	343.6	-40.0	346.1	-37.3	348.7	-34.5
351.2	-31.7	354.8	-31.0	357.7	-28.6	360.3	-25.9
362.4	-22.8	364.4	-19.6	366.2	-16.3	367.8	-12.9
369.1	-9.4	370.3	-5.8	371.2	-2.2	371.8	1.5
372.3	5.2	372.5	9.0	372.6	12.7	372.4	16.5
372.1	20.2	371.7	23.9	371.1	27.6	370.5	31.3
369.8	35.0	369.0	38.7	368.2	42.3	367.3	46.0
366.4	49.6	365.4	53.2	364.3	56.8	363.2	60.4
362.0	64.0	360.8	67.5	359.7	71.1	358.6	74.7
357.6	78.3	356.7	81.9	355.8	85.6	355.1	89.3
354.5	93.0	354.0	96.7	353.7	100.4	353.4	104.2
353.2	107.9	353.1	111.7	353.1	115.4	353.0	119.2
353.1	122.9	353.1	126.7	353.1	130.4	353.1	134.2
352.8	139.8	352.7	141.6	350.7	193.6		

147

T= 6002. SEC Z= -0.7233 M R= 3.7410 M
NEXT TIME STEP= 4.5035 SEC

TEMPERATURES, K:
POOL - TM=1764. TO=1859. TSUR=1811. T12=1766.

```
GAS  - TG=1846.
TQMW=1759.   TQOW=1696.
LIQ./SOL. TLM=1765.   TMM=1755.     TLO=2133.   TMO=1810.

PROPERTIES
                                  METAL          OXIDE
        DENS.,KG/M3                7144.          4050.
        COND.,W/(M*K)             48.379          3.251
        C.P.,J/(KG*K)             29670.          2008.
        SIGMA,KG/S2                1.796          3.913
        VISC.,KG/(S*M)        0.5703E-02     0.1436E+02

POOL-CONCRETE INTERFACE
                      BOTTOM     MET. WALL     OX. WALL
   VELOC.,M/S      0.5636E-02  0.3651E-02  0.1814E-02
   H,W/(M2*K)      0.1463E+04  0.9518E+03  0.7205E+03

MASSES AND VOLUMES
                     METAL         OXIDE
MASS,KG          0.7683E+05  0.2458E+06
VOL.,M3          0.1232E+02  0.6718E+02
VO,M3            0.1076E+02  0.6070E+02
VF               0.1267E+00  0.9643E-01
DEPTH,M          0.3545E+00  0.1608E+01
WT. FRACTIONS
 UO2   ZRO2    FEO    CAO   SIO2   AL2O3  CR2O3
0.42   0.17   0.0    0.08   0.31   0.00   0.03
 FE     ZR     CR     NI
0.83   0.0    0.09   0.08
CRUST THICKN.,CM
INT.MET.     INT.OX.      SURFACE      WALL MET.    WALL OX.
0.0          0.1781E+00   0.0          0.0          0.1938E+00

     HEAT FLUX BALANCE,W:
                                  METAL          OXIDE
          INTERNAL             0.2638E+07     0.1837E+08
          ENTERING             0.1318E+08     0.2191E+08
          LEAVING             -0.1605E+08    -0.4484E+07
          REACTIONS            0.2014E+07     0.0
          CONCRETE            -0.1065E+08    -0.3464E+07
          INTERCHANGE          0.3159E+07    -0.3159E+07
          RADIATED             0.0           -0.1163E+08
          SENSIBLE HT.        -0.5710E+07     0.1754E+08

       INTEGRATED ENERGY BALANCE,W
          ENTHO      0.3953E+12      ENTH       0.5383E+12
          INT        0.1338E+12      CONCR      0.2378E+12
          ENT        0.3110E+12      LEAVE      0.7394E+11
          REACT      0.9958E+11      RAD        0.9818E+11

          TOTALS     0.9398E+12                 0.9483E+12
          ERROR     -0.8476E+10                -0.9020E+00   PER CENT

GASES ADDED TO ATMOSPHERE
                     CO2           CO            H2O           H2
MASS FLUX,KG/S    0.6883E-01  0.1731E+00  0.4357E+00  0.3917E-01
MOL FLUX,MOL/S    0.1564E+01  0.6182E+01  0.2418E+02  0.1939E+02
WT. FRACT.        0.9602E-01  0.2416E+00  0.6078E+00  0.5464E-01
MOL FRACT.        0.3048E-01  0.1205E+00  0.4712E+00  0.3779E+00
TOT.MASS,KG       0.8495E+03  0.2734E+04  0.6653E+04  0.5825E+03
TOT.MOLS,MOL      0.1930E+05  0.9762E+05  0.3692E+06  0.2884E+06
```

CAVITY DIMENSIONS,CM

R	Z	R	Z	R	Z	R	Z
0.0	-72.3	7.5	-72.3	11.3	-72.3	15.0	-72.3
18.8	-72.3	22.5	-72.3	26.3	-72.3	30.0	-72.3
33.8	-72.3	37.5	-72.3	41.3	-72.3	45.0	-72.3
48.8	-72.3	52.5	-72.3	56.3	-72.3	60.0	-72.3
63.8	-72.3	67.5	-72.3	71.3	-72.3	75.0	-72.3
78.8	-72.3	82.5	-72.3	86.3	-72.3	90.0	-72.3
93.8	-72.3	97.5	-72.3	101.3	-72.3	105.0	-72.3
108.8	-72.3	112.5	-72.3	116.3	-72.3	120.0	-72.3
123.8	-72.3	127.5	-72.3	131.3	-72.3	135.0	-72.3
138.8	-72.3	142.5	-72.3	146.3	-72.3	150.0	-72.3
153.8	-72.3	157.5	-72.3	161.3	-72.3	165.0	-72.3
168.8	-72.3	172.5	-72.3	176.3	-72.3	180.0	-72.3
183.8	-72.3	187.5	-72.3	191.3	-72.3	195.0	-72.3
198.8	-72.3	202.5	-72.3	206.3	-72.3	210.0	-72.3
213.8	-72.3	217.5	-72.3	221.3	-72.3	225.0	-72.3
228.8	-72.3	232.5	-72.3	236.3	-72.3	240.0	-72.3
243.8	-72.3	247.5	-72.3	251.3	-72.3	255.0	-72.3
258.8	-72.3	262.5	-72.3	266.3	-72.3	270.0	-72.3
273.8	-72.3	277.5	-72.3	281.3	-72.3	285.0	-72.3
288.8	-72.3	292.5	-72.3	296.3	-72.3	300.0	-72.3
303.7	-72.0	307.5	-71.4	310.8	-69.6	313.7	-67.3
316.5	-64.8	319.1	-62.1	322.8	-61.9	326.5	-61.2
329.8	-59.4	332.8	-57.1	335.5	-54.5	338.2	-51.9
340.9	-49.3	343.4	-46.5	346.0	-43.8	348.5	-41.0
352.3	-36.9	353.5	-35.5	356.1	-32.7	358.7	-30.0
361.2	-27.2	363.4	-24.2	365.4	-21.0	367.2	-17.7
368.8	-14.3	370.2	-10.8	371.4	-7.3	372.4	-3.7
373.1	0.0	373.7	3.7	374.0	7.5	374.1	11.2
374.0	15.0	373.8	18.7	373.4	22.4	373.0	26.2
372.4	29.9	371.7	33.5	371.0	37.2	370.2	40.9
369.3	44.5	368.4	48.2	367.5	51.8	366.4	55.4
365.3	59.0	364.2	62.6	363.1	66.1	361.9	69.7
360.8	73.3	359.8	76.9	358.8	80.5	357.9	84.2
357.2	87.8	356.5	91.5	356.0	95.2	355.6	99.0
355.3	102.7	355.0	106.5	354.9	110.2	354.8	114.0
354.8	117.7	354.8	121.5	354.5	123.9	353.9	128.9
352.7	141.6						

145

T= 7001. SEC Z= -0.7795 M R= 3.7576 M
NEXT TIME STEP= 4.5035 SEC

TEMPERATURES, K:
POOL - TM=1763. TO=1853. TSUR=1806. T12=1765.
GAS - TG=1841.
TQMW=1758. TQOW=1704.
LIQ./SOL. TLM=1765. TNM=1755. TLO=2127. TMO=1800.

PROPERTIES

	METAL	OXIDE
DENS.,KG/M3	7161.	3993.
COND.,W/(M*K)	48.215	3.284
C.P.,J/(KG*K)	29601.	2005.
SIGMA,KG/S2	1.795	4.015
VISC.,KG/(S*M)	0.5716E-02	0.1487E+02

POOL-CONCRETE INTERFACE

	BOTTOM	MET. WALL	OX. WALL
VELOC.,M/S	0.5611E-02	0.3646E-02	0.1953E-02

H,W/(M2*K) 0.1467E+04 0.9540E+03 0.7263E+03

MASSES AND VOLUMES

	METAL	OXIDE
MASS,KG	0.7659E+05	0.2529E+06
VOL.,M3	0.1223E+02	0.7002E+02
VD,M3	0.1070E+02	0.6333E+02
VF	0.1250E+00	0.9563E-01
DEPTH,M	0.3528E+00	0.1663E+01

WT. FRACTIONS

UO2	ZRO2	FEO	CAO	SIO2	AL2O3	CR2O3
0.41	0.16	0.0	0.08	0.32	0.00	0.03

FE	ZR	CR	NI
0.84	0.0	0.08	0.08

CRUST THICKN.,CM

INT.MET.	INT.OX.	SURFACE	WALL MET.	WALL OX.
0.0	0.1308E+00	0.0	0.0	0.1535E+00

HEAT FLUX BALANCE,W:

	METAL	OXIDE
INTERNAL	0.2596E+07	0.1810E+08
ENTERING	0.1311E+08	0.2214E+08
LEAVING	-0.1592E+08	-0.4447E+07
REACTIONS	0.1996E+07	0.0
CONCRETE	-0.1057E+08	-0.3899E+07
INTERCHANGE	0.3414E+07	-0.3414E+07
RADIATED	0.0	-0.1150E+08
SENSIBLE HT.	-0.5372E+07	0.1699E+08

INTEGRATED ENERGY BALANCE,W

ENTHO	0.3953E+12	ENTH	0.5502E+12
INT	0.1547E+12	CONCR	0.2521E+12
ENT	0.3302E+12	LEAVE	0.7840E+11
REACT	0.1016E+12	RAD	0.1097E+12
TOTALS	0.9818E+12		0.9905E+12
ERROR	-0.8666E+10		-0.8827E+00 PER CENT

GASES ADDED TO ATMOSPHERE

	CO2	CO	H2O	H2
MASS FLUX,KG/S	0.6859E-01	0.1716E+00	0.4321E+00	0.3887E-01
MOL FLUX,MOL/S	0.1558E+01	0.6126E+01	0.2398E+02	0.1924E+02
WT. FRACT.	0.9644E-01	0.2413E+00	0.6076E+00	0.5466E-01
MOL FRACT.	0.3061E-01	0.1203E+00	0.4710E+00	0.3780E+00
TOT.MASS,KG	0.9182E+03	0.2907E+04	0.7086E+04	0.6215E+03
TOT.MOLS,MOL	0.2086E+05	0.1038E+06	0.3932E+06	0.3077E+06

CAVITY DIMENSIONS,CM

R	Z	R	Z	R	Z	R	Z
0.0	-77.9	7.5	-77.9	11.3	-77.9	15.0	-77.9
18.8	-77.9	22.5	-77.9	26.3	-77.9	30.0	-77.9
33.8	-77.9	37.5	-77.9	41.3	-77.9	45.0	-77.9
48.8	-77.9	52.5	-77.9	56.3	-77.9	60.0	-77.9
63.8	-77.9	67.5	-77.9	71.3	-77.9	75.0	-77.9
78.8	-77.9	82.5	-77.9	86.3	-77.9	90.0	-77.9
93.8	-77.9	97.5	-77.9	101.3	-77.9	105.0	-77.9
108.8	-77.9	112.5	-77.9	116.3	-77.9	120.0	-77.9
123.8	-77.9	127.5	-77.9	131.3	-77.9	135.0	-77.9
138.8	-77.9	142.5	-77.9	146.3	-77.9	150.0	-77.9
153.8	-77.9	157.5	-77.9	161.3	-77.9	165.0	-77.9
168.8	-77.9	172.5	-77.9	176.3	-77.9	180.0	-77.9
183.8	-77.9	187.5	-77.9	191.3	-77.9	195.0	-77.9
198.8	-77.9	202.5	-77.9	206.3	-77.9	210.0	-77.9

```
  213.8    -77.9      217.5    -77.9      221.3    -77.9      225.0    -77.9
  228.8    -77.9      232.5    -77.9      236.3    -77.9      240.0    -77.9
  243.8    -77.9      247.5    -77.9      251.3    -77.9      255.0    -77.9
  258.8    -77.9      262.5    -77.9      266.3    -77.9      270.0    -77.9
  273.8    -77.9      277.5    -77.9      281.3    -77.9      285.0    -77.9
  288.8    -77.9      292.5    -77.9      296.3    -77.9      300.0    -77.9
  303.8    -77.6      307.5    -77.0      310.8    -75.2      313.7    -72.9
  316.5    -70.4      319.0    -67.6      322.7    -67.4      326.4    -66.8
  329.7    -65.0      332.7    -62.7      335.4    -60.2      338.1    -57.5
  340.7    -54.8      343.3    -52.1      345.8    -49.3      348.4    -46.6
  350.9    -42.7      352.5    -40.3      354.8    -37.3      357.3    -34.5
  359.8    -31.8      362.2    -28.9      364.5    -25.9      366.5    -22.8
  368.4    -19.5      369.9    -16.1      371.3    -12.6      372.6     -9.1
  373.6     -5.5      374.5     -1.8      375.1      1.9      375.5      5.6
  375.7      9.4      375.8     13.1      375.6     16.9      375.4     20.6
  374.9     24.3      374.4     28.1      373.8     31.8      373.1     35.4
  372.4     39.1      371.6     42.8      370.7     46.4      369.8     50.1
  368.8     53.7      367.7     57.3      366.6     60.9      365.5     64.4
  364.4     68.0      363.3     71.6      362.2     75.2      361.2     78.8
  360.3     82.4      359.5     86.1      358.8     89.8      358.2     93.5
  357.7     97.2      357.3    100.9      357.0    104.7      356.8    108.4
  356.7    112.2      356.7    115.9      356.3    119.6      355.3    123.7
  354.5    126.9      353.9    128.9
146
   RUNGE-KUTTA STEP HALVING CURTAILED AT T=  0.6614E+04


T=  8004. SEC      Z= -0.8358 M    R= 3.7754 M
   NEXT TIME STEP= 4.5035 SEC


TEMPERATURES, K:
POOL - TM=1762.   TO=1846.   TSUR=1799.   T12=1764.
GAS  - TG=1836.
TOMW=1758.   TQOW=1709.
LIQ./SOL.  TLM=1767.   TMM=1756.     TLO=2122.   TMO=1790.


PROPERTIES
                                 METAL          OXIDE
        DENS.,KG/M3              7178.          3940.
        COND.,W/(M*K)           48.050          3.315
        C.P.,J/(KG*K)           26767.          2002.
        SIGMA,KG/S2              1.793          4.112
        VISC.,KG/(S*M)       0.5722E-02     0.1600E+02


POOL-CONCRETE INTERFACE
                        BOTTOM      MET. WALL     OX. WALL
   VELOC.,M/S       0.5604E-02   0.3643E-02   0.2029E-02
   H,W/(M2*K)       0.1470E+04   0.9559E+03   0.7254E+03


MASSES AND VOLUMES
                      METAL         OXIDE
MASS,KG          0.7637E+05   0.2600E+06
VOL.,M3          0.1216E+02   0.7295E+02
VO,M3            0.1064E+02   0.6601E+02
VF               0.1251E+00   0.9522E-01
DEPTH,M          0.3511E+00   0.1719E+01
WT. FRACTIONS
 UO2   ZRO2    FEO    CAO   SIO2   AL2O3  CR2O3
0.40   0.16   0.0    0.08   0.33   0.00   0.03
 FE     ZR     CR     NI
0.85   0.0    0.06   0.08
 CRUST THICKN.,CM
```

INT.MET.	INT.OX.	SURFACE	WALL MET.	WALL OX.
0.0	0.9424E-01	0.0	0.0	0.1276E+00

HEAT FLUX BALANCE,W:

	METAL	OXIDE
INTERNAL	0.2554E+07	0.1783E+08
ENTERING	0.1309E+08	0.2234E+08
LEAVING	-0.1586E+08	-0.4427E+07
REACTIONS	0.1988E+07	0.0
CONCRETE	-0.1054E+08	-0.4197E+07
INTERCHANGE	0.3511E+07	-0.3511E+07
RADIATED	0.0	-0.1134E+08
SENSIBLE HT.	-0.5257E+07	0.1670E+08

INTEGRATED ENERGY BALANCE,W

ENTHO	0.3953E+12	ENTH	0.5620E+12
INT	0.1753E+12	CONCR	0.2668E+12
ENT	0.3498E+12	LEAVE	0.8285E+11
REACT	0.1036E+12	RAD	0.1212E+12
TOTALS	0.1024E+13		0.1033E+13
ERROR	-0.8861E+10		-0.8654E+00 PER CENT

GASES ADDED TO ATMOSPHERE

	CO2	CO	H2O	H2
MASS FLUX,KG/S	0.6874E-01	0.1708E+00	0.4306E+00	0.3877E-01
MOL FLUX,MOL/S	0.1562E+01	0.6099E+01	0.2390E+02	0.1919E+02
MT. FRACT.	0.9696E-01	0.2410E+00	0.6074E+00	0.5468E-01
MOL FRACT.	0.3078E-01	0.1202E+00	0.4709E+00	0.3782E+00
TOT.MASS,KG	0.9871E+03	0.3078E+04	0.7518E+04	0.6605E+03
TOT.MOLS,MOL	0.2243E+05	0.1099E+06	0.4172E+06	0.3270E+06

CAVITY DIMENSIONS,CM

R	Z	R	Z	R	Z	R	Z
0.0	-83.6	7.5	-83.6	11.3	-83.6	15.0	-83.6
18.8	-83.6	22.5	-83.6	26.3	-83.6	30.0	-83.6
33.8	-83.6	37.5	-83.6	41.3	-83.6	45.0	-83.6
48.8	-83.6	52.5	-83.6	56.3	-83.6	60.0	-83.6
63.8	-83.6	67.5	-83.6	71.3	-83.6	75.0	-83.6
78.8	-83.6	82.5	-83.6	86.3	-83.6	90.0	-83.6
93.8	-83.6	97.5	-83.6	101.3	-83.6	105.0	-83.6
108.8	-83.6	112.5	-83.6	116.3	-83.6	120.0	-83.6
123.8	-83.6	127.5	-83.6	131.3	-83.6	135.0	-83.6
138.8	-83.6	142.5	-83.6	146.3	-83.6	150.0	-83.6
153.8	-83.6	157.5	-83.6	161.3	-83.6	165.0	-83.6
168.8	-83.6	172.5	-83.6	176.3	-83.6	180.0	-83.6
183.8	-83.6	187.5	-83.6	191.3	-83.6	195.0	-83.6
198.8	-83.6	202.5	-83.6	206.3	-83.6	210.0	-83.6
213.8	-83.6	217.5	-83.6	221.3	-83.6	225.0	-83.6
228.8	-83.6	232.5	-83.6	236.3	-83.6	240.0	-83.6
243.8	-83.6	247.5	-83.6	251.3	-83.6	255.0	-83.6
258.8	-83.6	262.5	-83.6	266.3	-83.6	270.0	-83.6
273.8	-83.6	277.5	-83.6	281.3	-83.6	285.0	-83.6
288.8	-83.6	292.5	-83.6	296.3	-83.6	300.0	-83.5
303.8	-83.2	307.5	-82.6	310.8	-80.8	313.7	-78.5
316.5	-75.9	318.9	-73.1	322.7	-73.0	326.4	-72.4
329.7	-70.6	332.6	-68.3	335.4	-65.7	338.0	-63.1
340.7	-60.4	343.2	-57.7	345.7	-54.9	348.2	-52.1
350.3	-48.4	351.9	-45.6	353.9	-42.4	356.2	-39.4
358.6	-36.5	361.0	-33.7	363.4	-30.8	365.6	-27.8
367.7	-24.6	369.5	-21.3	371.0	-17.9	372.5	-14.5
373.8	-11.0	374.9	-7.4	375.8	-3.7	376.6	-0.1
377.1	3.7	377.4	7.4	377.5	11.1	377.5	14.9
377.3	18.6	377.0	22.4	376.6	26.1	376.0	29.8

```
  375.4     33.5     374.7     37.2     373.9     40.9     373.1     44.5
  372.2     48.2     371.3     51.8     370.3     55.4     369.2     59.0
  368.1     62.6     367.0     66.2     365.9     69.8     364.8     73.4
  363.8     77.0     362.8     80.6     362.0     84.2     361.2     87.9
  360.5     91.6     360.0     95.3     359.5     99.0     359.2    102.8
  359.0    106.5     358.8    110.2     358.6    114.0     358.1    117.7
  357.0    121.3     356.2    123.4     354.6    128.4     354.5    126.9
148

T=  9003. SEC      Z= -0.8917 M    R= 3.7938 M
   NEXT TIME STEP= 4.5035 SEC


TEMPERATURES, K:
POOL - TM=1762.  TO=1839.  TSUR=1792.  T12=1764.
GAS  - TG=1830.
TQMW=1757.  TQOW=1711.
LIQ./SOL. TLM=1770.  TMM=1757.     TLO=2117.  TMO=1781.


PROPERTIES
                                 METAL          OXIDE
        DENS.,KG/M3               7195.          3890.
        COND.,W/(M*K)            47.885          3.344
        C.P.,J/(KG*K)            23331.          2001.
        SIGMA,KG/S2               1.791          4.204
        VISC.,KG/(S*M)       0.5731E-02     0.1753E+02


POOL-CONCRETE INTERFACE
                        BOTTOM     MET. WALL    OX. WALL
   VELOC.,M/S       0.5591E-02  0.3628E-02  0.2050E-02
   H,W/(M2*K)       0.1473E+04  0.9575E+03  0.7232E+03


MASSES AND VOLUMES
                    METAL          OXIDE
MASS,KG         0.7616E+05  0.2673E+06
VOL.,M3         0.1208E+02  0.7589E+02
VO,M3           0.1058E+02  0.6871E+02
VF              0.1241E+00  0.9464E-01
DEPTH,M         0.3494E+00  0.1774E+01
WT. FRACTIONS
 UO2   ZRO2    FEO    CAO   SIO2   AL2O3  CR2O3
0.39   0.15   0.0    0.08   0.34   0.00   0.04
 FE     ZR     CR     NI
0.86   0.0    0.05   0.08
CRUST THICKN.,CM
 INT.MET.     INT.OX.      SURFACE      WALL MET.    WALL OX.
 0.0          0.6466E-01   0.0          0.0          0.1095E+00

     HEAT FLUX BALANCE,W:
                                 METAL          OXIDE
          INTERNAL           0.2512E+07     0.1756E+08
          ENTERING           0.1306E+08     0.2246E+08
          LEAVING           -0.1580E+08    -0.4402E+07
          REACTIONS          0.1979E+07     0.0
          CONCRETE          -0.1050E+08    -0.4419E+07
          INTERCHANGE        0.3502E+07    -0.3502E+07
          RADIATED           0.0           -0.1118E+08
          SENSIBLE HT.      -0.5246E+07     0.1652E+08

       INTEGRATED ENERGY BALANCE,W
         ENTHO      0.3953E+12      ENTH      0.5735E+12
         INT.       0.1955E+12      CONCR     0.2816E+12
```

ENT	0.3694E+12	LEAVE	0.8725E+11	
REACT	0.1055E+12	RAD	0.1324E+12	
TOTALS	0.1066E+13		0.1075E+13	
ERROR	-0.9060E+10		-0.8501E+00	PER CENT

GASES ADDED TO ATMOSPHERE

	CO2	CO	H2O	H2
MASS FLUX,KG/S	0.6889E-01	0.1699E+00	0.4288E+00	0.3864E-01
MOL FLUX,MOL/S	0.1565E+01	0.6067E+01	0.2380E+02	0.1913E+02
WT. FRACT.	0.9753E-01	0.2406E+00	0.6072E+00	0.5471E-01
MOL FRACT.	0.3096E-01	0.1200E+00	0.4707E+00	0.3784E+00
TOT.MASS,KG	0.1056E+04	0.3249E+04	0.7948E+04	0.6991E+03
TOT.MOLS,MOL	0.2399E+05	0.1160E+06	0.4410E+06	0.3461E+06

CAVITY DIMENSIONS,CM

R	Z	R	Z	R	Z	R	Z
0.0	-89.2	7.5	-89.2	11.3	-89.2	15.0	-89.2
18.8	-89.2	22.5	-89.2	26.3	-89.2	30.0	-89.2
33.8	-89.2	37.5	-89.2	41.3	-89.2	45.0	-89.2
48.8	-89.2	52.5	-89.2	56.3	-89.2	60.0	-89.2
63.8	-89.2	67.5	-89.2	71.3	-89.2	75.0	-89.2
78.8	-89.2	82.5	-89.2	86.3	-89.2	90.0	-89.2
93.8	-89.2	97.5	-89.2	101.3	-89.2	105.0	-89.2
108.8	-89.2	112.5	-89.2	116.3	-89.2	120.0	-89.2
123.8	-89.2	127.5	-89.2	131.3	-89.2	135.0	-89.2
138.8	-89.2	142.5	-89.2	146.3	-89.2	150.0	-89.2
153.8	-89.2	157.5	-89.2	161.3	-89.2	165.0	-89.2
168.8	-89.2	172.5	-89.2	176.3	-89.2	180.0	-89.2
183.8	-89.2	187.5	-89.2	191.3	-89.2	195.0	-89.2
198.8	-89.2	202.5	-89.2	206.3	-89.2	210.0	-89.2
213.8	-89.2	217.5	-89.2	221.3	-89.2	225.0	-89.2
228.8	-89.2	232.5	-89.2	236.3	-89.2	240.0	-89.2
243.8	-89.2	247.5	-89.2	251.3	-89.2	255.0	-89.2
258.8	-89.2	262.5	-89.2	266.3	-89.2	270.0	-89.2
273.8	-89.2	277.5	-89.2	281.3	-89.2	285.0	-89.2
288.8	-89.2	292.5	-89.2	296.3	-89.2	300.0	-89.1
303.8	-88.8	307.5	-88.2	310.8	-86.4	313.7	-84.1
316.4	-81.5	318.9	-78.7	322.6	-78.6	326.3	-77.9
329.6	-76.2	332.6	-73.8	335.3	-71.3	338.0	-68.7
340.6	-66.0	343.1	-63.2	345.6	-60.4	348.1	-57.6
350.0	-54.2	351.6	-51.0	353.4	-47.7	355.4	-44.5
357.6	-41.4	359.9	-38.5	362.3	-35.6	364.6	-32.7
366.8	-29.7	368.9	-26.5	370.6	-23.2	372.2	-19.8
373.7	-16.4	375.1	-12.8	376.2	-9.3	377.2	-5.7
378.0	-2.0	378.6	1.7	379.1	5.4	379.3	9.2
379.4	12.9	379.3	16.7	379.1	20.4	378.7	24.1
378.2	27.9	377.7	31.6	377.0	35.3	376.3	38.9
375.5	42.6	374.7	46.3	373.7	49.9	372.8	53.5
371.7	57.1	370.7	60.7	369.6	64.3	368.5	67.9
367.4	71.5	366.4	75.1	365.4	78.7	364.5	82.4
363.7	86.0	363.0	89.7	362.4	93.4	361.9	97.1
361.4	100.8	361.1	104.6	360.9	108.3	360.6	112.1
360.1	115.8	359.1	119.4	357.4	123.1	355.9	126.1
354.6	128.4						

149

T= 10002. SEC Z= -0.9216 M R= 3.8149 M
NEXT TIME STEP= 4.5035 SEC

TEMPERATURES, K:
POOL - TM=1761. TO=1851. TSUR= 827. T12=1764.

GAS - TG=1838.
TQMW=1594. TQOW=1751.
LIQ./SOL. TLM=1771. TMM=1758. TLO=2113. TMO=1776.

PROPERTIES

	METAL	OXIDE
DENS.,KG/M3	7205.	3851.
COND.,W/(M*K)	47.793	3.358
C.P.,J/(KG*K)	21922.	2000.
SIGMA,KG/S2	1.790	4.277
VISC.,KG/(S*M)	0.5736E-02	0.1288E+02

POOL-CONCRETE INTERFACE

	BOTTOM	MET. WALL	OX. WALL
VELOC.,M/S	0.9011E-03	0.5122E-03	0.2802E-02
H,W/(M2*K)	0.2061E+04	0.1202E+04	0.7615E+03

MASSES AND VOLUMES

	METAL	OXIDE
MASS,KG	0.7616E+05	0.2721E+06
VOL.,M3	0.1057E+02	0.7065E+02
VO,M3	0.1057E+02	0.7065E+02
VF	0.0	0.0
DEPTH,M	0.3100E+00	0.1627E+01

WT. FRACTIONS

UO2	ZRO2	FEO	CAO	SIO2	AL2O3	CR2O3
0.38	0.15	0.0	0.08	0.35	0.00	0.04

FE	ZR	CR	NI
0.87	0.0	0.05	0.08

CRUST THICKN.,CM

INT.MET.	INT.OX.	SURFACE	WALL MET.	WALL OX.
0.0	0.1170E+00	0.1909E+01	0.4915E+01	0.2917E-01

HEAT FLUX BALANCE,W:

	METAL	OXIDE
INTERNAL	0.2470E+07	0.1729E+08
ENTERING	0.2380E+07	0.9081E+07
LEAVING	-0.2461E+07	-0.1821E+07
REACTIONS	0.3092E+06	0.0
CONCRETE	-0.1641E+07	-0.5761E+07
INTERCHANGE	0.1314E+06	-0.1314E+06
RADIATED	0.0	-0.1388E+06
SENSIBLE HT.	0.1189E+07	0.1852E+08

INTEGRATED ENERGY BALANCE,W

ENTHO	0.3953E+12	ENTH	0.5917E+12	
INT	0.2154E+12	CONCR	0.2919E+12	
ENT	0.3823E+12	LEAVE	0.8973E+11	
REACT	0.1066E+12	RAD	0.1355E+12	
TOTALS	0.1100E+13		0.1109E+13	
ERROR	-0.9195E+10		-0.8362E+00	PER CENT

GASES ADDED TO ATMOSPHERE

	CO2	CO	H2O	H2
MASS FLUX,KG/S	0.5905E-01	0.3779E-01	0.2267E+00	0.5239E-02
MOL FLUX,MOL/S	0.1342E+01	0.1349E+01	0.1258E+02	0.2594E+01
WT. FRACT.	0.1796E+00	0.1150E+00	0.6895E+00	0.1594E-01
MOL FRACT.	0.7511E-01	0.7553E-01	0.7042E+00	0.1452E+00
TOT.MASS,KG	0.1104E+04	0.3338E+04	0.8200E+04	0.7196E+03
TOT.MOLS,MOL	0.2509E+05	0.1192E+06	0.4550E+06	0.3562E+06

CAVITY DIMENSIONS,CM

R	Z	R	Z	R	Z	R	Z
0.0	-92.2	7.5	-92.2	11.3	-92.2	15.0	-92.2
18.8	-92.2	22.5	-92.2	26.3	-92.2	30.0	-92.2
33.8	-92.2	37.5	-92.2	41.3	-92.2	45.0	-92.2
48.8	-92.2	52.5	-92.2	56.3	-92.2	60.0	-92.2
63.8	-92.2	67.5	-92.2	71.3	-92.2	75.0	-92.2
78.8	-92.2	82.5	-92.2	86.3	-92.2	90.0	-92.2
93.8	-92.2	97.5	-92.2	101.3	-92.2	105.0	-92.2
108.8	-92.2	112.5	-92.2	116.3	-92.2	120.0	-92.2
123.8	-92.2	127.5	-92.2	131.3	-92.2	135.0	-92.2
138.8	-92.2	142.5	-92.2	146.3	-92.2	150.0	-92.2
153.8	-92.2	157.5	-92.2	161.3	-92.2	165.0	-92.2
168.8	-92.2	172.5	-92.2	176.3	-92.2	180.0	-92.2
183.8	-92.2	187.5	-92.2	191.3	-92.2	195.0	-92.2
198.8	-92.2	202.5	-92.2	206.3	-92.2	210.0	-92.2
213.8	-92.2	217.5	-92.2	221.3	-92.2	225.0	-92.2
228.8	-92.2	232.5	-92.2	236.3	-92.2	240.0	-92.2
243.8	-92.2	247.5	-92.2	251.3	-92.2	255.0	-92.2
258.8	-92.2	262.5	-92.2	266.3	-92.2	270.0	-92.2
273.8	-92.2	277.5	-92.2	281.3	-92.2	285.0	-92.2
288.8	-92.2	292.5	-92.2	296.3	-92.2	300.0	-92.1
303.8	-91.8	307.4	-91.2	310.8	-89.4	313.6	-87.0
316.4	-84.5	318.8	-81.6	322.6	-81.5	326.3	-80.9
329.6	-79.2	332.5	-76.8	335.3	-74.3	337.9	-71.6
340.5	-68.9	343.0	-66.1	345.5	-63.3	347.8	-61.2
350.9	-58.1	352.8	-54.8	354.5	-51.5	356.3	-48.2
358.3	-45.1	360.5	-42.0	362.8	-39.1	365.2	-36.1
367.4	-33.2	369.6	-30.1	371.4	-26.8	373.1	-23.5
374.7	-20.1	376.1	-16.6	377.4	-13.1	378.5	-9.5
379.5	-5.9	380.2	-2.2	380.8	1.5	381.2	5.2
381.4	9.0	381.5	12.7	381.4	16.5	381.2	20.2
380.9	24.0	380.4	27.7	379.9	31.4	379.2	35.1
378.5	38.8	377.8	42.4	376.9	46.1	376.0	49.7
375.1	53.4	374.1	57.0	373.0	60.6	372.0	64.2
370.9	67.8	369.8	71.4	368.8	75.0	367.8	78.6
366.9	82.2	366.1	85.9	365.3	89.6	364.7	93.3
364.2	97.0	362.8	101.5	362.0	104.2	355.9	126.1

144

CAVITY DIMENSIONS,CM

R	Z	R	Z	R	Z	R	Z
0.0	-92.2	7.5	-92.2	11.3	-92.2	15.0	-92.2
18.8	-92.2	22.5	-92.2	26.3	-92.2	30.0	-92.2
33.8	-92.2	37.5	-92.2	41.3	-92.2	45.0	-92.2
48.8	-92.2	52.5	-92.2	56.3	-92.2	60.0	-92.2
63.8	-92.2	67.5	-92.2	71.3	-92.2	75.0	-92.2
78.8	-92.2	82.5	-92.2	86.3	-92.2	90.0	-92.2
93.8	-92.2	97.5	-92.2	101.3	-92.2	105.0	-92.2
108.8	-92.2	112.5	-92.2	116.3	-92.2	120.0	-92.2
123.8	-92.2	127.5	-92.2	131.3	-92.2	135.0	-92.2
138.8	-92.2	142.5	-92.2	146.3	-92.2	150.0	-92.2
153.8	-92.2	157.5	-92.2	161.3	-92.2	165.0	-92.2
168.8	-92.2	172.5	-92.2	176.3	-92.2	180.0	-92.2
183.8	-92.2	187.5	-92.2	191.3	-92.2	195.0	-92.2
198.8	-92.2	202.5	-92.2	206.3	-92.2	210.0	-92.2
213.8	-92.2	217.5	-92.2	221.3	-92.2	225.0	-92.2
228.8	-92.2	232.5	-92.2	236.3	-92.2	240.0	-92.2
243.8	-92.2	247.5	-92.2	251.3	-92.2	255.0	-92.2
258.8	-92.2	262.5	-92.2	266.3	-92.2	270.0	-92.2
273.8	-92.2	277.5	-92.2	281.3	-92.2	285.0	-92.2
288.8	-92.2	292.5	-92.2	296.3	-92.2	300.0	-92.1
303.8	-91.8	307.4	-91.2	310.8	-89.4	313.6	-87.0
316.4	-84.5	318.8	-81.6	322.6	-81.5	326.3	-80.9

329.6	-79.2	332.5	-76.8	335.3	-74.3	337.9	-71.6
340.5	-68.9	343.0	-66.1	345.5	-63.3	347.8	-61.2
350.9	-58.1	352.8	-54.8	354.5	-51.5	356.3	-48.2
358.3	-45.1	360.5	-42.0	362.8	-39.1	365.2	-36.1
367.4	-33.2	369.6	-30.1	371.4	-26.8	373.1	-23.5
374.7	-20.1	376.1	-16.6	377.4	-13.1	378.5	-9.5
379.5	-5.9	380.2	-2.2	380.8	1.5	381.2	5.2
381.4	9.0	381.5	12.7	381.4	16.5	381.2	20.2
380.9	24.0	380.4	27.7	379.9	31.4	379.2	35.1
378.5	38.8	377.8	42.4	376.9	46.1	376.0	49.7
375.1	53.4	374.1	57.0	373.0	60.6	372.0	64.2
370.9	67.8	369.8	71.4	368.8	75.0	367.8	78.6
366.9	82.2	366.1	85.9	365.3	89.6	364.7	93.3
364.2	97.0	362.8	101.5	362.0	104.2	361.5	107.9
361.1	111.6	360.3	115.3	358.3	121.4	356.6	124.7
355.2	128.2	354.3	131.8	353.6	135.7	352.8	143.4
352.4	151.1	352.4	155.2	352.5	161.2	352.5	167.0
352.5	170.8	352.2	174.5	351.8	178.2	351.6	182.0
351.4	185.7	351.1	189.4	350.3	197.2	350.0	201.0
349.7	204.7	349.1	209.9	348.7	213.7	347.8	219.1
347.0	222.7	346.0	226.4	345.0	230.0	343.4	233.4
341.8	236.7	340.2	240.2	338.7	243.6	337.2	247.0
334.1	253.4	332.4	256.8	330.7	260.2	329.0	263.6
327.5	267.0	326.0	270.4	324.5	273.9	323.1	277.3
321.9	280.9	320.7	284.4	320.2	288.1	320.0	291.9
320.0	295.6	320.0	303.6	320.0	307.4	320.0	311.1
320.0	314.9	320.0	318.6	320.0	322.4	320.0	326.1
320.0	329.9	320.0	333.6	320.0	337.4	320.0	341.1
320.0	344.9	320.0	348.6	320.0	352.4	320.0	356.1
320.0	359.9	320.0	363.6	320.0	367.4	320.0	371.1
320.0	374.9	320.0	378.6	320.0	382.4	320.0	386.1
320.0	389.9	320.0	393.6	320.0	397.4	320.0	401.1
320.0	406.2						